Copyright Warning & Restrictions

The copyright law of the United States (Title 17, United States Code) governs the making of photocopies or other reproductions of copyrighted material.

Under certain conditions specified in the law, libraries and archives are authorized to furnish a photocopy or other reproduction. One of these specified conditions is that the photocopy or reproduction is not to be "used for any purpose other than private study, scholarship, or research." If a, user makes a request for, or later uses, a photocopy or reproduction for purposes in excess of "fair use" that user may be liable for copyright infringement,

This institution reserves the right to refuse to accept a copying order if, in its judgment, fulfillment of the order would involve violation of copyright law.

Please Note: The author retains the copyright while the New Jersey Institute of Technology reserves the right to distribute this thesis or dissertation

Printing note: If you do not wish to print this page, then select "Pages from: first page # to: last page #" on the print dialog screen

NJIT New Jersey's Science & Technology University

The Van Houten library has removed some of the personal information and all signatures from the approval page and biographical sketches of theses and dissertations in order to protect the identity of NJIT graduates and faculty.

ABSTRACT

NUMERICAL SIMULATION OF MECHANOFUSION SYSTEM FOR DRY PARTICLE COATING PROCESS

by
Wenliang Chen

A numerical simulation of the Mechanofusion device for dry particle coating is carried out using Discrete Element Method (DEM) technique. In dry particle coating, tiny sub-micron guest particles are coated onto larger micron sized host particles by using mechanical forces, which the Mechanofusion device provides. It consists of a rotating cylindrical chamber that contains the powder mixture, a stationary inner piece (which has a cylindrical surface at the end), and a fixed scraper blade, which prevents powder from caking against the chamber wall. The simulation studies are performed on two scales: system scale to investigate the particle-particle and particle-system interactions, and micro scale to study the degradation of agglomerates prior to the dry particle coating process.

The system-scale simulation is based on a mono-dispersed system where only host particles are taken into consideration. The particles are assumed to be frictional, elastic-plastic spheres. A widely used, non-adhesion Walton-Braun contact model has been applied in two-dimensional configuration. Two simplified geometric models of the Mechanofusion chamber with and without the scraper have been studied. The visualization of the particulate patterns inside the system and the diagnostic analysis derived from the numerical simulations clearly demonstrate the effect of scraper on the system. The forces acting on the inner piece are calculated and compared with the experimental results available from the literature. Average forces on particles due to interactions with other particles and vessel parts are also calculated and categorized into four regions. The effect of particle properties on coating level is examined through a simple deformation analysis. In addition, minimum coating

time is estimated. Furthermore, the important parameters that affect the system performance are studied.

Another important contribution of the dissertation lies in the dimensional analysis of the Mechanofusion system carried out on the basis of kinetic theory under the assumption of collisional flow, verified qualitatively by simulations. An equation for average force on particles inside the system is derived to establish the correlation between a simulated system and a real system. Major kinetic theory modeling based similarity results, verified by simulations and in part from available experimental data, include: (1) Inter-particle (host-host) forces vary linearly with the rotation speed; (2) Force exerted on the particles within the inner-piece zone is inversely proportional to the gap-size; and (3) Force on the inner-piece varies linearly with the square of the rotation speed.

Based on the results from system simulation, the fracture/fragmentation of an agglomerate during normal interactions with host particle and with system wall is examined in detail by the micro-scale simulation. The numerical study is implemented using a DEM code (developed by Prof. Thornton's group at Aston University) in two-dimensional mode, which enables the simulation of auto-adhesive particles. The study shows that single agglomerate may fracture or even shatter inside the system as a result of interactions with the host particles and system boundaries. The fracture pattern of the agglomerate is in agreement with reported three-dimensional simulation results. Results show that higher impact velocities lead to higher local damage and debris formation. However, impact velocities as low as 0.1 m/s lead to fracture in some case. In most cases, impacts at velocities of 1 m/s and higher lead to shattering of the agglomerate.

In summary, the work presented in this dissertation, which is one of the first reported work on DEM simulation of dry particle coating system, shows that DEM technique can be used to model important aspects of the Mechanofusion system,

such as the salient pattern of particles inside the system and the overall system performance as well as the agglomerate fragmentation prior to the dry particle coating process.

NUMERICAL SIMULATION OF MECHANOFUSION SYSTEM FOR DRY PARTICLE COATING PROCESS

by
Wenliang Chen

A Dissertation
Submitted to the Faculty of
New Jersey Institute of Technology
in Partial Fulfillment of the Requirements for the Degree of
Doctor of Philosophy Mechanical in Engineering

Department of Mechanical Engineering

January 2002

APPROVAL PAGE

NUMERICAL SIMULATION OF MECHANOFUSION SYSTEM FOR DRY PARTICLE COATING PROCESS

Wenliang Chen

Dr. Rajesh N. Dave, Dissertation Advisor — Date
Professor of Mechanical Engineering, NJIT

Dr. Robert Pfeffer, Dissertation Co-Advisor — Date
Distinguished Professor of Chemical Engineering, NJIT

Dr. Boris Khusid, Committee Member — Date
Associate Professor of Mechanical Engineering, NJIT

Dr. Chao Zhu, Committee Member — Date
Assistant Professor of Mechanical Engineering, NJIT

Dr. I. Joga Rao, Committee Member — Date
Assistant Professor of Mechanical Engineering, NJIT

Copyright © 2002 by Wenliang Chen
ALL RIGHTS RESERVED

BIOGRAPHICAL SKETCH

Author: Wenliang Chen

Degree: Doctor of Philosophy

Date: January 2002

Undergraduate and Graduate Education:

- Doctor of Philosophy in Mechanical Engineering,
  New Jersey Institute of Technology, Newark, NJ, 2002

- Master of Science in Mechanical Engineering,
  East China University of Science and Technology, Shanghai, China, 1992

- Bachelor of Science in Mechanical Engineering,
  East China University of Science and Technology, Shanghai, China, 1989

Major: Mechanical Engineering

Publications and Presentations:

W. Chen, R. N. Dave, R. Pfeffer and O. Walton,
"Numerical Simulation of Mechanofusion System ", submitted to the *Powder Technology*, 2002.

W. Chen, R. N. Dave and R. Pfeffer,
"Numerical Simulation of Mechanofusion System for Dry Particle Coating", *AIChE Annual Meeting* : Particle Technology Forum, Reno Hilton, Reno, NV, November 2001.

W. Chen, R. N. Dave and R. Pfeffer,
"Computer Simulation of Mechanofusion Process for Dry Particle Coating", *AIChE Annual Meeting* : Fourth International Particle Technology Forum, Los Angeles, CA, November 2000.

A. Mujumdar, W. Chen, M. Malik, R. Pfeffer and R. N. Dave,
"Diagnostic Analysis of Hybridization System by Numerical Simulation", *AIChE Annual Meeting* : Fourth International Particle Technology Forum, CD-ROM Proceedings, Los Angeles, CA, November 2000.

W. Chen, R. N. Dave and R. Pfeffer,
"Computer Simulation and Modeling of Mechanofusion System for Dry Particle Coating", *IFPRI Annual Meeting*, Gainesville, Florida, June 2001.

R. N. Dave, W. Chen, A. Mujumdar, W. Wang, and R. Pfeffer,
"Discrete Element Modeling for Dry Particle Coating", accepted by *World Congress on Particle Technology*, Sydney, Australia, July 2002.

W. Chen, D. Wei, R. N. Dave and R. Pfeffer,
"Numerical Simulation of Mechanofusion System for Dry Particle Coating", 6^{th} *Chinese-American Conference on Chemical Science and Technology*, NJIT, Newark, NJ, June 2000.

W. Chen and R. N. Dave,
"Binary Impact Model Analysis for DEM Simulation", 9^{th} *Uni-Tech Student Conference on Science and Technology*, NJIT, Newark, April 2000.

W. Chen, R. N. Dave and R. Pfeffer,
"Dynamic Simulation of Mechanofusion System for Dry Particle Coating", *Mini Symposium on Particle Technology*, Newark, NJIT, March 2000.

This dissertation is dedicated to my husband, Junhong and my daughter, Chenge

ACKNOWLEDGMENT

I wish to express my sincere appreciation to my advisor, Prof. Rajesh N. Dave, for his insight, encouragement and support throughout my doctoral study. Without his guidance, this research would not have been accomplished. I am grateful to Prof. Robert Pfeffer, my co-advisor, for the help and inspiration he has brought to this work. I would also like to thank Prof. Boris Khusid, Prof. I. Joga Rao and Prof. Chao Zhu for serving as members of my dissertation committee and offering valuable advice.

I would like to thank Dr. Otis Walton from Inhale Corporation, for sharing the DEM code with us, and spending much time answering my questions. Special thanks go to Dr. Colin Thornton and Dr. Kafui from Granular Dynamics Research Group of Aston University, UK, for providing the DEM simulation code for the agglomerate degradation study. I am also thankful to Mr. Haitao Xu from Cornell University, with whom I had had meaningful discussions on this research.

Dr. Moinuddin Malik, who was a visiting professor at NJIT and now works at Stevens Tech, deserves many thanks for kindly correcting errors in my proposal manuscript. I am also grateful to my friend Dawen Kou for helping me edit the final manuscript. I appreciate the friendship and cooperation of Dr. Bodhisattwa Chaudhuri, Dr. Wenqiang Wang, Dr. Michelle Ramlakhan, Ajit Mujumdar, Gregory James, and all of my research group colleagues during the course of this research. The assistance from the faculty and staff of Department of Computing Engineering, NJIT Library, Office of Graduate Studies, and Office of International Students and Faculty is also gratefully acknowledged.

I would like to express my endless gratitude to my parents, Huiwen Song and Xijun Chen, who have always supported my academic pursuit and helped me in every possible way. I am also indebted to my sister Wenjun, and my brother-in-law, Dr.

Yonghua Xu, without whom I would not have come to NJIT.

Last, but certainly not least, I want to thank my husband Junhong Feng and my daughter Chenge Feng for their love and support throughout these years.

TABLE OF CONTENTS

TABLE OF CONTENTS
(Continued)

Chapter Page

TABLE OF CONTENTS
(Continued)

Chapter **Page**

LIST OF TABLES

LIST OF FIGURES

Figure **Page**

LIST OF FIGURES
(Continued)

Figure **Page**

LIST OF FIGURES
(Continued)

Figure **Page**

LIST OF FIGURES
(Continued)

LIST OF FIGURES
(Continued)

Figure **Page**

CHAPTER 1

INTRODUCTION

1.1 Dry Particle Coating

Particle coating has many potential applications. In this process, tiny, sub-micron sized (guest or fine) particles are coated onto relatively larger, micron sized (host or core) particles. Currently, it is used mainly for forming a barrier between the particle and its environment whose purpose is extended or delayed release, separation of incompatibles, protection from water vapor, light or oxygen, and taste masking, etc.

At present, most commercial coatings of particles, grains, granules or pellets are done using a wet process. For solid particles, in the size range of about 100 microns to a few millimeters, the most popular methods employed by industry are pan coaters or fluidized bed coaters with various flow patterns and solution spraying nozzles [1] $\sim$ [3]. These methods employ suitable solvents (aqueous or organic based) to dissolve or suspend the coating materials to form the solution/suspension, and the tiny liquid droplets are sprayed to the surface of the substrate particles in the fluidized zone. During processing, the coated particles are simultaneously dried and the end product is obtained. There are several major disadvantages of the existing wet coating techniques [4] $\sim$ [7]. First is the potential environmental hazard due to the use of volatile solvents (in non-aqueous system). Second, wet coating systems are expensive to operate and require a drying stage. Third, most wet systems cannot be used successfully for particles below 100 microns. Lastly, when using coating material that does not readily dissolve or make a stable suspension, elaborate schemes may be required which may not be practical or achievable.

Contrary to wet particle coating, in dry particle coating processes, the guest particles are brought into close contact with the host particles through the application of mechanical forces or utilizing mechanochemical treatment [8] ~ [10]. Thus, either a discrete or continuous coating of guest particles can be achieved depending on operating conditions and particle properties. Particulate materials produced in this manner can not only have completely different physical or chemical properties, but also be cost effective due to the reduced use of high-priced or rare materials since the more expensive materials can be coated onto cheaper carrier material. Moreover, dry particle coating can coat host particles a few microns in diameter with nano-sized guest particles without creating a problem of dust contamination.

Dry particle coating processes are relatively new and still in the research and development stages. However, they are becoming increasingly more attractive to industry. Besides advantages mentioned above, compared with wet coating processes, dry particle coating processes are environmentally friendly, requiring no solvents, binders or even water and result in substantial cost savings because there is no need for drying the particulate products obtained. During the last ten years after it was first proposed in Japan, many machines have been used to accomplish dry coating in the laboratory [11] ~ [14]. All of these devices subject the mixture of host and guest particles to large shearing and compressive stresses and /or high impacts, which results in coating by mechanical or sometimes chemical (mechanochemistry) interactions. Mechanofusion system is one of the most promising machines that can be used for dry particle coating.

1.2 Mechanofusion System

Mechanofusion system was developed in Japan in the mid 80's resulting from research on the application of the high-powered mechanical energy to powder treatment. Figure 1.1 illustrates a schematic of Mechanofusion. It consists of a cylindrical

chamber that rotates at very high-speed, while a stationary inner piece (which has a cylindrical surface at the end) creates intense shear of the host and guest powder mix pinned against the cylindrical container. There is also a scraper, which prevents powder from caking against the wall. The clearance space between the inner piece and the chamber inner wall is adjustable, which is generally set to 4 to 5 mm. The clearance between the scraper blade and the chamber inner wall is much smaller, usually around 0.5 mm. Those clearances are adjustable, and are determined by many factors such as, powder properties, particle size, requirements of final products, and so on.

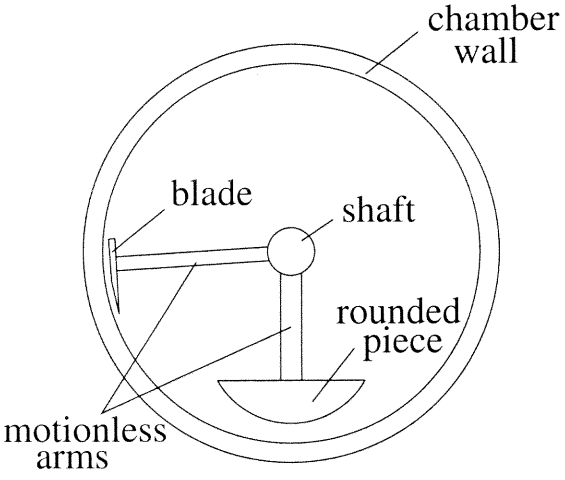

Figure 1.1 Schematic of Mechanofusion

The operation of the Mechanofusion process is very simple, but the mechanism of powder processing inside the chamber is very complicated. When the chamber rotates, powder is forced to be compressed on the chamber wall by centrifugal action. While particles passing through the converging space between the rounded piece (inner piece) and chamber wall, mechanical interactions, mainly in the form of high shear-rate collisions, take place between the particles and between the particles and solid boundaries of the chamber inner wall and the rounded piece. As the particles come out of the diverging space of the rounded piece region, they are adhered to each other and to the chamber wall. The blade serves to scrape off the powders attached to

the chamber wall. The powder mixture is then dispersed inside the chamber and gets into the inner piece region again. The powder continuously undergoes this process of compression, attrition, and frictional shearing while the chamber is rotating. As the chamber rotates at high speeds, the interactions are intensive and a considerable amount of thermo-mechanical energy is generated, which results in various effects on powder materials. The running time is kept under control to prevent burning or melting of particles.

A number of experimental studies have been devoted toward the research & development of the Mechanofusion system [15] $\sim$ [18]. However, in contrast, there has been very little effort on the theoretical analysis of the Mechanofusion system. According to the literature, there is only one reported work by Herman and Chen [19] in which a preliminary theoretical model of the Mechanofusion system was proposed to develop quantitative relationships among system variables and their effects on the system operation. In this model, The Mechanofusion effects were assumed to take place in the converging region between the inner piece and the chamber wall. This region was referred to as the inner piece "action zone". The particles within the action zone were treated as fluid-like assembly. The particle interactions with the inner piece and the chamber wall were considered. However, the interactions among the particles were neglected while creating the constitute relationship for this "action zone". Moreover, the function of the scraper was not considered at all.

1.3 The Objective of Dissertation Work

Over the years, the application of computer simulations to particulate systems has increased greatly. The early continuum techniques present large limitations to particulates , while discrete simulation techniques are much more realistic to deal with the physical behavior of particles. However, according to current literature, the dynamic

simulation technique has not yet been applied to the study of the Mechanofusion system for dry particle coating process.

Except work done by Alonso [20] [21], there is little available in terms of quantitative modeling of dry particle coating process. A qualitative explanation is given by Bannister and Harnby [22]. Three stages are identified as degradation of guest agglomerates, bonding of fines to the carriers surfaces and redistribution and exchange of fines among the carries, while the real process may not take place exactly in that order. The objective of the dissertation work is to understand dry particle coating process in the Mechanofusion system by means of dynamic simulation. The numerical studies are implemented by a system-scale simulation and a micro-scale simulation based on the methodology of the DEM. The system-scale simulation is based on a mono-dispersed system to uncover the dynamics of the system and investigate particle-particle interactions, particle-system interactions and resulted dry particle coating levels. The micro-scale simulation is carried out to understand fracture mechanism of a guest agglomerate prior to the dry particle coating process during normal interactions with host particles and with system walls.

1.4 Structure of the Dissertation

Chapter 2 gives a detailed review of DEM (Discrete Element Method), which is a very popular particulate system simulation method. It also summarizes the latest development of the method. A review of particle-particle interaction model without adhesion is presented in Chapter 3. Walton-Braun partially latching-spring model, which is applied in the DEM code for the system-scale simulation is discussed in detail in this chapter. A binary impact test, under different situations, is analyzed carefully using this force model.

The numerical simulation of Mechanofusion process is presented in Chapter 4. The system-scale simulation is performed on a mono-dispersed system to study

the dynamics of the system and examine particle-particle interactions and particle-system interactions. The simulation is based on two-dimensional mode. The coating level analysis is carried out for a hypothetical host-guest coating system through host-host interactions based on impact theory. The key points that affect coating level and system performance are thereafter studied. Dimensional analysis of a Mechanofusion system is proposed in Chaper 5 on the basis of kinetic theory. An equation for average force on particles during process is deduced to establish the correlation between a simulated system and a real system.

Particle interaction model with adhesion is presented in Chapter 6. A set of binary impact tests are carried out under combination of normal and tangential interactions. The fracture of a single agglomerates inside the system prior to dry coating process during normal interactions with host particles and system boundary is examined in Chapter 7. Finally, a summary and conclusions resulting from all the research work carried out in this dissertation are discussed in Chapter 8. Further work on the related topic is also suggested.

CHAPTER 2

DISCRETE ELEMENT METHOD REVIEW

2.1 Particulate System Simulation

Particulate system simulation provides a direct route from the microscopic details of a system such as the interactions within it to macroscopic properties of experimental interests as the state of the system. The importance of this technique is that it can provide some useful information for the particle flow which is difficult to obtain from direct experimentation. In a word, it is easy for the simulation to catch the exact moment when something of major interest happens. Particle simulation technology started from the early 1940s'. Basically, there are two mechanisms dealing with particle related simulation: kinematics method and dynamic method.

The theory of kinematics method is based on the fluid dynamics. It is mostly used to simulate dynamic systems including particle flow [23] $\sim$ [25]. Here constitutive equations are analyzed for the particle assembly. This type of continuum approach is capable of providing some useful information on macroscopic behaviors of powder assembly during process [26] $\sim$ [28]. However, it is impossible to elucidate the effects of particle geometrical factor on interaction forces between particles within the system, because the developed constitutive equations are not related with them. Particle dynamic simulations investigate the behaviors of particles in this respect. It treats the particle flow as an assembly of particles instead of a continuum. The behavior of each particle is described to related to the macroscopic behavior of the assembly.

Most particle dynamic simulations use the Discrete Element Method (DEM). The term "discrete element" refers to the fact that the simulation models the particles as a system of individual particles. In other words, this technique simulates systems consisting of discrete particles in which each individual particle is followed exactly as it interacts with other particles and with the system boundaries. Therefore, it

involves simultaneously integrating all the equations of motion for all the particles in the system. Examples of DEM model include Molecular Dynamics (MD) method, Monte Carlo (MC) techniques, Distinct Element Method, etc. "Molecular dynamics" is the term used to describe the solution of the classical equations of motion (Newton's equations) for a set of molecules. "Monte Carlo simulation" is so called because of the role that random numbers play in the method. "Distinct Element Method" is another name for DEM, which was coined by Cundall who was the first to use this type of model to study granular flow [29] $\sim$ [32].

The origins of DEM technique actually lie in the field of Molecular Dynamics (MD). In MD, the motions of molecules are followed mechanistically under the influence of external forces. Using MD simulation, it is possible to solve the dynamic problem without making any approximations within the limits imposed by machine accuracy. MD simulation has been applied widely to the study of molecular solids interactions [33] [34] and particulate systems [35] [36]. There is a thorough discussion of the details of the numerical techniques, which include over 600 references [37].

Monte Carlo simulations take use of the random nature of the molecular motion in gases to approach the problem from a statistical point of view. In Monte Carlo method, it is assumed that the velocities of individual particles are independently distributed within a velocity distribution function without regard to history or to the behavior of neighboring particles. It is unlikely that this is true in dense concentrations where particles will experience many collisions with their nearest neighbors and it is therefore unlikely that there would be no correlation between their velocities or positions. Thus, Monte Carlo method has limited usefulness in granular flow studies. Nonetheless, molecular chaos is an essential assumption in the theory of rapid granular flows so that Monte Carlo simulations do provide a forum for evaluating rapid-flow within the context of their basic assumptions [38] $\sim$ [40].

Computer simulation of dense-phase discrete particle systems was first reported by Cundall & Strack [41]. The scheme developed was termed as the "Distinct Element Method (DEM)" or referred as "Particle Dynamic Methods (PDM)" [42]. In DEM simulations, it normally assumes that the particulate flow occurs in the absence of an interstitial fluid, or the interstitial fluid can be ignored. These techniques are applicable to cases where the interstitial fluid does not play a significant role in determining the overall mechanics of the system. Within the system, the forces experienced by the particles are mainly due to the interactions with their neighbors and with the system boundaries. Therefore, in those systems, the motions of particles are not strongly influenced by any fluid that might fill the inter-particle gaps.

In a particle system, solid-solid interactions dominate the system. Therefore it is essential to establish methods of identifying contacts and modeling the contact interactions in all discrete elements methods. Most of simulations assume that particles are spheres, because it is easy to detect contacts between round particles. According to different treatment of particles interactions in the methods, DEM techniques are divided into two main categories: Hard Sphere Model (hard contact approach) and Soft Sphere Model (soft contact approach). The detail description of DEM approach and its method can be found in [43].

2.2 Hard Sphere & Soft Sphere Model

2.2.1 Hard Sphere Model

A hard sphere model assumes that all particle interactions are instantaneous collisions without any deformation. The support of this assumption is that stress levels in most granular flows are usually small so that the particle surfaces will not elastically deform to any significant degree [44] [45]. It is then a reasonable approximation to assume that the particles are perfectly rigid and cannot deform during collisions. However, this requires that any collision between such particles

must occur instantaneously. Based on the above considerations, in the hard sphere model, collisions are assumed to be instantaneous and no interpenetration of the two bodies occur. The by-product of this assumption is that there is no probability of simultaneous collisions between three or more particles so that only binary collision need be accounted for.

During the simulation, a list of collisions in order of precedence is maintained and simulation proceeds by variable time steps between successive collisions. Between collisions, the particles simply follow their kinematic trajectories which only change as the result of collisions. The collision result is determined from a inelastic, frictional collisional operator governing the dynamics of idealized binary collisions, while satisfying equilibrium and the constitutive laws. The state of the system between collisions can be easily determined if needed. The algorithm of a rigid contact model is shown in Fig. 2.1 and processes as follows: after starting the simulation, the time at which the first collision occurs is computed from the particle trajectories which is described by a simple function of time. The positions and velocities of all the particles are updated to that time. The collision result is computed, the time of the next collision to occur is found, and the average properties of the system are calculated if required and the process is repeated.

The algorithm of the hard sphere model decides that the rate at which time progresses during a simulation is inversely proportional to collision frequency. The simulation using this method is very efficient at low solid concentrations where collisions are infrequent. For the systems with large concentrations, where collisions occur frequently, the hard sphere simulation becomes very inefficient. Furthermore, the hard sphere model cannot be applied to any situation involving stagnant zones or other situations where particles are in contact for long periods of time. In this situation, the collision frequency goes to infinity and the simulation time, which progresses from collision to collision, cannot change and simulation stops.

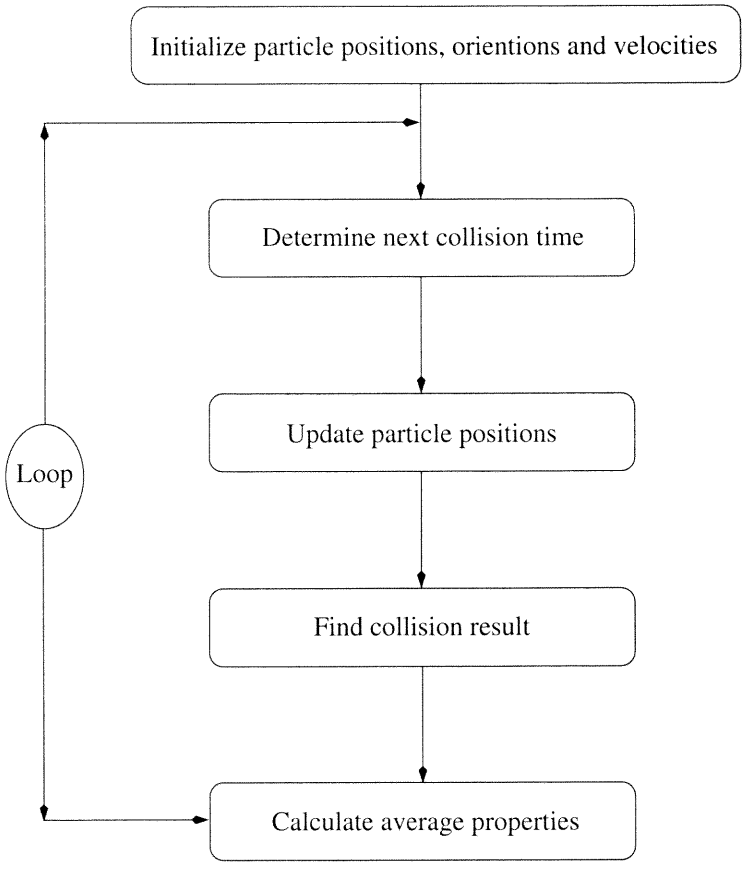

Figure 2.1 Algorithm of Hard Sphere Model

Generally, the hard contact assumption is appropriate in simulation of "molecular dynamics", in which sparse populations of bodies move around at high speed and interact by collision. The collisions are very brief, and can be modeled as instantaneous exchanges of momentum and energy may or may not be conserved by the particle pair. A good implementation of rigid-sphere collision model is described in detail by Walton [46]. Hard Sphere simulations are mainly concerned with rapid granular flows [47] [48].

2.2.2 Soft Sphere Model

In contrast to hard spheres where collisions are instantaneous, soft spheres go through certain deformations during the collisions and have a finite contact time. In the soft sphere model, a particle is allowed to be in contact with several particles simultaneously. The duration of contact is related to a non-infinite contact stiffness which is specified as a contact property. Deformation of the particle is represented as a small overlap. Consequently, the inter-particle forces are generally small, and for computational ease, the particle shape in a soft sphere simulation is not allowed to change. The force at the contact is continuously varying as the particles are being deformed. Generally, the force generated normal (and tangential) to the contact point is modeled as a simple spring. For cohesionless particles, the spring is not allowed to support tensile force and is eliminated as soon as the particles lose contact.

Each contact exerts force and moment on each of the particles involved. The total force and moment on a particle are the sum of those applied by all its contacts, combined with a body force such as gravity. The position and velocity of the particle are controlled by Newton's second law through an ordinary differential equation. Simultaneous solution of all the differential equations for all the constituent particles can determine the new state of entire system. Figure 2.2 shows flow diagram of the soft sphere model. It is simply a numerical integration. At each time step, it needs to check for new and broken contacts. The inter-particle forces are computed next and followed by integration the equations of motion. The average properties of the system are calculated at regular intervals to obtain quantities of interest. The time step of soft sphere model is usually a function of the physical properties of the discrete elements. The accurate integration of the motion equations is normally obtained by implementation more time steps ($30 \sim 50$) during a collision.

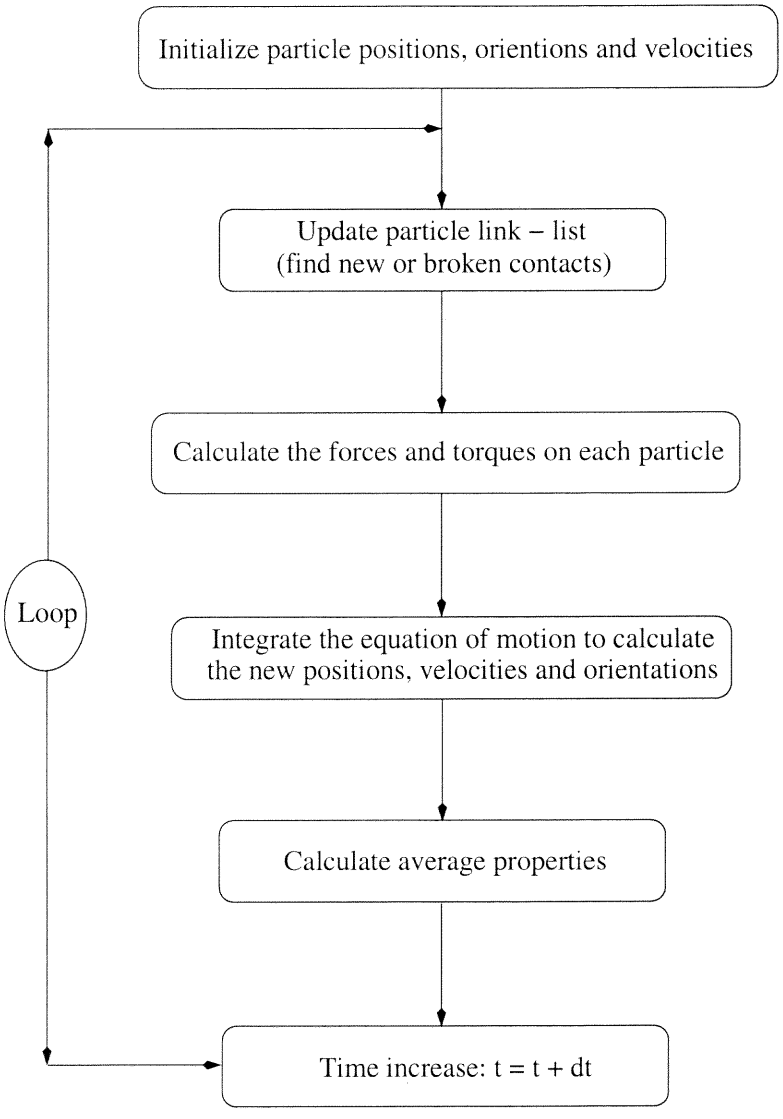

Figure 2.2 Algorithm of DEM Soft Sphere Model

Besides allowing simulation of static situations, this approach is more efficient than a rigid particle approach for dense systems, since computational time required to run a given simulation is not dependent on the particle packing. However, soft sphere models are computationally inefficient to deal with sparse system where collisions are infrequent, and most of the computer time will be spent in updating positions of the particles as they move unimpeded along their kinematic trajectories.

The Soft Sphere model is one of the more common discrete element technique compared with the hard sphere model. It is can give a better representation of what

actuarially happens during impact since it can handle a variety of inter-particle forces. This is very important in simulations of systems with very soft plastic materials or for fine powders where long-range electrostatic or van der Waals forces are important. Furthermore, soft sphere simulation can provide some information on the structure and dynamics of system including details of position, velocities, forces and energy partitions. More significantly, this approach is applicable to all configurations including both quasi-static and dynamic situations.

2.3 Development of DEM Model

Since it was first applied to study rock mass problem by Cundall in 1971, DEM has been widely used to model various problems such as granular segregation , granular mixing and agglomerate degradation [49] [50] as well as particle concentration structures in shear flows [51] [52]. Campbell gave a detail review of DEM simulation and its applications in powder flows [43]. Tsuji reviewed the recent application of discrete particle simulation method in Japan [53].

The original DEM method could not handle interstitial fluid. But recently studies have added interstitial fluid effects in an approximate manner (Tsuji et al. [54] [55]). In DEM model, particle is mostly treated as sphere for the computationally convenient purpose. Recently, simulations for two-dimensional polygonal particles have been developed by Walton [56] and Hopkins [57] and for three-dimensional polyhedral particles by Ghaboussi and Barbosa [58].

DEM modeling is not only used in simulation of quasi-static system, but is also put to simulate the rapid particle flows. Macroscopic behavior of smooth inelastic spheres in vibrating beds is investigated by Lan by three-dimensional simulation [59]. Muguruma et al use DEM to simulate the three-dimensional motions of all individual particles in a rotating mixer with two baffles [60]. Szepvolgyi et al take use this method to simulate particle motion in a high shear mixer based

on three-dimensional mode [61]. Moreover, DEM based model analysis has been applied to granular mixing [62] and particle packing study [63]. A modified distinct element method (MDEM), which considers the effect of rolling resistance at contact points, successfully simulates shear band in natural granular soils [64].

CHAPTER 3

PARTICLE INTERACTION MODELS

3.1 Introduction

In DEM simulations, it is assumed that particle-particle interactions dominate the particle-fluid interactions. The validity of the results depends on how accurately the individual particle interactions are approximated. Thus, interaction models deserve a place in any discussion of particle simulations.

Since soft sphere model can incorporate more elaborate collision interactions than hard sphere model and can handle static assemblies of particles, it is adopted in the numerical study of Mechanofusion system in the dissertation. The soft sphere interaction models are presented in this chapter. First, there is a brief review of the interaction model development. Then, a popular Walton-Braun (WB) partially latching-spring model is discussed in detail. At last, a binary impact test is studied using this model.

3.2 Development of Particle Interaction Model

In the soft sphere model, solid-solid interaction model must contain three basic components: (1) a mechanism to calculate normal force at the contact point that pushes the particle surface apart, (2) a mechanism to consider energy dissipation during the collision, and (3) a mechanism to calculate tangential force that acts on the particle surfaces.

In the early 1882, Hertz solved the problem of normal interaction (zero friction) between two elastic spheres [65]. He predicts a repulsive force that varies as the displacement to the three-halves power, i.e. $F \propto \alpha^{3/2}$, where F is resultant force and α is the displacement of two centers. However, Hertz's model is good for large deformations and not appropriate for granular flow where interactions are too small to deform the macroscopic shape of the surface. Therefore, in their first model,

Cundall and Strack simply used linear springs to model normal and tangential interactions with the tangential force limited by a Mohr-Coulomb criterion. The energy loss is implemented by a dash-pot. Incorporating with the finite-element analysis, Walton suggested a nearly linear response to displacement for the interaction of the elasticity and the plasticity. In their model, Walton and Braun used a "latched spring" to represent normal inter-particle loadings, where energy loss is incorporated by difference between loading and unloading stiffness. Based on above two models, Thornton suggested a combined spring for normal interaction with initial loading acting as nonlinear (Hertian) followed by linear relationship of force and displacement. For the last two models, frictional force and tangential compliance are incorporated in a complicated way based on the work of Mindin and Deresiewicz [66], which assume Hertzian behavior in the normal direction and predict complex hysteretic behavior in the tangential direction whenever the frictional limit has been exceeded (i.e., when there is slip between the particle surfaces). However, their work was based on the quasi-static behavior assumption.

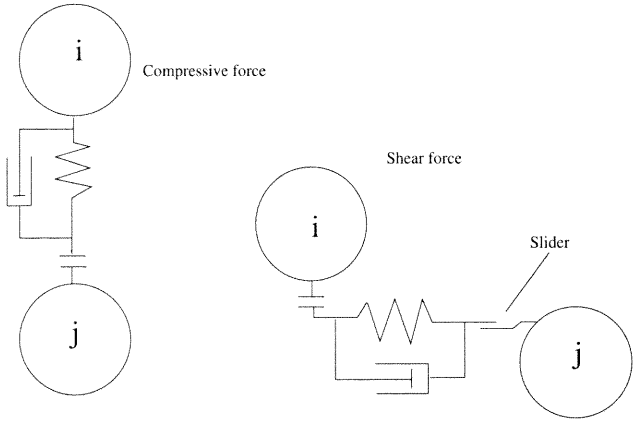

Figure 3.1 Models of contact forces

Generally, the implementation of the contact model to DEM simulations based on the above considerations. The forces applied in the normal direction are usually assumed to act as nonlinear or linear springs which generating a force proportional to

the overlap between the particles. Meanwhile, the spring is connected in parallel to a linear dashpot to provide the energy dissipation. The tangential forces that arose from inter-particle friction are simulated in the similar way. For instance, Cundall and Strack [30] formulate a simple model using a spring, dash-pot and slider as shown in Fig. 3.1 to model particle-particle interaction in quasi-static granulate flow. Walton and Braun formulated a similar model, called "latching spring" model [67]. A detailed explanation of "latching spring" model is presented in the rest of the chapter.

3.3 Walton-Braun Partially Latching-Spring Model (Non-Cohesive)

Partially latching-spring model (Fig. 3.2) was proposed by Walton-Braun for an elastoplastic material [68] $\sim$ [70]. They used a "latching spring" that loads with one spring constant and unloads with another as a way of incorporating the energy dissipation. They found this to be closer to results of elastic-plastic finite-element modeling of impact of the round particles.

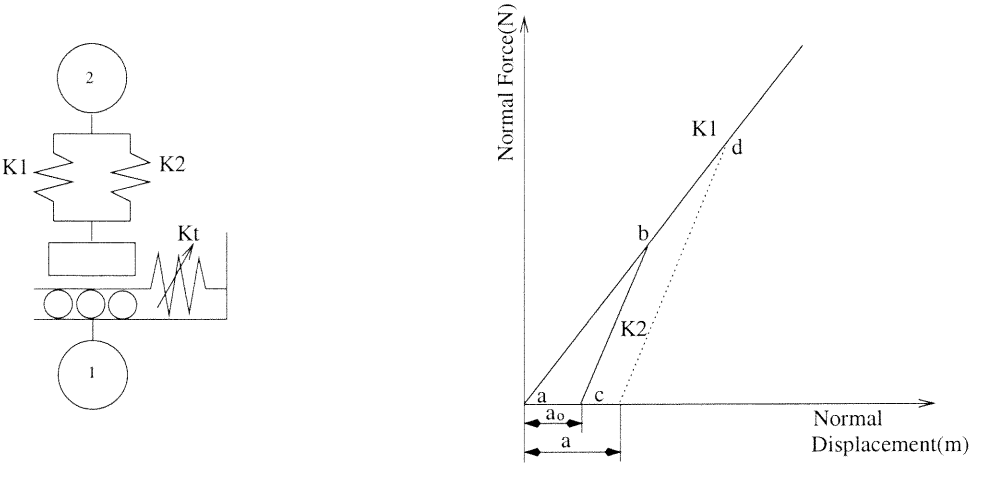

Figure 3.2 Partially latching-spring model

stage, with spring constant K_2, while a finite plastic deformation occurs. K_2 can be decided from the given coefficient of restitution e, independent of impact velocity, which is defined as

$$e = \left(\frac{K_1}{K_2}\right)^{\frac{1}{2}} \tag{3.1}$$

The normal force is given by

$$\begin{cases} N_l = K_1\,\alpha & \text{for loading} \\ N_u = K_2\,(\alpha - \alpha_o) & \text{for unloading} \end{cases} \tag{3.2}$$

where α is the relative approach (overlap) after initial contract, and α_o is the finite plastic deformation, i.e., α_o is the value of α where the unloading curve goes to zero.

The tangential force model used here is incrementally slipping friction model suggested by Walton-Braun too. Effective tangential stiffness in the direction parallel to the existing friction forces. It decreases with tangential displacement until it is zero when full sliding occurs. In the present 2D surface model, the tangential displacement parallel to the current friction force and the displacement perpendicular to the existing friction force are considered separately. They are combined vectorially and their sum is checked against the total friction force limit, μF_N.

The effective tangential stiffness, K_T is given by

$$K_T = \begin{cases} K_o\left(1 - \frac{T - T^*}{\mu N - T^*}\right)^{\nu} & \text{for slip in one direction } (T \text{ increases}) \\ K_o\left(1 - \frac{T^* - T}{\mu N + T^*}\right)^{\nu} & \text{for slip another direction } (T \text{ decreases}) \end{cases} \tag{3.3}$$

where T is the total tangential force; μ is the coefficient of friction; N is the total normal force; ν is a fixed parameter usually set to 1, and T^* is the loading reversal value, which is initially zero, is subsequently set to the value of the total tangential force, T, whenever the the magnitude changes from increase to decrease, or vice versa. It is scaled in proportion to any change in the normal force from the previous time step. K_o is the initial tangential stiffness and is assigned by the equation:

$$K_o = \begin{cases} \tau\,K_1 & \text{loading} \\ \tau\,K_2 & \text{unloading} \end{cases} \tag{3.4}$$

where τ is the ratio of tangential and normal stiffness, and normally it is less than 1.0.

The new tangential force T' (parallel to friction force) is given by the expression

$$T' = T + K_T \, \Delta s \tag{3.5}$$

where Δs is the amount of relative surface displacement between the contact particles during time step Δt (see Eq. 3.10 through Eq. 3.12 for further explanation).

Thus, in order to calculate the total tangential force acting between each pair of particles, it needs to keep only two history dependent quantities, T and T^* from one time step to the next. The simulation model assumes that the displacements from one time step to the next are relatively small.

The following is detailed calculation steps for tangential force:

1. Calculate the unit normal vector of the contact between I and J, $\hat{k}_{ij}$, treat it as tangent plane.

$$\hat{k}_{ij} = \frac{(\vec{r}_i - \vec{r}_j)}{\mid \vec{r}_i - \vec{r}_j \mid} \tag{3.6}$$

   where $\vec{r}_i$, $\vec{r}_j$ is the position vector for particle I, and particle J, respectively.

2. The tangential force from the previous time step $\vec{T}_{old}$ is projected onto the current tangential plane.

$$\vec{T}_o = \hat{k}_{ij} \times \vec{T}_{old} \times \hat{k}_{ij} = \vec{T}_{old} - \hat{k}_{ij}(\hat{k}_{ij} \cdot \vec{T}_{old}) \tag{3.7}$$

3. Normalize the projection friction force to the old magnitude to obtain new " starting " value for the friction force $\vec{T}$.

$$\vec{T} = \mid \frac{\vec{T}_{old}}{\vec{T}_o} \mid \vec{T}_o \tag{3.8}$$

4. Calculate the unit vector of this friction force.

$$\hat{t} = \vec{T} / \mid \vec{T} \mid \tag{3.9}$$

5. Calculate the relative surface displacement during the last time step and project it onto the contact tangent plane.

$$\begin{aligned}\Delta\vec{s}^{\,n-\frac{1}{2}} &= [\hat{k}_{ij}\times(\vec{v}_j^{\,n-\frac{1}{2}}-\vec{v}_i^{\,n-\frac{1}{2}})\times\hat{k}_{ij}+r_i(\vec{w}_i^{n-\frac{1}{2}}\times\hat{k}_{ij})+r_j(\vec{w}_j^{n-\frac{1}{2}}\times\hat{k}_{ij})]\,\Delta t \\ &\approx \Delta\vec{r}_{ij}-\hat{k}_{ij}(\hat{k}_{ij}\cdot\Delta\vec{r}_{ij})+[r_i(\vec{w}_i^{n-\frac{1}{2}}\times\hat{k}_{ij})+r_j(\vec{w}_j^{n-\frac{1}{2}}\times\hat{k}_{ij})]\,\Delta t \quad (3.10)\end{aligned}$$

$\Delta\vec{r}_{ij}=\vec{r}_{ij}^{\,n}-\vec{r}_{ij}^{\,n-1}$ is the change in the relative position vector during the last time step; $\vec{v}$ is the velocity, $\vec{w}$ is angular velocity, and r is the sphere radius, with subscript i and j indicating sphere I and J, respectively, and Δt is the time step.

6. Calculate the displacement that parallel to the " old " friction force.

$$\Delta\vec{s}_{||}=(\Delta\vec{s}^{\,n-\frac{1}{2}}\cdot\hat{t})\hat{t} \quad (3.11)$$

7. The perpendicular displacement is

$$\Delta\vec{s}_{\perp}=\Delta\vec{s}^{\,n-\frac{1}{2}}-\Delta\vec{s}_{||} \quad (3.12)$$

8. Decide the magnitude of $\vec{T}^*$. If the value of the normal force, F_N, changes from one step to the next, then the value of T^* in Eq. 3.3 is scaled in proportion to the change in normal force.

$$\vec{T}^{*\prime}=\vec{T}^{*}\mid\vec{F}_N^{n}/\vec{F}_N^{n-1}\mid \quad (3.13)$$

9. Calculate current stiffness for tangential force with $T^{*\prime}$ substitute for T^* in Eq. 3.3 for K_T.

10. Calculate the component of the new friction force parallel to the old friction force.

$$\vec{T}_{||}=\vec{T}+K_T\Delta\vec{s}_{||} \quad (3.14)$$

11. The perpendicular part is

$$\vec{T}_{\perp} = K_o \Delta \vec{s}_{\perp} \tag{3.15}$$

12. New tangential force

$$\vec{T}' = \vec{T}_{\parallel} + \vec{T}_{\perp} \tag{3.16}$$

13. Normalize to friction limit $\mu \vec{F}_N$ to get $\vec{T}$

$$\vec{T} = \vec{T}' * \frac{\min(\vec{T}', \mu \vec{F}_N)}{\vec{T}'} \tag{3.17}$$

3.4 Binary Impact Analysis by WB Model

The partially latching-spring model has been widely used in granular flow problems. However, in the available literature, except for the work of Walton [46] not much attention has been paid on the analysis of interaction forces predicted by the model. For this reason, a detailed analysis of the partially latching-spring model was carried out by examining the interaction of two (spherical) particles under planar, central and oblique impacts (Fig. 3.3). Some results from this analysis are presented here.

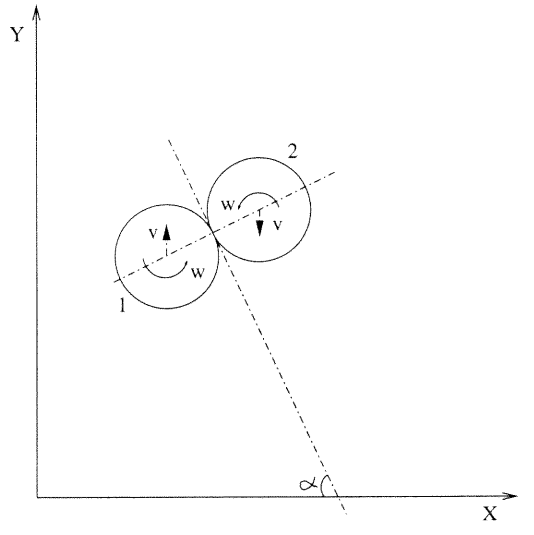

Figure 3.3 Impact of two spheres under angle α, velocity v and rotational speed w

The results are intended to show the effects of approach velocity, angle of impact, and rotation of particles on the predicted force-deformation characteristics of the model. Table 3.1 lists the parameters for contact particles.

Table 3.1 Parameters of the particle

Radius of particles	0.2 mm
Density of particles	1.20×10^3 kg/m^3
Normal stiffness (for loading)	20000 kg/s^2
Particle-particle coefficient of friction	0.4
Coefficient of restitution	0.85

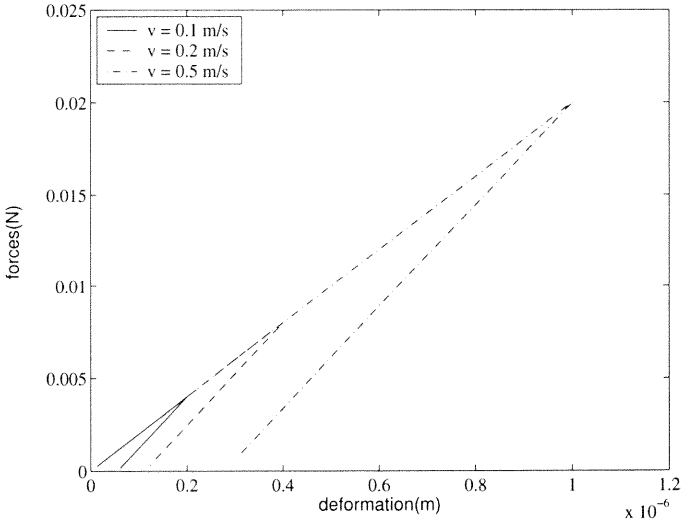

Figure 3.4 Force-deformation vs. impact velocity (normal impact)

Figure 3.4 shows the effect of impact velocity on force-deformation (loading path) under central impact (or normal impact) without considering angular speed of particles. Figure 3.5 shows the case under oblique impact ($\alpha = 30^o$). The loading path is proportional to impacting velocity under either case. The larger impact velocity induces to the longer loading path, i.e., larger deformation and impact force. Figure 3.6 and Fig. 3.7 show effect of impact angle on the loading path and force path under the same impact velocity, respectively. The change of loading path is inverse to impact angle. The larger impact angle induces to the shorter loading

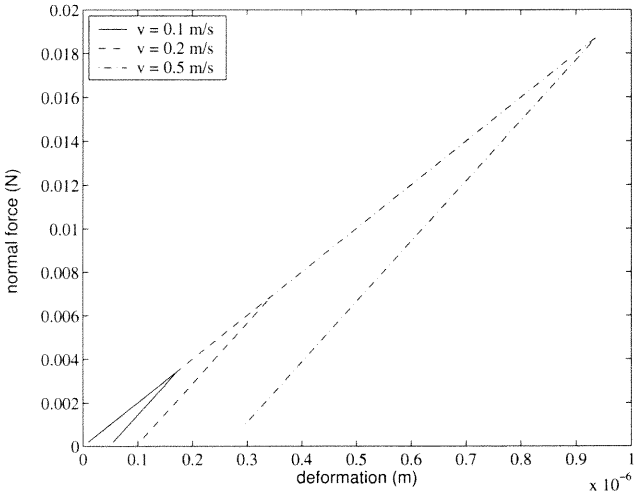

Figure 3.5 Force-deformation vs. impact velocity (impact angle = 30^o)

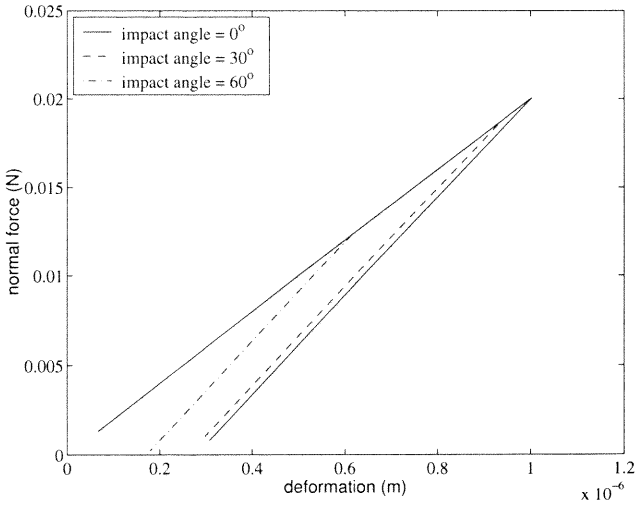

Figure 3.6 Force-deformation vs. impact angle at v = 1.0 m/s

path. However, the larger impact angle causes larger tangential force during impact and when the impact angle goes to some degree, the slipping of force happens during the unloading period. Figure 3.8 shows effect of angular speed of particles on force path under the same impact velocity and impact angle. It illustrates that tangential force between particles increases with angular speed of particles.

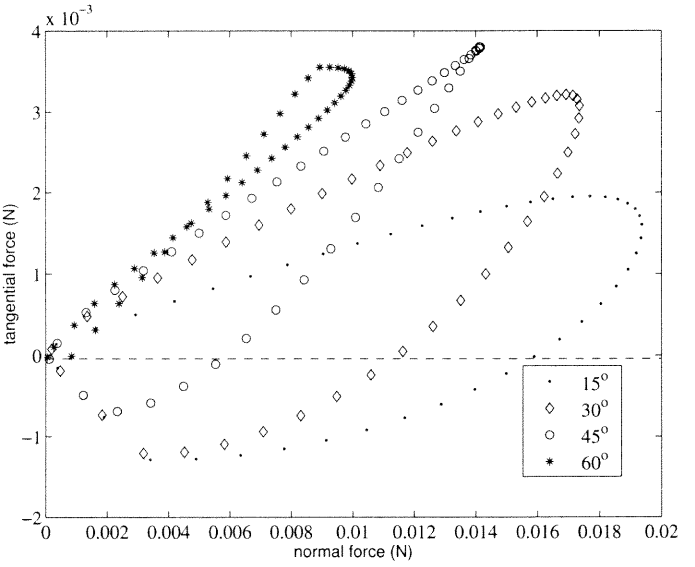

Figure 3.7 Force path vs. impact angle under same impact velocity ($v = 1.0$ m/s)

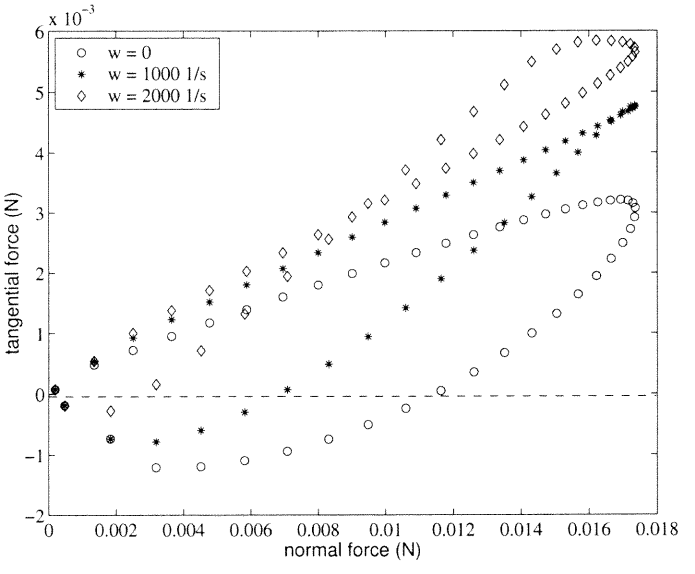

Figure 3.8 Force path vs. rotation speed of particles under same impact angle ($\alpha = 30^o$) and impact velocity ($v = 1.0$ m/s)

CHAPTER 4

NUMERICAL SIMULATION OF MECHANOFUSION SYSTEM

4.1 Introduction

Since it was invented around 15 years ago, Mechanofusion system has been widely studied in experiment. However, there is less literature about the theoretical study of the Mechanofusion powder processing, except a preliminary model that was proposed by Herman and Chen based on fluid mechanism (the model is briefly reviewed in Chap. 1). The presented work is the first attempt on the numerical simulation of a Mechanofusion system based on DEM technique [71] $\sim$ [73]. The numerical study is performed on a mono-dispersed system based on two-dimensional simulation. In the numerical model, interactions among particles and between particles and boundary (cylinder chamber & inner piece) as well as particles and blade (scraper) are calculated by force model algorithm. Diagnostic analysis is carried out to compare two systems, where only difference between them is that in one of them doesn't have a scraper. Visualization of the particulate patterns inside the system and results of diagnostic analysis clearly demonstrate the effect of scraper on the system. The force applied on the inner piece is calculated and is qualitively comparable with experimental results. Average forces on particles due to interactions with other particles and vessel parts are also calculated and categorized into four function areas. The results show particles will experience different force while passing through the different areas. The numerical mechanism and approach of simulation study of Mechanofusion system for dry particle coating process are presented in detail in this chapter.

The simulation study is performed on a system scale. Because of the large difference between size of host particles and that of guest particles, in the system-scale simulation, only host particles are taken into consideration. The purpose of the system-scale simulation of is to understand the dynamics of the system which may

help explain the mechanism of dry particle coating and effect of key parameters on the coating outcome.

4.2 Description of the Model

4.2.1 Geometry Model

In the model (2D), as shown in Fig. 4.1, the outer circle represents the Mechanofusion chamber. It is an outer-boundary of the system. The eccentric inner circle represents the inner rounded piece (i.e., inner piece), see Fig. 1.1 for reference. The radius of the inner circle is decided by the corresponding shape of the inner piece. The exact modeling of the scraper is rather complicated. In order to simplify the simulation, the model just considers the basic function of scraper within the system. In Fig. 4.1, the scraper is represented by a set of fixed particles, placed at an angle as shown. This closely mimics the actual placement of scraper inside the chamber. It is noted that other configurations, i.e., positioning the particles at a higher angle resulted in excessive flow impediment, unlike that seems to occur in the physical system. In addition, in the numerical model, there is zero clearance between scraper particles and the chamber, and these fixed particles are taken to be of the same size as the powder particles.

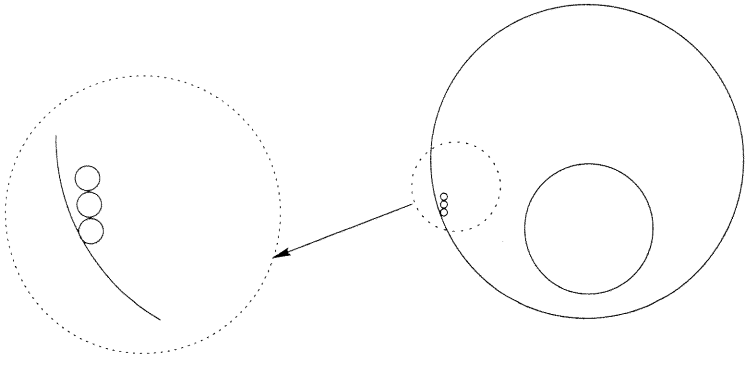

Figure 4.1 Simulation model, showing the detail of the model of the scraper

4.2.2 Force Model

A detailed description of force model that is used in this simulation is provided in the Chap. 3. Here a brief summary is given to keep the chapter integral. The force model is proposed by Walton and Braun. During a simulation, particles are assumed to be frictional, elastic-plastic spheres. For the normal force, it is calculated by a partially latching-spring model. The loading resistance force is calculated by a linear spring, with the spring constant given by k_1; a stiffer linear spring is used during the unloading (restoration) stage, with spring constant k_2, while a finite plastic deformation occurs. The tangential force model used here is incrementally slipping friction model. The new tangential force is calculated by the old tangential force and is related with loading history and direction.

Besides this, there are two points deserving a brief discussion:

- Time step, Δt: The time step during the simulation is calculated by the equation,

$$\Delta t = \frac{\pi\, e \sqrt{\frac{m_i}{2K_N}}}{n} \tag{4.1}$$

where e is restitution coefficient, m_i is mass of particle, K_N is spring stiffness for loading and n is the desired number of time steps for one contact (for this simulation $n = 40$). Equation 4.1 shows that calculation time step is proportional to particle mass, i. e., proportional to particle size. However, the time step is inversely proportional to spring stiffness K_N. The larger stiffness will cause smaller time step.

- Normal stiffness, K_N: As shown in Eq. 4.1, the value of K_N is closely related to the calculation time step. If the value of K_N is very high, the time step will be very small and computation time will be very long. However, if the value of K_N is very small, the particle will be too "soft". The deformation of a particle during the simulation will be out of the model limitation, which requires that

maximum deformation of the particle during the simulation should be less than 1 % of particle diameter. Therefore, based on the impact mechanics and condition that maximum deformation of particles is less than 1 % of particle diameter, the normal stiffness can be calculated by equation,

$$K_N = 0.01\pi E r_i \tag{4.2}$$

where E is Young's modules and r_i is particle radius.

4.2.3 Zone Mapping and Volume Fractions of a Particle

In order to analyze the dynamics change inside the system, several zones are defined along the radius of the chamber as shown in Fig. 4.2. Each zone has the same volume, $V_i = V/N$, where V is the volume of the chamber and N is number of zones. The number of zones is selected so that the height of each zone is equal or greater than the maximum diameter of particles. Under this condition, the largest particle will not occupy more than two zones at a time instant. In this study, there are seven zones along the chamber radius.

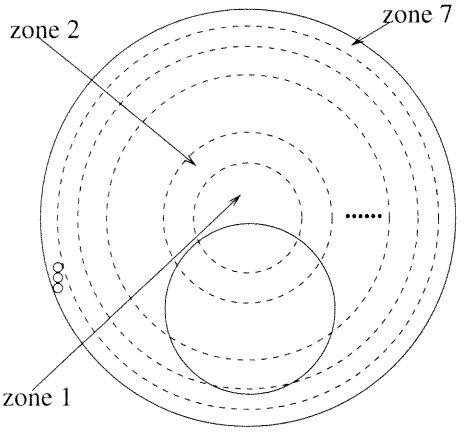

Figure 4.2 Zone mapping

During the dynamic modeling, particles are supposed to be frozen in each very short time step to calculate macroscopic quantities such as kinetic energy and pressure. By assuming uniform materials, it is assumed that the ratio of a material

fraction is equal to the ratio of volume fraction. If a particle occupies one zone in the time instant, calculation of the volume fraction is not necessary because all of it belongs to the one particular zone.

Consider particle i to be occupied by two zones as shown in Fig. 4.3, then the upper fraction belongs to the zone k and lower fraction belongs to the zone $k+1$. The distance of particle center to the zone k is represented by a. It is calculated using equation,

$$a = l_{oi} - r_k \tag{4.3}$$

where l_{oi} is the distance of particle $i's$ center to chamber $o's$ center and r_k is the radius of zone k.

The volume of particle i in zone k is given by

$$V_k = \int_a^r \pi x^2 dy = \frac{2}{3}\pi r^3 - \pi a(r^2 - \frac{1}{3}a^2) \tag{4.4}$$

where r is the the radius of particle, and $x = \sqrt{r^2 - y^2}$.

Therefore the volume fraction of particle i in zone k is

$$rpos(i) = \frac{V_k}{V_t} = \frac{\frac{1}{2}V_t - \pi a(r^2 - \frac{1}{3}a^2)}{V_t} \tag{4.5}$$

where V_t is the volume of particle i.

The volume fraction of particle i in zone $k+1$ is

$$rneg(i) = 1 - rpos(i) \tag{4.6}$$

4.2.4 Simulation Approach

In a dynamic simulation such as this, the computation time is a critical issue. The number of particles should be large for the simulation to capture the essential features

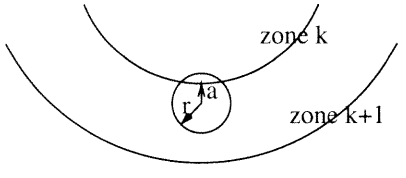

Figure 4.3 Volume fraction when two zones are occupied by a particle i

of the particulate flow. However, the number of particles determines the computation time, and hence the computational cost. Theoretically, the computation time is proportional to the square of the number of particles, but it seems to increases exponentially with the number of particles, as shown in Fig. 4.4. One way to limit the number of particles in the system is by using a two-dimensional configuration for the system. Dimensional reduction is equivalent to assuming the system to be either very long or very narrow in the third (eliminated) dimension. In the former case, the flow pattern becomes independent of the third direction [74]. Approximation for the latter case becomes possible as the particulate flow becomes dominantly two-dimensional. Here, assuming the particulate flow to be in the transverse plane, two-dimensional simulations were employed for the present studies. In addition, the simulation system is taken to be smaller than the actual system in order to keep the number of particles small hence computable on time. The parameters used for the simulation system are given in Table 4.1. The particle properties such as the friction coefficient are selected based on the properties of PMMA.

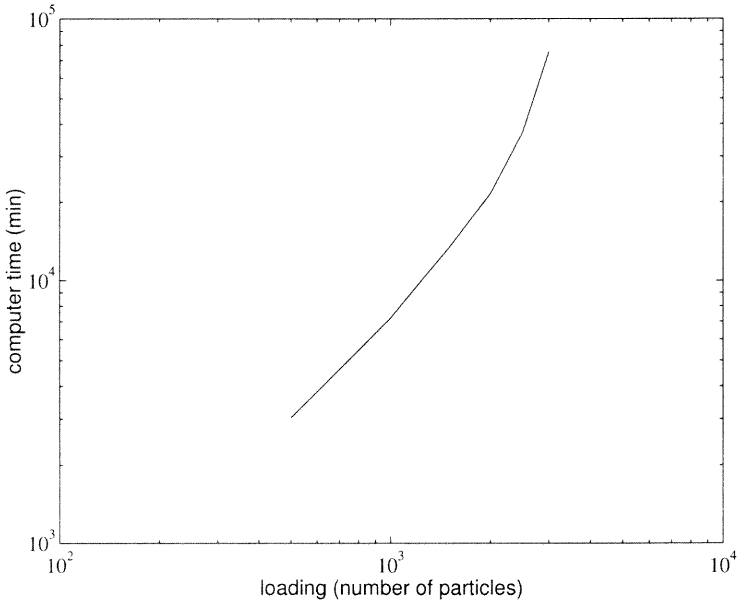

Figure 4.4 Computer time as a function of loading of particles

Table 4.1 Parameters of the system

Radius of particles	0.2 mm
Number of particles	1500
Density of particles	1.20×10^3 kg/m^3
Diameter of outer circle	25 mm
Diameter of inner circle	10 mm
gap size	1.6 mm
Rotational speed of chamber	2000 rpm
Normal stiffness (for loading)	20000 N/m
Particle-particle coefficient of friction	0.4
Particle-solid boundaries coefficient of friction	0.5
Coefficient of restitution	0.85

4.2.5 Numerical Method

During a simulation, cylinders (chamber and inner-piece) are treated as boundary particles and scraper as fixed particles. They act as discrete elements of the system which interact with system particles. The algorithm of a computational model (soft sphere) is illustrated in Fig. 2.2. At the beginning of the simulation, particles are randomly positioned inside the system with some overlaps between them (overlap is not allowed between particle and boundary particles or fixed particles). Initially, particles are assigned with small random velocities, however, the net momentum of the system is zero. For each time step, inter-particle forces are calculated for all contacting particles using the contact force model. In this study, the simulation is implemented in two-dimensional mode, the gravity force, which is in z-direction is not considered. Summation of related forces acting on each particle is carried out on x and y-direction (2D) respectively. The new particle translational and rotational acceleration (in x-direction) are calculated by Newton's equations of motion:

$$\begin{cases} \dot{v}_x^n = \frac{F_{i_x}^n}{m} \\ \dot{\omega}_x^n = \frac{M_{i_x}^n}{I} \end{cases} \tag{4.7}$$

where the superscript n refers to the current time step; $m = \frac{1}{6}\pi d^3\rho$ is particle mass, here d is particle diameter, and ρ is particle density; $I = \frac{1}{10}md^2$ is particle moment of inertia; F_{i_x} and M_{i_x} are the inter-particle force and moment acting on the particle due to interaction with others. Similar equation can be written for y-direction. The new velocity and position of the particle are obtained by explicit integration of Eq. 4.7 via the time-centered, finite-difference "leap-frog" method [37]. The finite difference equations for the particle are

$$\begin{cases} v_x^{n+\frac{1}{2}} = v_x^{n-\frac{1}{2}} + \dot{v}_x^n \Delta t \\ \omega_x^{n+\frac{1}{2}} = \omega_x^{n-\frac{1}{2}} + \dot{\omega}_x^n \Delta t \end{cases} \tag{4.8}$$

for translational and rotational velocity in x-direction. The new particle position is updated by:

$$x^{n+1} = x^n + v_x^{n+\frac{1}{2}} \Delta t \tag{4.9}$$

for x-direction. Similarly, the corresponding equations for motion can be written for y-direction. After obtaining new positions and velocities for all the particles, the program repeats the cycle of updating contact forces and particle positions. Checks are incorporated to find new contacts and delete broken contacts. During the simulation, average properties of the system are calculated and output at regular intervals to obtain interest quantities.

4.3 Comparison Study

4.3.1 Two Mechanofusion Systems

In the numerical studies, first, two geometric models of Mechanofusion system are studied. The two models differ only in that scraper is excluded in one model. Figure 4.5 shows the geometric model with scraper (a) and without scraper (b). A series of simulation experiments are performed in order to understand the effect of scraper. The number of particles in the system is 1500 and gap between the inner

piece and the chamber boundary is 1.6 mm. The rotational speed of the chamber for this comparison study is 2000 rpm.

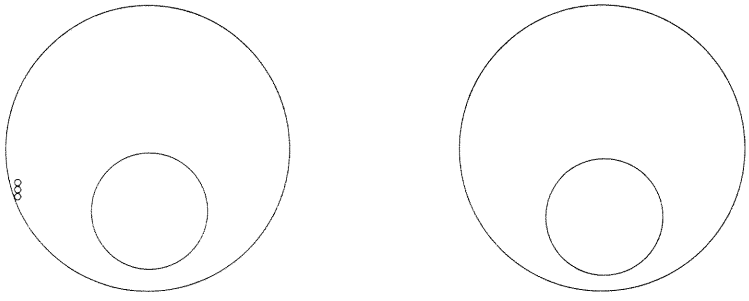

Figure 4.5 Two geometric models

Figure 4.6 and Fig. 4.7 show the snap-shots of the patterns within the system with scraper and without scraper, respectively. The initial condition for two systems is same: particles are randomly put inside the system which allows overlap between them and with small initial velocity. The total running time for this simulation is 10 seconds. From these figures, the time evolution of the particle patterns can be observed. Figure 4.6 shows the pattern having scraper inside the chamber. It can be seen that during the operation, particles are generally dispersed within the chamber. However, the pattern shown in Fig. 4.7 for the system without scraper, is quite different from that shown in Fig. 4.6. As the time passes, more and more particles get attached to the chamber wall because of the centrifugal force, and hence the particles are not evenly dispersed within the system. These results are somewhat in line with the expectation.

4.3.2 Computing Diagnostic Quantities

The quantities of interest for diagnostic analysis of the simulated system are the time-averaged values of volume fraction, velocity, granular temperature, and so on. The time over which averages are taken must be long enough compared to the typical time taken by any particle interaction (e.g. particle-particle or particle-wall collision), but

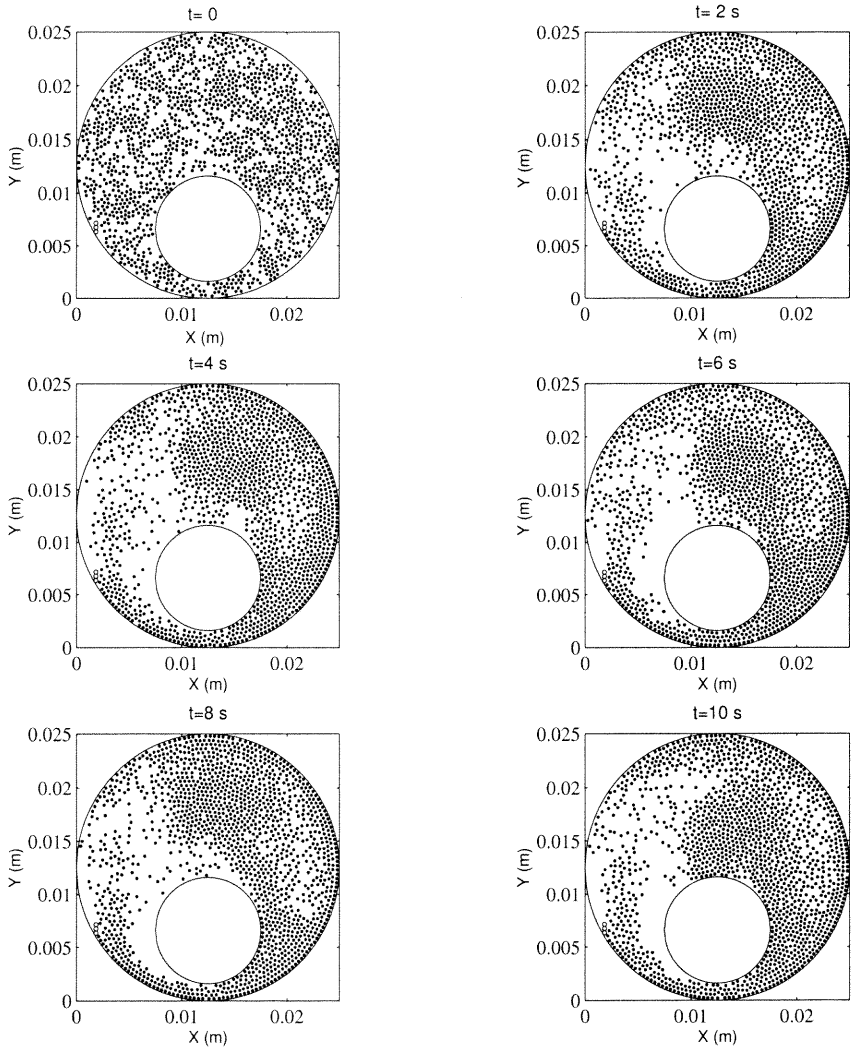

Figure 4.6 Particle pattern for the system with scraper versus time (10 s)

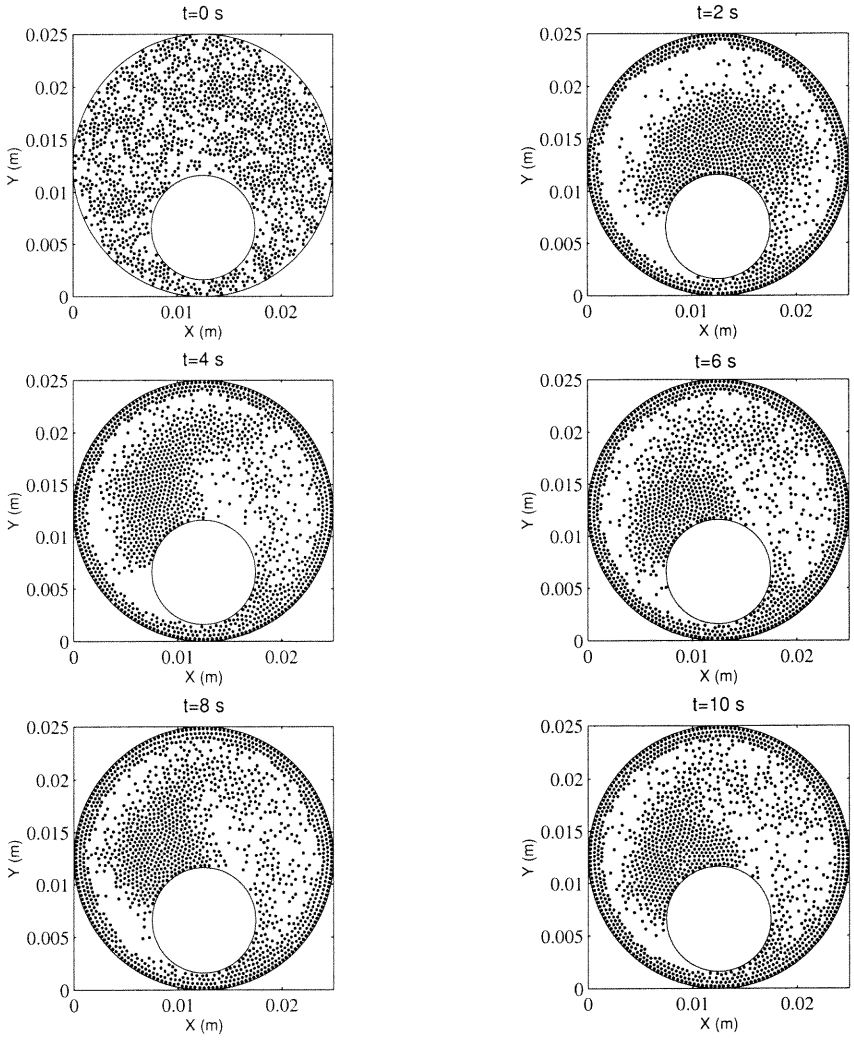

Figure 4.7 Particle pattern for the system without scraper versus time (10 s)

it should be short compared to the time scale of major changes in the properties of interest.

The snap-shots of particle patterns inside these systems show qualitatively the difference between systems with and without scraper. To obtain a quantitative understanding, the time-averaged kinetic energy, pressure, etc. can be computed. Such computations provide an understanding of the dynamics of the system. For these two systems, the diagnostic analysis is carried out to compare the difference in the dynamic condition inside the two systems. Each diagnostic quantity is a volume average inside each zone during a time period (set to 2 seconds in this case). Since the simulation is performed in two-dimensional, the volume is obtained by setting the third direction, i.e., the thickness of each zone to be same dimension as particle diameter.

1. Rotational kinetic energy. The rotational kinetic energy of particles inside zone k is given by,

$$\mathbf{E}_r^{(k)} = \frac{1}{2V_k} \sum_{i \in k} \mathbf{I}_i \left[\omega_{ix}^2 + \omega_{iy}^2 + (\omega_{iz} - \omega)^2 \right] \tag{4.10}$$

where V_k is volume of zone k, ω is the rotational speed of the Mechanofusion chamber; ω_{ix}, ω_{iy}, ω_{iz} are the components of the angular velocity of particle i (which falls in zone k in the time instant); $\mathbf{I}_i = \frac{2}{5} m_i r_i^2$ is moment of inertia of particle i; and m_i and r_i are the mass and radius of particle i. In the case of two-dimensional simulation, $\omega_{ix} = \omega_{iy} = 0$. In the above, the rotation speed of the chamber is subtracted so that the effect of the rigid body rotation is eliminated. For instance, if all the particles were glued to the chamber, the rotational kinetic energy of each particle will be $\mathbf{I}_i \, \omega^2$. Hence, the computed total rotational kinetic energy as per equation above will be zero.

As seen from Fig. 4.8, the rotational kinetic energy of the particles in the system with scraper increases radially outward, which means boundary zones have larger rotational kinetic energy. However, for the system without

scraper, Fig. 4.9, rotational kinetic energy along the boundary zone goes down. This implies that without the scraper, particles basically stick to the boundary during the processing.

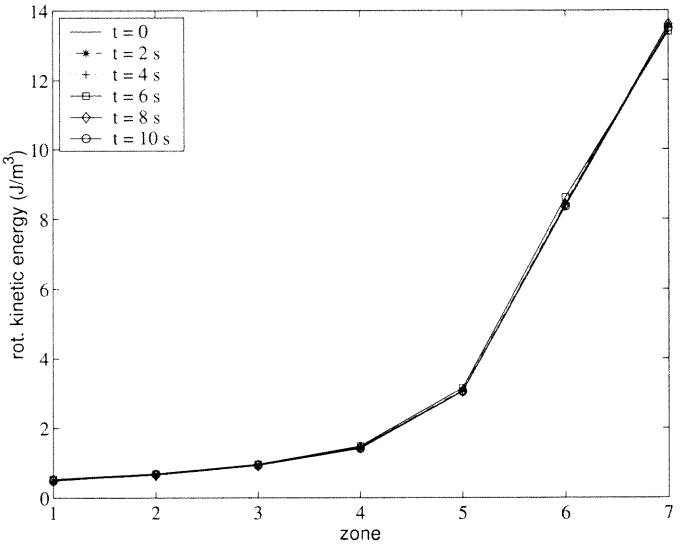

Figure 4.8 Rotational kinetic energy distribution inside the chamber for the system with scraper

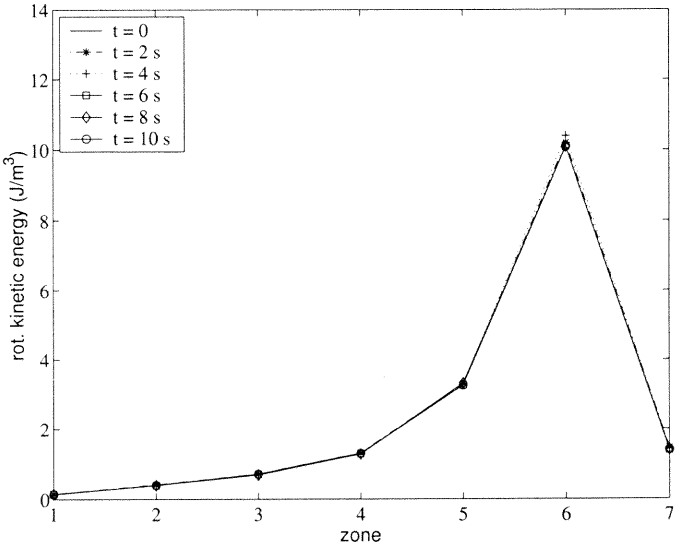

Figure 4.9 Rotational kinetic energy distribution inside the chamber for the system without scraper

2. Deviatoric kinetic energy. This is calculated by the equation,

$$\mathbf{E}_t^{(k)} = \frac{1}{2V_k} \sum_{i \in k} m_i \left[(v_i - \bar{v}_k)^2 \right] \tag{4.11}$$

where v_i is particle velocity and $\bar{v}_k$ is the average velocity inside zone k where particle i falls in the current time step. The value of the translational kinetic energy computed by this equation is deviatoric. The average velocity of the zone, which does not have any contribution to the collisions between the particles, is subtracted from the absolute value of the particle velocity to get the comparative kinetic property of the system. Figure 4.10 and Fig. 4.11 show deviatoric kinetic energy distribution inside the chamber for the system with scraper and without scraper. From Fig. 4.10 it can be seen that for the system that has scraper the deviatoric kinetic energy is evenly distributed inside the system. However, for the system without scraper, Fig. 4.11, the deviatoric kinetic energy is much smaller compared with the value of the system with scraper. The exception happens in the zone that has the inner piece boundary which induces the larger fluctuation of the particles similar as the scraper function inside the system with scraper.

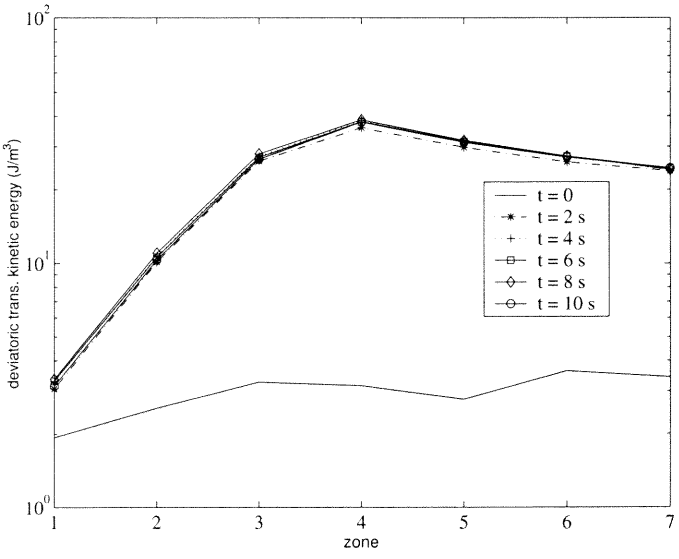

Figure 4.10 Deviatoric kinetic energy distribution inside the chamber for the system with scraper

3. Pressure distribution. For the particulate dynamic system like Mechanofusion, the pressure inside the system is calculated based on the work by Ladd [75],

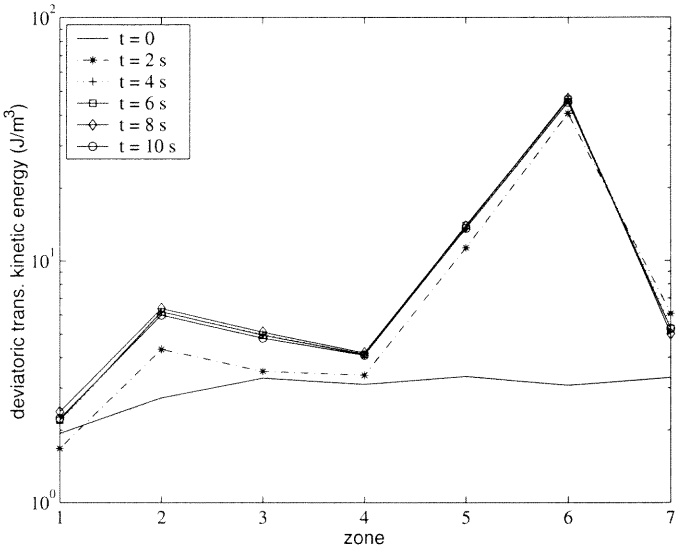

Figure 4.11 Deviatoric kinetic energy distribution inside the chamber for the system without scraper

given by,

$$\mathbf{P}_t^{(k)} = \frac{1}{3V_k}\left[\sum_{i\in k} m_i(v_i - \bar{v}_k)^2 + \sum_{i\in k, i>j} F_{ij}R_{ij}\right] \tag{4.12}$$

where F_{ij} is the repulsive force acting between particle i and j, and R_{ij} is the distance between particle i and particle j. The first term in the above expression is the kinetic contribution to the granular pressure due to the motion of the particles corresponding to the average velocity field at the location of particle i, and second term is the potential or collisional contribution to the pressure due to the forces of interaction between particles.

Pressure distribution for the system with scraper and without scraper is shown in Fig. 4.12 and Fig. 4.13, respectively. It can be seen that basically the pressure along the boundary zone is very large compared with other zones. The value inside boundary zone of the system without scraper is relatively larger because of dense packing of the particles along the boundary. However, the pressure distribution inside the system with scraper is more uniform along the zones compared with the system without scraper.

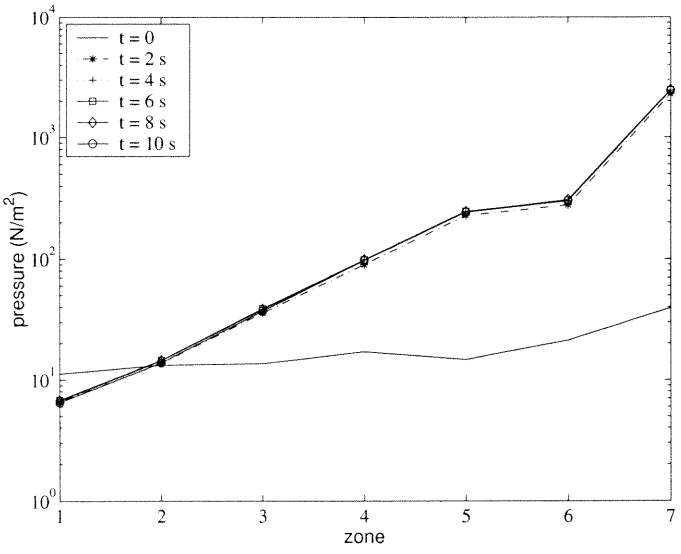

Figure 4.12 Pressure distribution inside the chamber for the system with scraper

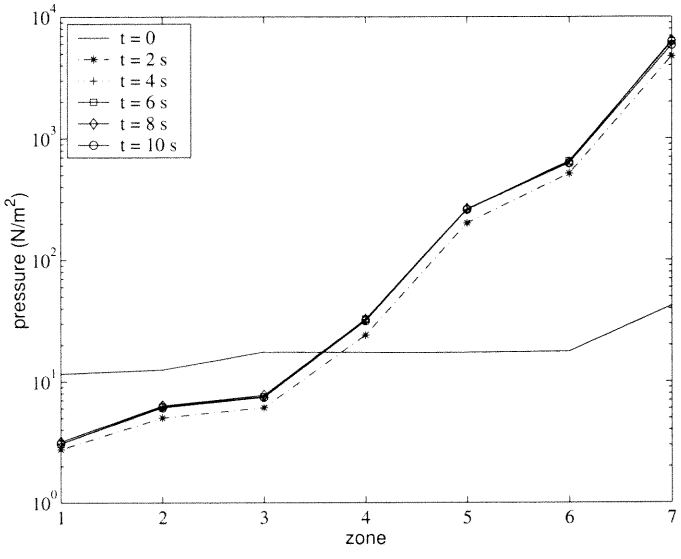

Figure 4.13 Pressure distribution inside the chamber for the system without scraper

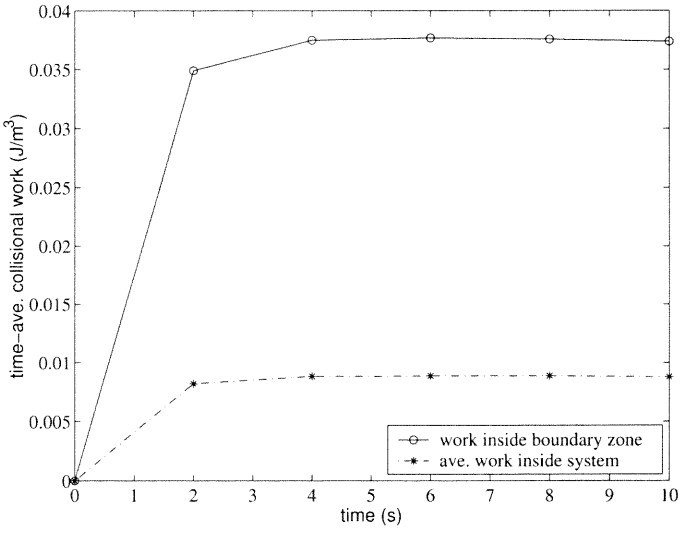

Figure 4.14 Time-averaged collision work for the system with scraper

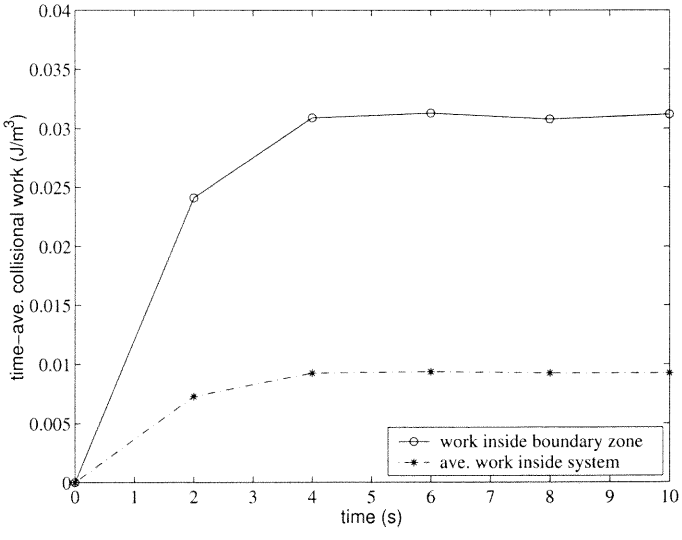

Figure 4.15 Time-averaged collision work for the system without scraper

4. Collision work. Finally, the collision work of particles within the system is computed. The time averaged collision work done by the inner-particle forces is the potential energy of the system. It is calculated by equation,

$$\mathbf{E}_p = \frac{1}{V} \sum_i \sum_j (F_{ij}(\alpha_{ij} - \alpha_{ij_0})) \tag{4.13}$$

Here V is the volume of cell, and α_{ij} is the relative displacement of particles i and j, and α_{ij_0} is the value of previous time step.

Figure 4.14 and Fig. 4.15 show the collision work inside the chamber as a function of time for the two kinds of systems (with scraper and without scraper), respectively. Generally, the collision work inside the boundary zone is much larger than the average work inside the system. Although the average collision work inside the system with time is similar inside the two systems, the collisional work because of interaction inside boundary zone is larger for the system with scraper.

4.4 Force Inside the System

The comparison study and diagnostic analysis of two Mechanofusion chambers show that the numerical simulation can show the essence of flow patterns and predict dynamics of the system . However, those are not the final objectives for this simulation study, since they don not provide an ability to do coating analysis.

It is obvious that for dry particle coating process, mechanism for the coating is resulted from particle-particle interactions and particle-system interactions. Here, force calculations are based on the following considerations: First, force on the inner piece as a function of the rotational speed of chamber and loading of system is calculated and compared with the experimental result available in the literature [11]. The average forces on the particles during the process are calculated and categorized into four areas. When not specified, the running conditions for the simulation are: loading 1500 particles, gap size 1.6 mm.

4.4.1 Force on the Inner Piece

The methodology of DEM makes it possible to keep tracking all the interactions of particles with the inner piece at any time instant. The normal force and tangential force are calculated respectively. They are long-termed average values and are obtained by averaging all the instant values during the simulation. The following

numerical studies are performed in order to compare the simulation results with that of experiment:

- Force on the inner piece as a function of the rotational speed of chamber, Fig. 4.16. The calculated normal force and tangential force on the inner piece linearly increase with rotational speed of chamber under log-log plot. Experimental study of polystyrene beads at the rotation speed shows a linear relationship for the normal force in the log-log plot and similar relationship for the tangential force.

- Normal force and tangential force on the inner piece as a function of loading of the system. For each loading, the simulation is running under three values of rotational speed of chamber. The results are shown in Fig. 4.17 and Fig. 4.18, respectively. Both normal force and tangential force on the inner piece increase with the load of the system. The increase rate is larger under higher rotation speed. The numerical result agrees with experiment results qualitatively.

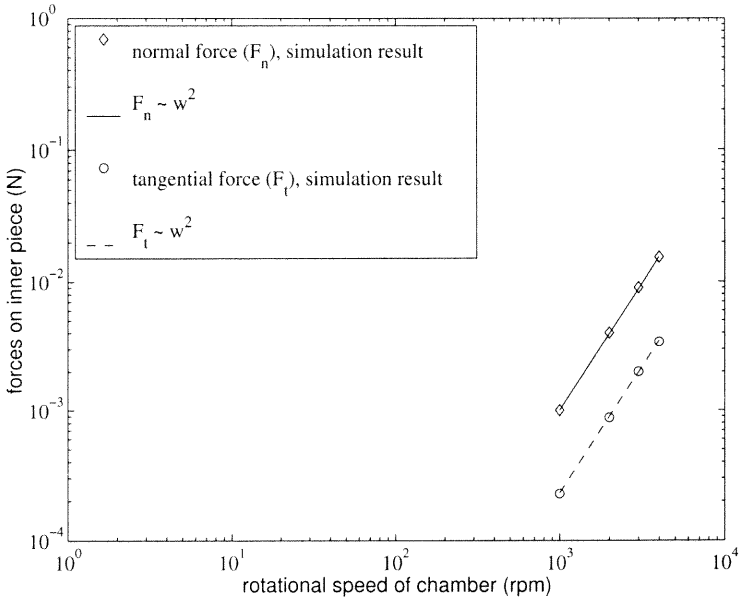

Figure 4.16 Average force on the inner piece as a function of the rotation speed

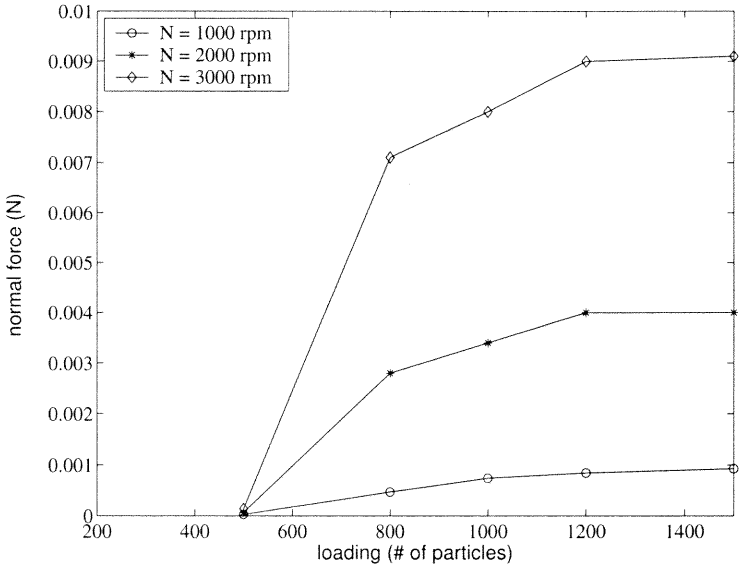

Figure 4.17 Normal force on the inner piece as a function of loading of particles and rotation speed

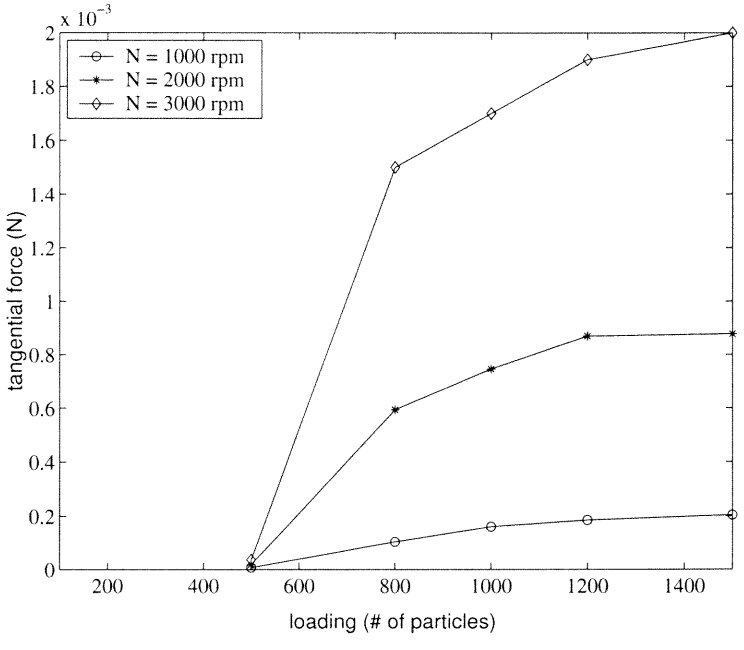

Figure 4.18 Tangential force on the inner piece as a function of loading of particles and rotation speed

4.4.2 Force on Particles Within the System

In a Mechanofusion system, particles are expected to experience different interactions inside the system. The calculation of force on the particles can show the internal difference within different regions inside the system. There are four areas defined inside the system, as shown in Fig. 6.4. Area 1 is defined as "inner piece area", which has converging-diverging shape. Area 2 is defined as "scraper area" since scraper function is put into this area. Area 3 is defined as "input area", because it is the place before the particles fall into the inner piece area. Area 4 is named as "free-diffusion" area, where the particles get freely dispersed after being scraped from the boundary.

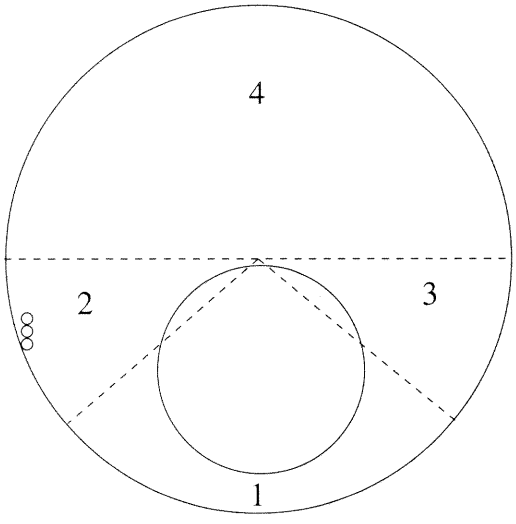

Figure 4.19 Area definition inside the system

The average normal force on a particle with time inside areas (Fig. 4.20), as well as the average tangential force on the particle inside area (Fig. 4.21), are calculated respectively. The values reported on these figures (Fig. 4.20, Fig. 4.21) are time-averaged values throughout a long period (in this case, it is 2s). The average forces on the particle inside the inner piece area and the scraper area are larger compared with values inside other two areas, which means that the particle experiences larger interaction forces inside those areas. These figures also show that under this situation,

average force on the particles inside the scraper area is largest within the system, because of normal impacts with the blade.

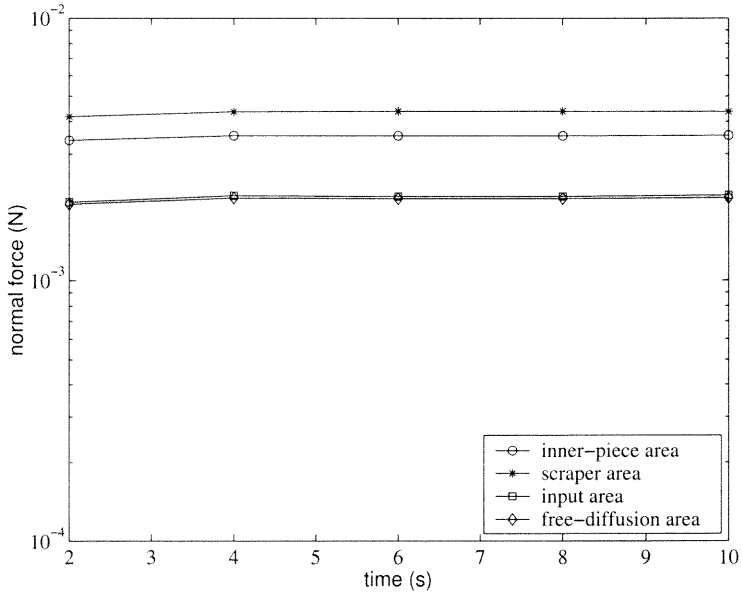

Figure 4.20 Average normal force on particles inside areas versus time

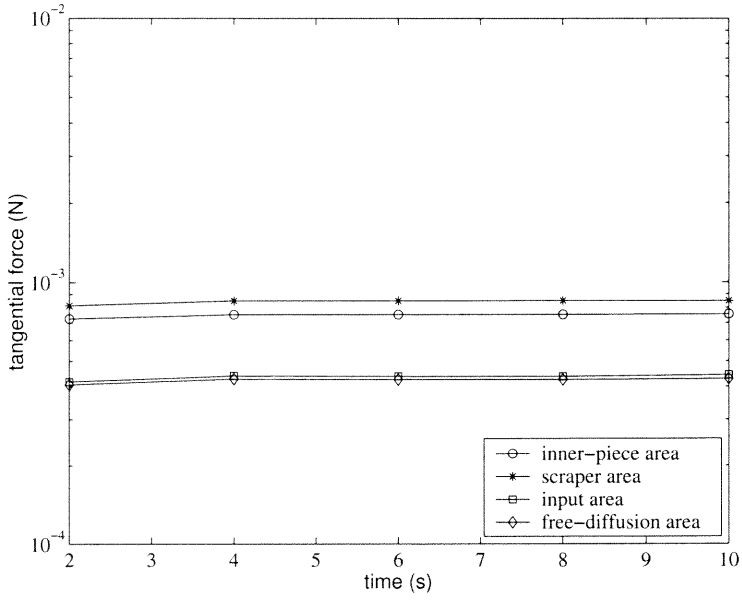

Figure 4.21 Average tangential force on particles inside areas versus time

4.5 Collision Analysis Inside the System

The calculation of average force on a particle during process shows theoretically the different stages that the particle experiences inside the Mechanofusion chamber. Purpose of the collision analysis inside the system is to understand the interaction frequency inside each area. Here, collision is categorized into the collision that happens between particles and the collision because of interaction of particles with the solid boundaries (cylinder boundaries and scraper fixed particles). The total number of collisions inside each area versus time are calculated first. System parameters for this analysis are same as above force analysis. Figure 4.22 shows the number of collisions of particles with boundary versus time and Fig. 4.23 shows the number of collisions between particles versus time inside different areas. The total collision number inside area increases with time. Collision ratio is calculated by equation,

$$\text{collision ratio} = \frac{\text{cumulative number of collisions inside area}}{\text{average number of particles within the area}} \tag{4.14}$$

Values inside each area are shown in Fig. 4.24 and Fig. 4.25, respectively.

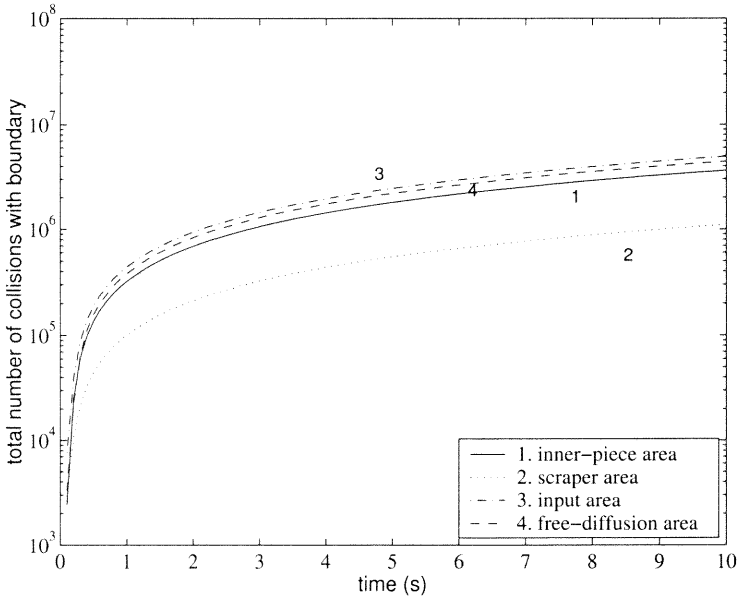

Figure 4.22 Collisions between particle and boundary inside areas versus time

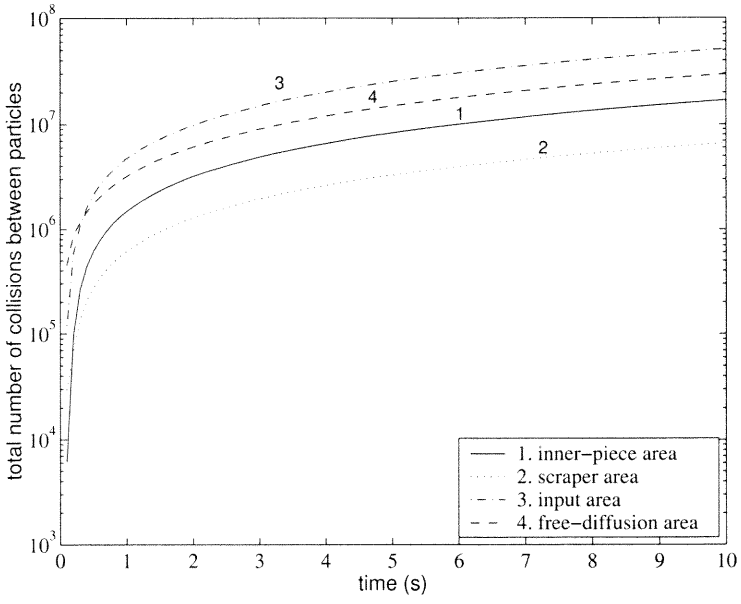

Figure 4.23 Collisions among particles inside areas versus time

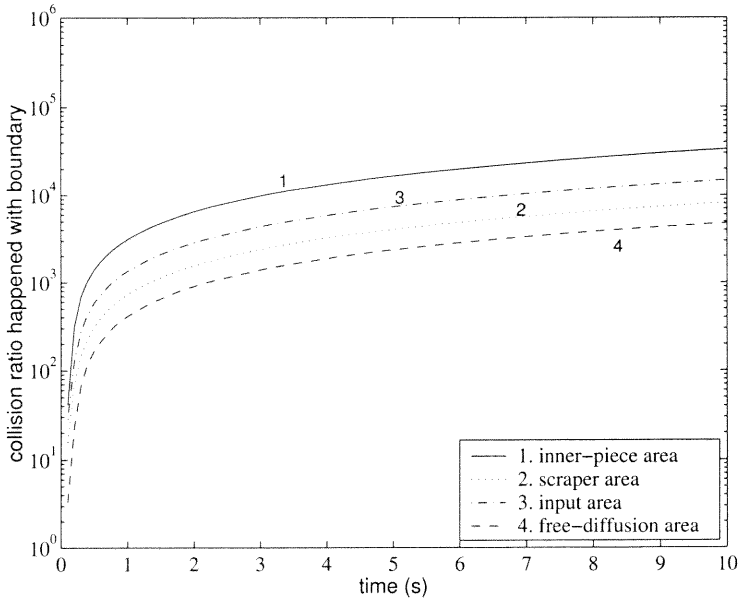

Figure 4.24 Collision ratio between particle and boundary inside areas versus time

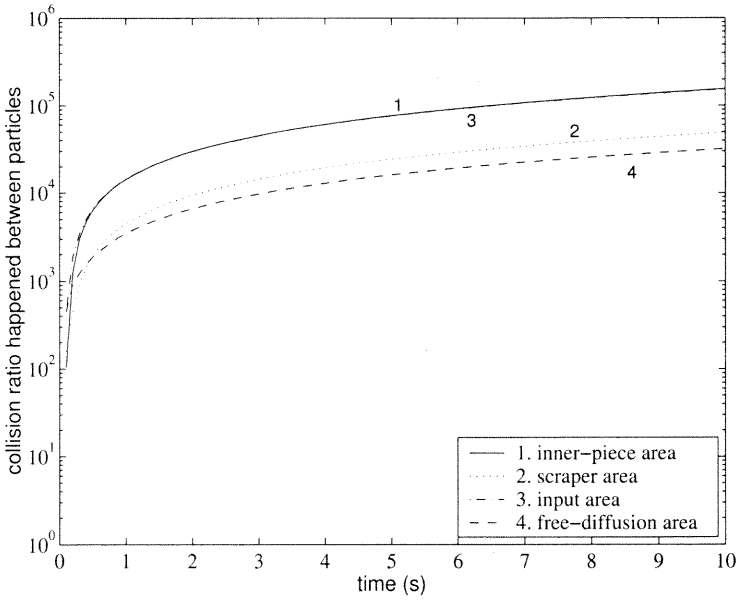

Figure 4.25 Collision ratio among particles inside areas versus time

Comparatively, the collision ratio inside free diffusion area is the smallest. This means particles inside this area have less chance to interact with each other, which is agreeing with the expectation. Collision ratio between particles inside the scraper area is smaller compared with the value inside the inner piece area and the input area. After being scraped up, particle seldomly interacts with each other. Collision ratio in the inner piece area and input area is larger, which means that the interaction inside those two areas is very active.

4.6 Deformation Analysis

Here deformation refers to embedding of guest particles to surface of host particles arose from particle-particle interactions and particle-boundary interactions. Although the system simulation does not include guest particles, the numerical results can still be used to predict deformations based on the performance of host particles, assuming that existing guest particles do not affect host-host interactions. The force result directly calculated from linear-spring model can not be used to represent the realistic contact force, however, it can reflect the relative interaction between

particles. Figure 4.26 shows the change of maximum force during a binary impact as a function of relative impact velocity and impact angle. The maximum contact force is linearly changed with relative impact velocity. The slope decreases while increasing impact angle. During the system simulation, the maximum force for each contact is calculated. Based on the binary impact analysis, the relative impact velocity of particles prior to contact can be deduced. Therefore, deformation study of a coating system is based on kinematics of host particles and is implemented by classical impact model.

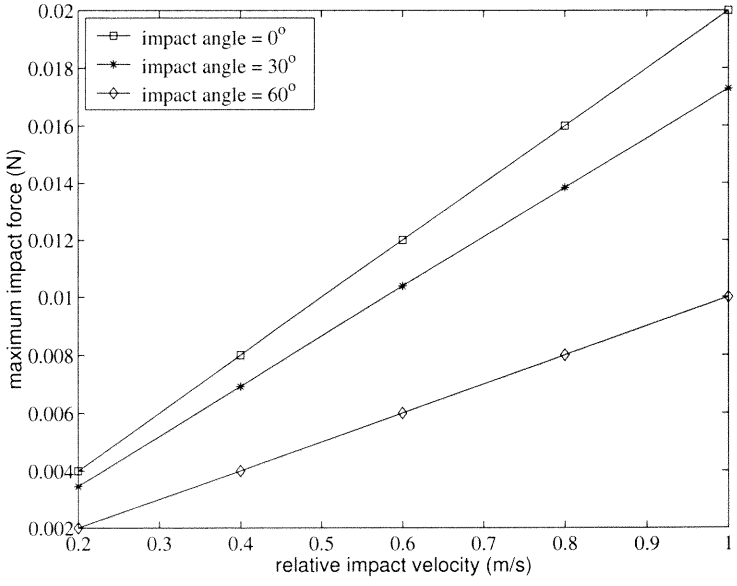

Figure 4.26 Maximum contact force as a function of relative impact velocity and impact angle of host particles

First, the maximum contact area because of host-host impact is calculated. The impact force is calculated and distributed onto guest particles falling inside the contact area which are assumed to have been evenly and loosely dispersed on the host surface. The force on each guest particle is therefore deduced and resulted central displacement of guest to host surface (here host particles are soft spheres and guest particles are rigid spheres) is obtained based on the classical impact theory. The detail calculation of this procedure can be found in Appendix B at the end of

dissertation. The deformation of coating system is expressed in the form of central displacement ratio, which is the rate of central displacement of a guest particle on a host surface to diameter of the guest particle. In this study, PMMA is used as host particles (400 μm) and Al_2O_3 (5 μm) is guest particle. Table 4.2 lists the properties of PMMA and Al_2O_3.

Table 4.2 Properties of PMMA and Al_2O_3

	PMMA	Al_2O_3
Density (ρ)	1190 Kg/m^3	3970 Kg/m^3
Young's modulus (E)	3300 MPa	345 GPa
Poisson's ratio (ν)	0.5	0.26
Dispersive surface energy (ω_d)	35.9 mJ/m^2	1000 mJ/m^2
Polar surface energy (ω_p)	4.3 mJ/m^2	540 mJ/m^2

1. Effect of the host-host interaction: The effect of relative impact velocity on contact area on the host surface is shown in Fig. 4.27, which illustrates that contact area linearly increases with velocity. Figure 4.28 is the deformation level as a function of relative impact velocity of host-host. It is shown that the relative interaction velocity does not affect the deformation level if it is beyond elastic yield limit, which means that coating product is not related with system operations.

2. Effect of particle parameters: Some important parameters such as size of guest particles and hardness of host particles to deformation level are studied. The corresponding results are listed in Fig. 4.29 and Fig. 4.30, respectively. Figure 4.29 shows that the smaller guest particle will come with larger deformation ratio and resulted in stronger surface interaction of a coating system. However, the change of deformation ratio is not significant comparing with size change. The hardness study is based on changing Young's modulus of the host particle. Figure 4.30 presents results for two hardness values for the host particle. Comparatively, the hardness of host particle has significant effect on

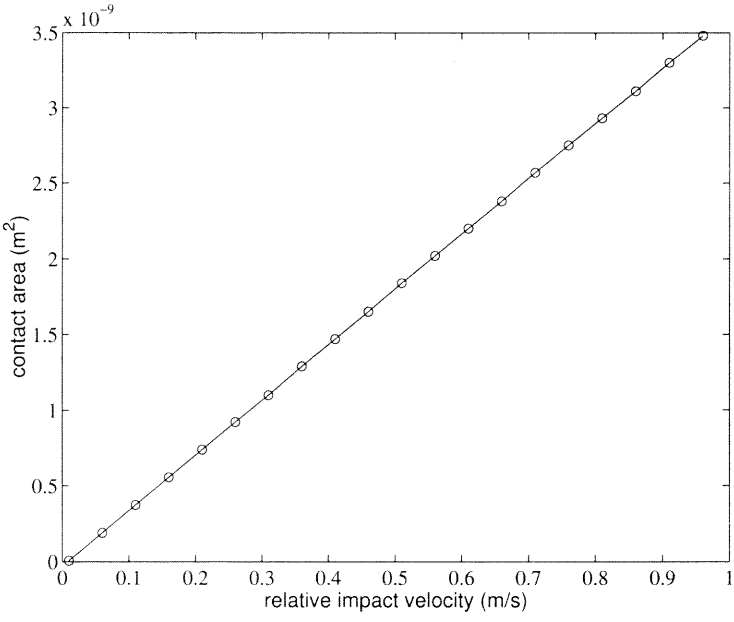

Figure 4.27 Contact area as a function of relative impact velocity of host particles

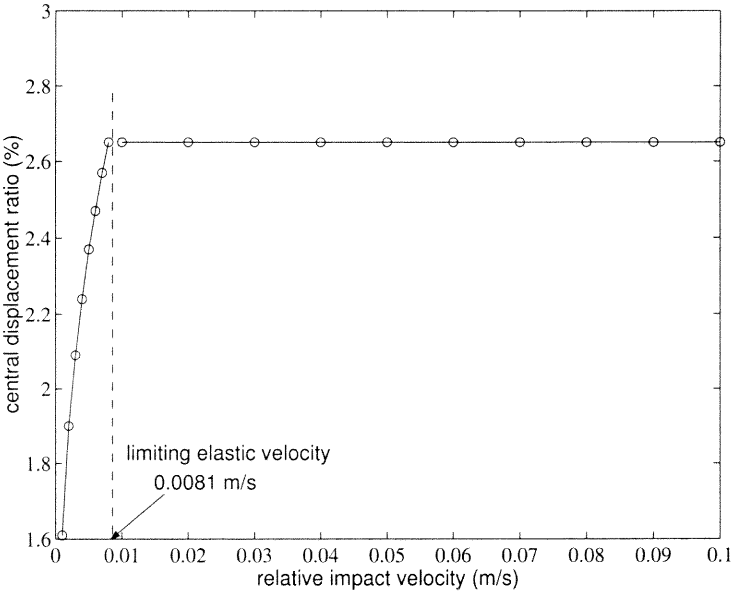

Figure 4.28 Central displacement ratio as a function of relative impact velocity

deformation level. The increased hardness of the host particle results in less deformation of a guest particle on the host surface. The similar observation of effect of hardness of particle and size ratio of host to guest particle on coating level has obtained by experimental study [13] [15].

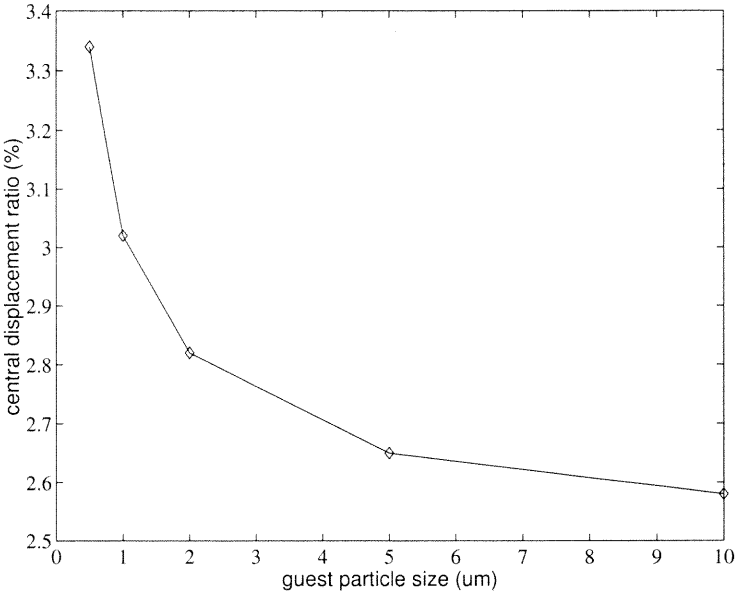

Figure 4.29 Central displacement ratio as a function of size of guest particles

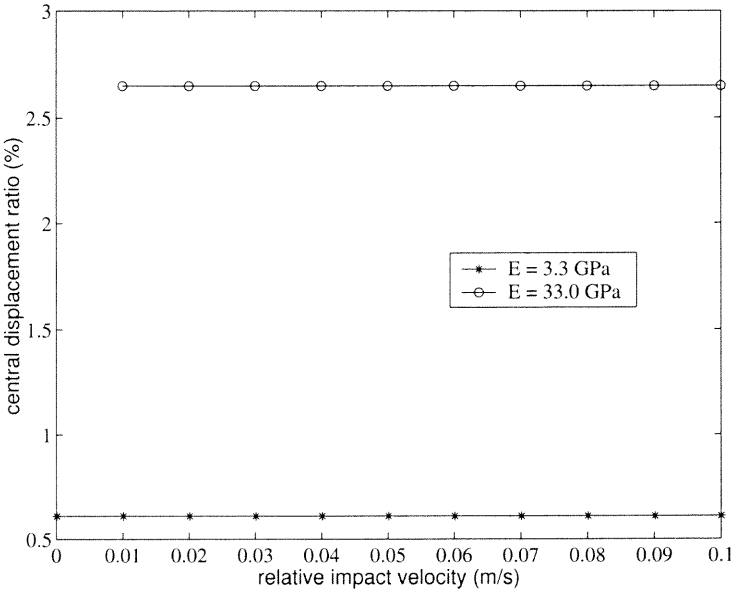

Figure 4.30 Central displacement ratio as a function of relative impact velocity and hardness of host particle

4.7 Coating Time Calculation

The minimum required coating time is based on the time required to have a complete coverage of surface area of all the host particles. This is estimated by the following steps (Fig. 4.31):

- Calculate the maximum central displacement d for each host-host contact.
- Calculate the contact radius a of this contact by the equation: $a = \sqrt{d * R}$
- Do the summation of contact area until it equal to the total surface area of the system, which is $N * S$, where N is total number of host particles and S is the surface area of each host particle and $S = 4\pi r_i^2$, and r_i is the radius of particle.

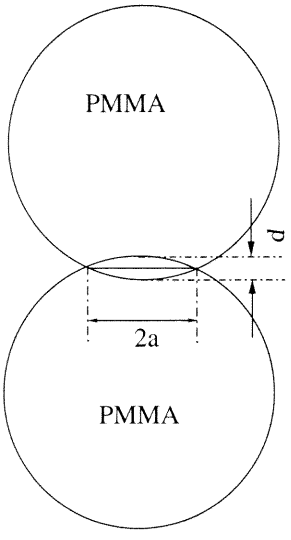

Figure 4.31 PMMA and PMMA

If number of particles inside the system is 1500, rotation speed is 2000 rpm and gap size is 1.6 mm, the minimum coating time needed is 0.61 seconds. This time is much less than the experimental study since here it is assumed that each contact occurs at a different position on particle surface. It is emphasized that the minimum time computed is only an estimated value and is only intended as an indicator for comparing different cases.

4.8 Effect of System Parameters on the Coating

Finally, the parameters that may affect the operation of the Mechanofusion device are examined. The change of average contact forces inside the system and required minimum coating time as a function of rotational speed of chamber and gap size is studied respectively. Force result from the direct system simulation can not put to deformation analysis as stated previously. However, as shown in Fig. 4.26 this value is linearly changed with relative velocity between particles before contact, which is closed related to the coating outcome. From this point, average contact forces inside areas are related with coating result. For each case of parametric study, there is only one parameter that is varied while the rest are kept constant.

4.8.1 Rotation Speed

A series of tests are carried out by changing the rotation speed while keeping loading of particles and gap size constant. Here, particle loading is 1500 and gap size is 1.6 mm. First, the effect of rotational speed of chamber on the average contact force, which affects the coating outcome, is studied. Figure 4.32 shows that average contact forces inside the system increase proportionally with the rotation speed. The rate of increase is different for different areas. Comparatively, inter-particle forces in scraper area have the largest increase rate while forces in free-diffusion area have the least increase rate. Figure 4.33 illustrates the effect of rotation speed on the minimum coating time. The figure shows that coating time is inversely proportional to the rotation speed. It is obvious that increasing rotation speed enhances interactions inside the system, while results in a reduction in the minimum coating time.

4.8.2 Gap size

The study of gap size on coating is performed under the following conditions: particle loading is 1500 and rotation speed is 2000 rpm. As seen from Fig. 4.34, average inter-particle force within the inner piece area is inversely proportional to the gap. The

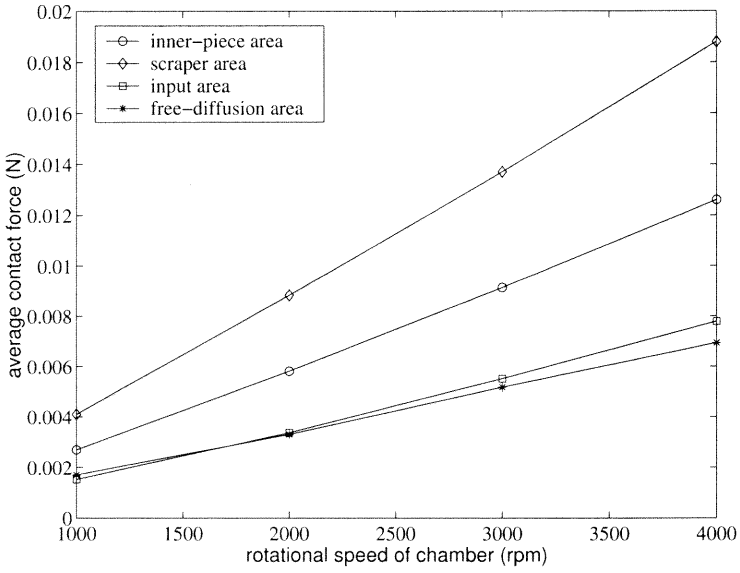

Figure 4.32 Average inter-particle force inside each area as a function of rotation speed (rpm)

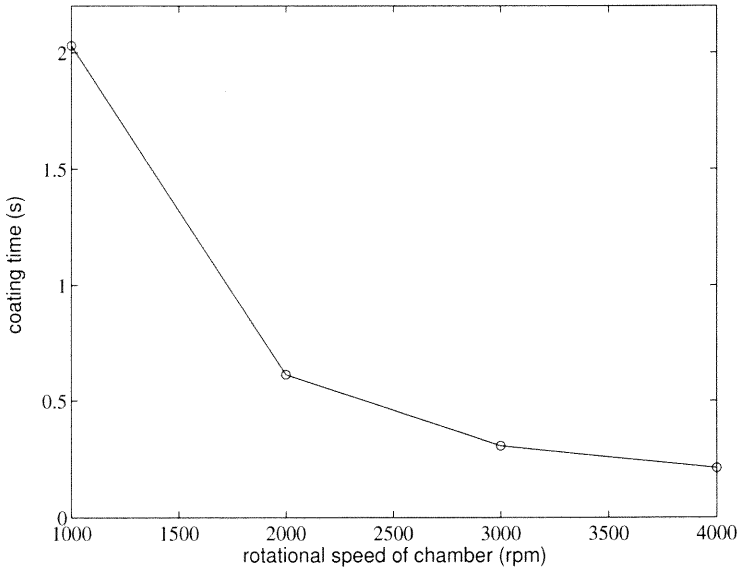

Figure 4.33 Coating time as a function of rotation speed (rpm)

reduced gap size increases the interaction inside this area, which agrees with the experimental study. However, the smaller gap size may constrict the particle flow inside the system. As shown in Fig. 4.34, the interaction inside input area and free-diffusion area get decreased with smaller gap size. Besides, small gap size requires longer coating time, as shown in Fig. 4.35.

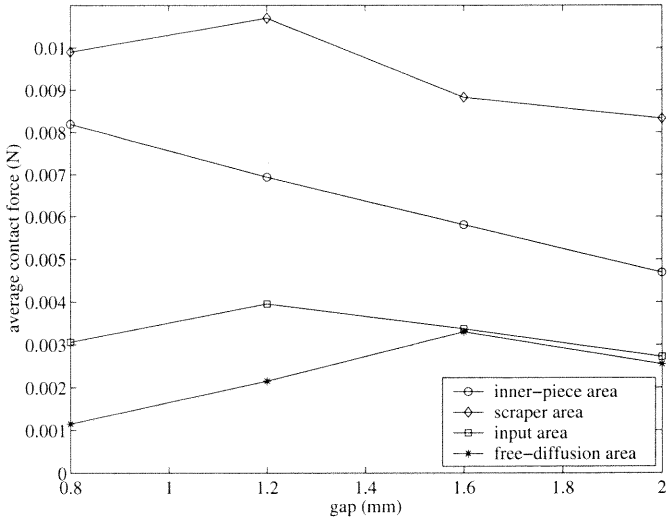

Figure 4.34 Average contact force inside each area as a function of gap size (mm)

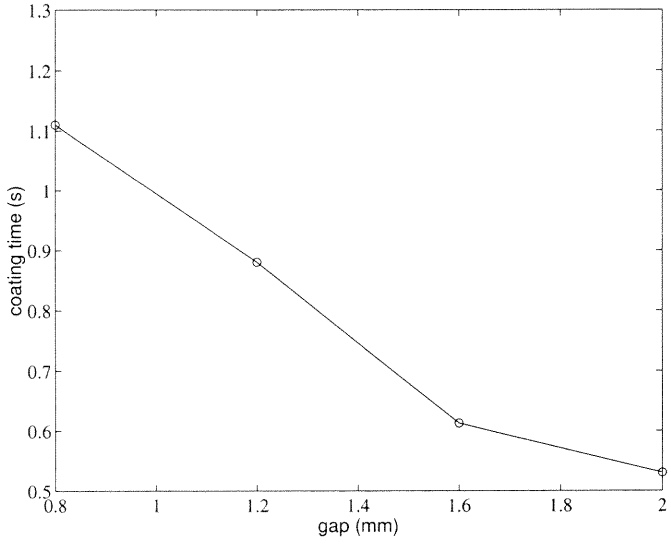

Figure 4.35 Coating time as a function of gap size (mm)

4.9 Conclusion

Numerical simulation of Mechanofusion system based on DEM technique is reported in this chapter. The simulation is performed on two-dimensional mode. The comparative agreement between three-dimensional simulation results (Appendix A) and two-dimensional simulation results verifies that the dimensional reduction is reasonable. The system-scale simulation is carried on a mono-dispersed system where only host particles are taken into consideration. The comparison study and diagnostic analysis of two Mechanofusion chambers with and without scraper clearly demonstrate the effect of scraper on the system. The numerical simulation are proved to be able to uncover the dynamics of the system. The calculation result of force on the inner piece illustrates that the normal force and tangential force are approximately proportional to square of rotational speed of chamber, which is qualitively comparable with that of the reported experimental result. Moreover, experimental observation of average force on the inner piece as a function of particle loading and rotation speed is also illustrated by the numerical study. Average forces on particles inside the system are calculated and categorized into four regions. The results show that a particle may experience different force inside the system during operation and comparatively, force on the particle inside the inner-piece area and the scraper area is two times as the value in the rest areas. Collisional analysis also shows that there are intense interactions inside the inner piece area and the scraper area. As can be seen from the results presented in this chapter and summarized above, DEM simulations can provide detailed information that was not available from fluid-based modeling [19]. It is noted that the fluid-based modeling only provided information on the force on the inner-piece as a function of the rotation speed.

Deformation analysis is based on the relative interactions between particles. The coating level which is expressed in the form of central displacement ratio of

guest particle to host surface is examined through a simple deformation analysis. The calculation result illustrates that coating level is not related to particle-particle interaction beyond the elastic yield limit, but related to the combination of a coating system (such as hardness of host particles and size of guest particles). The softer host particle and the smaller guest particle produce deeper coating under the same particle-particle interaction. The calculation result agrees with the experimental result. The parametric study shows that rotation speed and gap size may affect coating outcome. Increasing rotational speed will produce even coating with less coating time. The minimum coating time to cover whole surface of host particles is inversely proportional to gap size.

CHAPTER 5

DIMENSIONAL ANALYSIS OF MECHANOFUSION SYSTEM

5.1 Introduction

DEM is a very popular method in numerical studies of particulate systems. However, there is no literature about its application in Mechanofusion process. The present work of the numerical simulation of a Mechanofusion system based on the DEM technique provides useful information for the system operation. However, it should be pointed out that there are still some limitations of the current simulation model. First and most is the small system size that is adopted in the simulation. The size of the experimental apparatus is five times of the simulated system. Moreover, parameters such as particle size, particle properties, and gap size that are used in the numerical system may different with that in a real system. The effort here is try to evaluate the performance of the real system based on the results from the simulated system.

Research work done by Hopkins, et al for the study of rapidly deforming, steady, simple shear flows of inelastic disks of spheres developed a new Monte Carlo simulation method based on the theoretical framework of the kinetic theory of dense gases [40]. Recent theories for rapid deformations of granular materials have attempted to exploit the similarities between the grains of deforming granular mass and the molecules of a dis-equilibrated gas [77] $\sim$ [81]. For granular flows involving rapid deformations at much higher particle densities, the impulsive forces in collisions between pairs of neighboring particles are responsible for the transfer of momentum in the flowing material. If it is assumed that these collisions occur instantaneously between pairs of spheres, then these system of spherical grains are dynamically and statistically close to those considered in the ordinary non-equilibrium kinetic theory for dense gases [82]. Experiments involving the shear of both dense suspensions spherical particles and dry, dense masses of identical

spheres indicate that at sufficiently high rates of shear the dominant mechanism of momentum transfer is collisions between particles [83] [84]. Since the particulate flow within the Mechanofusion system is dominated by the continuous collisions between particles and between particles and system boundaries, furthermore, during a system simulation, particles are treated as elastic-plastic spheres, the dimensional analysis, which tried to scale up the simulated system, is therefore based on the fundamental of kinetic theory.

It should be pointed out that there is some difference between a classical dense gas and a rapidly deforming granular material. In the granular material an inhomogeneity of the mean flow is necessary to force the collisions and to drive the velocity fluctuations. Also, collisions between the particles of a granular material involve a loss of energy. Therefore, the implementation of kinetic theory for a rapidly deforming granular material should be different from that for a classical dense gas, as calculations much be extended in order to deliver the rate at which fluctuation energy is dissipated into heat [81].

5.2 Theory for a Simple Collisional Shear Flow

Based on the above considerations, Jenkins and Richman developed a kinetic theory for rapid deformations of identical, smooth, nearly elastic, spherical particles [85]. The constitutive quantity for the total pressure tensor, P_{ij}, inside a dense gas of inelastic spheres may be expressed compactly as

$$P_{ij} = (p - \omega D_{kk})\delta_{ij} - 2\mu \hat{D}_{ij} \tag{5.1}$$

where p is pressure, ω is bulk viscosity, μ is shear viscosity, D_{kk} is extension strain tensor (or normal strain tensor), and for a simple shear flow, $D_{kk} = 0$; δ_{ij} is known as the substitution tensor or the identity tensor, it is defined as

$$\delta_{ij} \equiv 1 \quad \text{if } i = j$$

$$\delta_{ij} \equiv 0 \quad \text{if } i \neq j$$

$\hat{D}_{ij}$ is the deviatoric part of the strain rate, $\hat{D}_{ij} \equiv \frac{1}{2}(u_{i,j} + u_{j,i})$.

Pressure p is defined by

$$p \equiv \nu\rho_s(1 + 2G(1 + e))T$$

ω is defined by the equation

$$\omega \equiv \frac{8m\nu G\ (1 + e)T^{\frac{1}{2}}}{\pi^{\frac{3}{2}}d^2}$$

Here m is mass of a particle, d is diameter of the particle, e is coefficient of restitution, T is granular temperature, and ν is solid volume fraction, and is defined as

$$\nu \equiv n\pi d^3/6$$

In the above, n is number density, $n = \frac{N_{total}}{V}$, N_{total} is number of particles inside the system and V is volume of the system. G is a function of ν

$$\begin{cases} G & = \nu g_o(\nu) \\ g_o(\nu) & = \frac{1}{1-\nu} + \frac{3\nu}{2(1-\nu)^2} + \frac{\nu^2}{2(1-\nu)^3} \\ & = \frac{\nu(2-\nu)}{2(1-\nu)^3} \end{cases}$$

and μ is defined by

$$\mu \equiv \bar{\mu}(1 + \frac{4}{5}G(1 + e)) + \frac{3}{5}\omega$$

Here $\bar{\mu}$ is the transport shear viscosity, and can be defined by

$$\bar{\mu} \equiv \alpha(1 + \frac{2}{5}\nu(3e - 1)(1 + e))$$

where

$$2\alpha \equiv \frac{5mT^{\frac{1}{2}}}{2d^2g_o(1 + e)(3 - e)\pi^{\frac{1}{2}}}$$

If Eq. 5.1 is applied to a simple shear flow (incompressible), shown in Fig. 5.1, which has the velocity field,

$$\begin{cases} \bar{u} = (u, 0, 0) \\ \frac{\partial}{\partial x} = \frac{\partial}{\partial z} = 0 \end{cases}$$

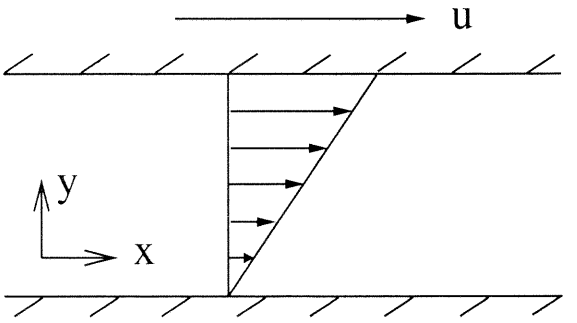

Figure 5.1 A simple shear flow

The equations for normal and shear stress can be expressed as:

$$\begin{cases} \sigma_{yy} = \nu\rho_s(1+2G(1+e))T \\ \sigma_{xy} = \mu\frac{\partial u}{\partial y} \end{cases} \tag{5.2}$$

Since an analysis of simple shear flow shows that the approximations made in determining the form of the single particle velocity distribution function are valid only when the particles are nearly elastic, so here it can further more assumed that $e \approx 1$. Equation 5.2 can be simplified as

$$\begin{cases} \sigma_{yy} = \nu\rho_s(1+4G)T \\ \sigma_{xy} = \frac{8J}{5\sqrt{\pi}}\nu G d\rho_s T^{\frac{1}{2}}\frac{\partial u}{\partial y} \end{cases} \tag{5.3}$$

where

$$J = 1 + \frac{\pi}{12}(1+\frac{5}{8G})^2$$

The equation for T in the simple shear flow is introduced next. It is known that the dominant terms in the governing equation of T are:

a. Shear production $= \sigma_{xy}\frac{\partial u}{\partial y} = \frac{8J}{5\sqrt{\pi}}\nu G d\rho_s T^{\frac{1}{2}}(\frac{\partial u}{\partial y})^2$

b. Inelastic dissipation $= \frac{24}{\sqrt{\pi}}(1-e)\frac{\rho_s T^{\frac{3}{2}}}{d}\nu G$

In the simple shear flow, those two terms are balanced, therefore it can be deduced that:

$$T^{\frac{1}{2}} = \sqrt{\frac{J}{15(1-e)}}d\frac{\partial u}{\partial y} \tag{5.4}$$

Substitute Eq. 5.4 into Eq. 5.3, it is easy to get new equations of stress for this flow, as:

$$\begin{cases} \sigma_{yy} = \frac{\nu(1+4G)J}{15(1-e)}\rho_s d^2(\frac{\partial u}{\partial y})^2 \propto (\frac{\partial u}{\partial y})^2 \\ \sigma_{xy} = \frac{8J}{5}(\sqrt{\frac{J}{15(1-e)}})\nu G d^2 \rho_s (\frac{\partial u}{\partial y})^2 \propto (\frac{\partial u}{\partial y})^2 \end{cases} \tag{5.5}$$

Therefore, if the flow is indeed collisional, the stress will change with the square of the shear rate, provided that other parameters are kept the same. Actually, as early as 1954, Bagnold considered the collisions between particles of a rapidly sheared granular material consisting of identical spherical grains [83]. Bagnold argued that, because both the momentum exchanged in a collision and the frequency of collisions are proportional to the mean rate of shear, the shear stress and the normal stress must both be proportional to the square of the mean shear rate. The normal stress and shear stress measured in Bagnold's own experiments and the more recent experiments of Savage & Sayed on simple shear flows do depend on the mean rate of shear in this way [84].

Inside the inner-piece area, if the shear rate can be simply expressed as:

$$\frac{\partial u}{\partial y} = \frac{\omega R}{H} \tag{5.6}$$

which means the shear rate changes linearly with ω inside this area, where ω is rotational speed of a chamber, R is the radius of the chamber, and H is the size of gap. So if the flow is assumed to be a collisional flow in MF, the force on the inner-piece should change with rotational speed of chamber as:

$$\begin{aligned} F_n &\propto \omega^2 \\ F_t &\propto \omega^2 \end{aligned}$$

where F_n is normal force and F_t is tangential force.

Figure 5.2 is the experimental result of normal and tangential force acting on an inner piece as a function of the rotational speed of the chamber reported by

Yokoyama, etc. [11]. It displays a linear increase of forces with rotation speed of the chamber in a log-log plot. Figure 5.3 is a simulation result which implies that forces on the inner piece is an approximate function of ω^2, which basically agrees with the linear relationship between the forces and the rotational speed on the log-log plot shown in Fig. 5.2. Hence the simulation result and the experimental result qualitively match with each other. Therefore, it is reasonable to estimate forces on the individual particle based on the collisional flow assumption .

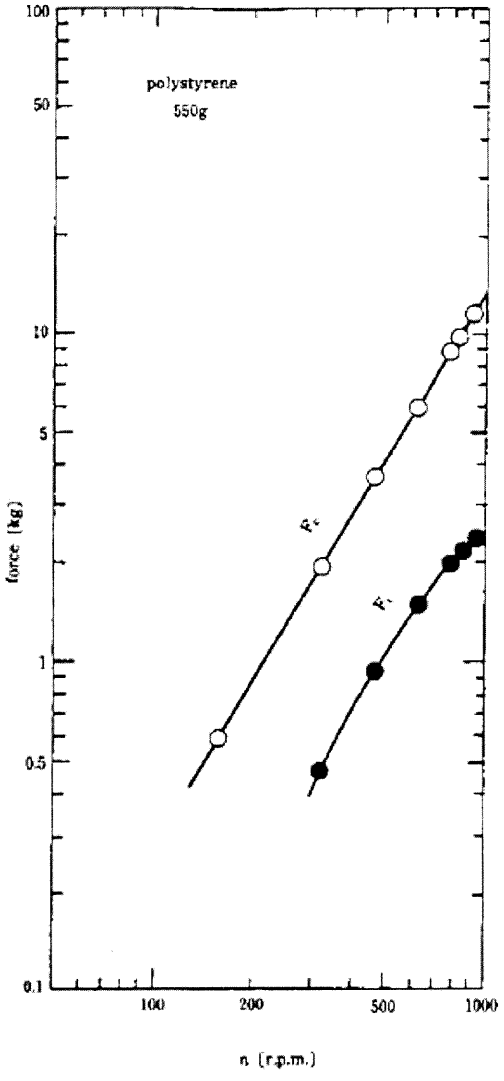

Figure 5.2 Variation of normal and tangential forces acting on the inner piece with rotation speed (Yokoyama, etc. [11])

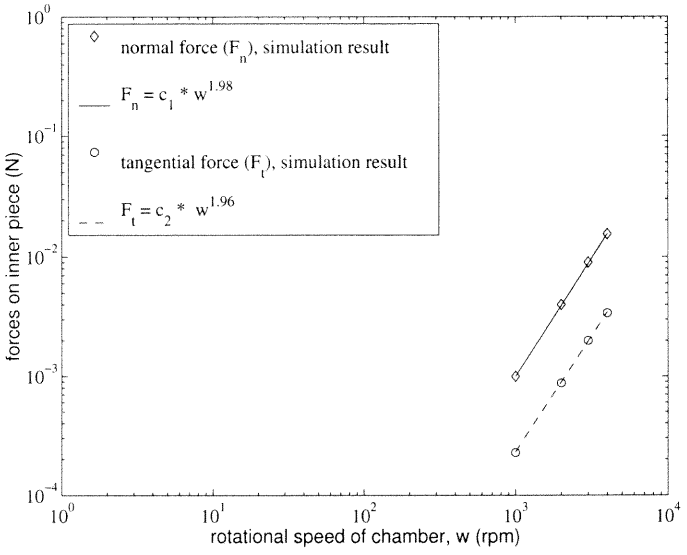

Figure 5.3 Comparison of the theoretical result with the simulation result of forces on the inner piece as a function of rotation speed

5.3 Similarity Relationship for MF System

It was shown in the previous section that a flow in a Mechanofusion system may be treated as a collisional flow. Therefore, kinetic theory can be employed in this similarity analysis. A similarity equation is deduced, which correlates the average force on a particle in a simulated system with that in a real system, where the size of systems, size of processed particle as well as operation parameters will be different.

5.3.1 Deduction of Similarity Equation

The average force acting on a particle during a collision is

$$\bar{F} = \frac{m \cdot \Delta v}{\Delta t} \tag{5.7}$$

where $\bar{F}$ is the average force the particle experiences in a collision, Δv is the change of velocity during a collision, m is mass of the particle, and $m = \rho_s \frac{\pi}{6} d^3$; Δt is contact time of two particles in a collision. According to Eq. 4.1,

$$\Delta t \propto \sqrt{\frac{m}{K}} \tag{5.8}$$

where K is spring stiffness in DEM model. Besides, in the collisional flow,

$$\Delta v \propto T^{\frac{1}{2}} \tag{5.9}$$

The particle may experience larger forces when it passes through the small gap between the inner-piece and the chamber wall, where the shear rate can be estimated by Eq. 5.6. After substituting Eq. 5.4, Eq. 5.8 and Eq. 5.9 into Eq. 5.7, Eq. 5.7 can be rewritten as

$$\begin{aligned} \bar{F} &\approx \frac{m}{\Delta t} T^{\frac{1}{2}} \approx \frac{m}{\Delta t} \cdot d\frac{\partial u}{\partial y} \\ &\approx \frac{d}{H}\omega R\sqrt{mK} \end{aligned} \tag{5.10}$$

Therefore, similarity relation, which can be used to estimate the force on the particle in a real system based on the result from a simulated system, is expressed as:

$$\frac{\bar{F}_s}{\bar{F}_r} = \frac{\frac{d_s}{H_s}\omega_s R_s\sqrt{m_s K_s}}{\frac{d_r}{H_r}\omega_r R_r\sqrt{m_r K_r}} \tag{5.11}$$

where subscript s represents parameters for the simulation system and r represents parameters for the real system.

5.3.2 Comparison of the Theoretical Result With the Numerical Result for Two Geometrical Similarity Systems

The force on a particle during a simulation is compared for two systems: one is the original system that is used in the numerical study, another is a system which size is two times as that of the original system (here it is called double-sized system). Two systems have the similar geometrical model, with corresponding dimensions (including gap size) of the double-sized system are two times as that of the original system. The loading for the double-sized system is four times as that for the original system to make two systems have similar particle packing ratio. The similarity equation (Eq. 5.11) shows that if two systems are loaded with particles with same properties (m and K), and are operated under the same rotation speed of chamber, particles inside those two systems should experience same force conditions. Figure 5.4 $\sim$ Fig. 5.7 are average forces on particles inside areas for two systems under the

following operation conditions: rotation speed is 2000 rpm, gap size is 1.6 mm for smaller system and 3.2 mm for double-sized system, and simulation time is 1 second. Average forces on particles inside the inner-piece area and the scraper area have the similar value for two systems. However, average forces on particles inside the input area and the free-diffusion area for the double-sized system is not agreeing well with the value for the original system. It is reasonable, since a particle flow inside the free-diffusion area and the input area may not abide to the collisional flow assumption while increasing the size of the system. Based on a system-scale simulation, the system performance can be evaluated based on particle-particle interactions inside the inner-piece area where particles experience the larger forces and intense interactions with other particles and boundaries. The same coating product can be obtained from two geometrically similar systems under the same operation conditions. In addition, good agreement on kinetic modeling and numerical simulation was also obtained for two similar systems, both in geometry and particle size.

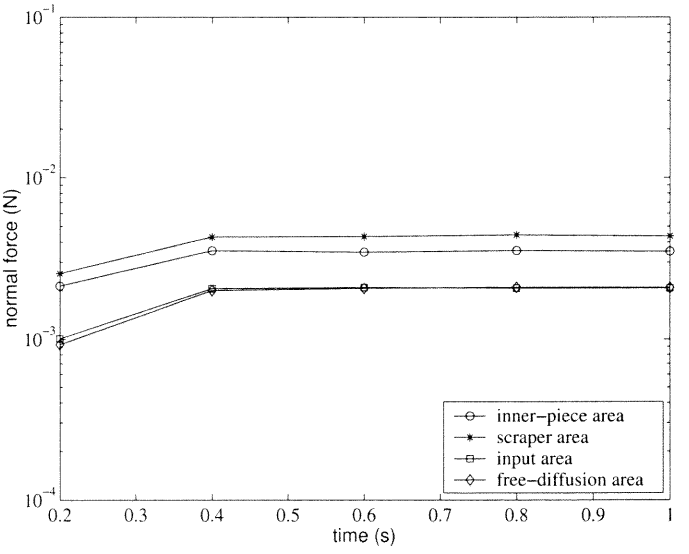

Figure 5.4 Average normal force on particles inside areas of the original system

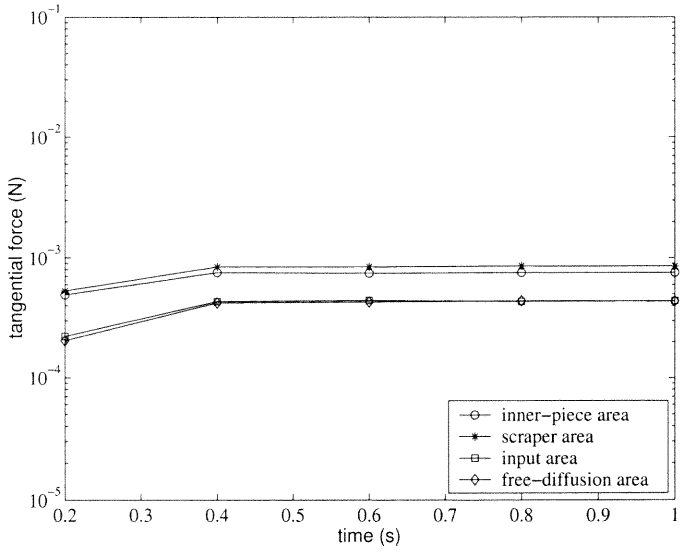

Figure 5.5 Average tangential force on particles inside areas of original system

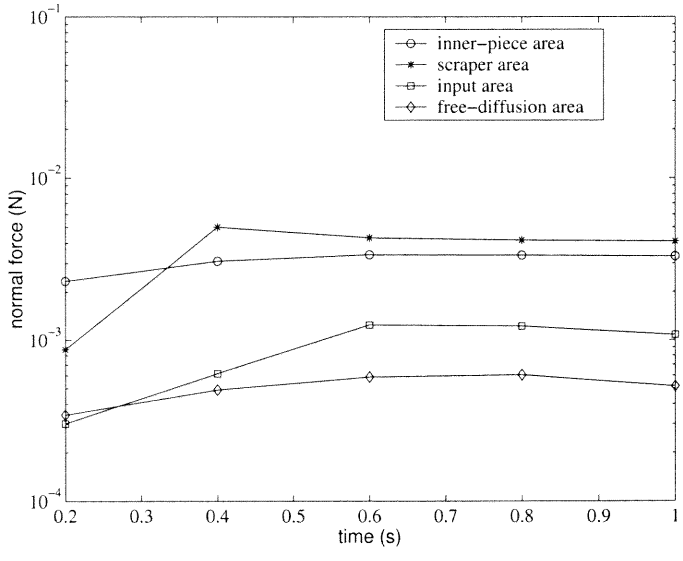

Figure 5.6 Average normal force on particles inside areas of double-sized system

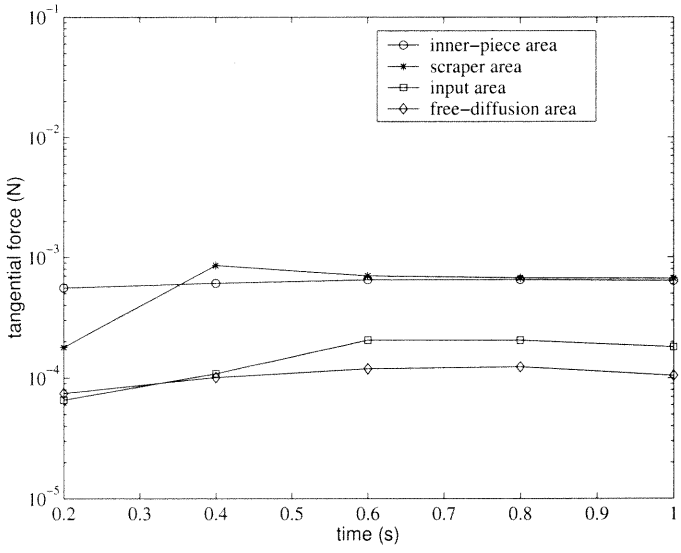

Figure 5.7 Average tangential force on particles inside areas of double-sized system

5.4 Selection of Spring Stiffness K

5.4.1 Constraints

As shown in Eq. 5.8, larger K means the smaller time step in a simulation. It is beneficial to be able to use smaller K if it doesn't change features of the flow inside a system. However there should be some constraints on using smaller K in the simulation study. In general, it is a question of relative magnitude of time scales. There are at least two constraints:

(i). Time for a particle to travel through the gap size, τ_f, is much larger than the contacting time in a collision τ_c, and $\tau_c = 2\sqrt{\frac{m}{K}}$. Inside a Mechanofusion system, τ_f can be roughly estimated by equation: $\tau_f \approx \frac{H}{\omega R}$. If $\tau_f \gg \tau_c$, then,

$$K \gg m(\frac{2\omega R}{H})^2 \tag{5.12}$$

(ii). Time for a particle to travel between two successive collisions, τ_t, is much larger than τ_c. From kinetic theory,

$$\tau_t = \frac{d}{\frac{24G}{\sqrt{\pi}}\sqrt{T}} \tag{5.13}$$

Substitute Eq. 5.4 and Eq. 5.6 into Eq. 5.13,

$$\tau_t = \frac{1}{\frac{24G}{\sqrt{\pi}}\sqrt{\frac{J}{15(1-e)}}\frac{\omega R}{H}} \tag{5.14}$$

If $\tau_t \gg \tau_c$,

$$K^{\frac{1}{2}} \gg 48G\sqrt{\frac{mJ}{15(1-e)\pi}}\frac{\omega R}{H}$$

and

$$K \gg 50\frac{JG^2}{1-e}(\frac{R}{H})^2 m\omega^2 \tag{5.15}$$

Finally, the value of K should satisfy the requirement of DEM model, which is based on the elastic-plastic assumption, that is during the simulation, the maximum deformation of a particle should be less than 1%. So there are three conditions to be considered when selecting K.

5.4.2 A Case Study

The stiffness value used in the simulation is selected based on impact mechanics and requirement that the maximum deformation of particle should be less than 1%. The value used in the simulation is 20000 N/m. It should be examined to see if this value can satisfy the constraints that listed above. According to the parameters that are shown in Table 5.1, this can be calculated.

parameter	equation	value
volume fraction ν	$n\frac{\pi}{6}d^3$	0.3048
G	$\frac{\nu(2-\nu)}{2(1-\nu)^3}$	0.7687
J	$(1+\frac{\pi}{12})(1+\frac{5}{8G})^2$	1.8606

Table 5.1 Parameters for the simulation system

1. According to the requirement of time period for a particle traveling inside the system, Eq. 5.12,

$$K \gg (\frac{2R}{H})^2 \omega^2 m$$

For the extreme case, $H = 1.6$ mm and $\omega = 419\ (1/s)$, for 4000 r.p.m., $K \gg 1.7$.

2. According to the requirement of comparative longer time for successive collisions, minimum K should satisfy Eq. 5.15,

$$K \gg 50 \frac{JG^2}{1-e} (\frac{R}{H})^2 m\omega^2 = 157.8$$

So the stiffness value that is adopted in the simulation satisfies the time constraints. Moreover, during the simulation, it is observed that maximum deformation is less than 1%, which satisfies the model requirement.

5.5 Parametric Analysis

1. Contact force as a function of stiffness: The momentum equation for a particle during a collision can be written as:

$$\bar{F} \Delta t = m \cdot \Delta \bar{v} \tag{5.16}$$

where $\bar{F}$ is average contact force on the particle during the collision and $\bar{v}$ is change of velocity during the collision. As it is known that $\Delta t \propto K^{-\frac{1}{2}}$, it can be deduced that $\bar{F} \propto K^{\frac{1}{2}}$. Figure 5.8 shows the relationship of average contact force as a function of normal stiffness based on a binary impact analysis. The simulation result of force $\bar{F}$ as a function of K exactly matches with the theoretical relation.

Figure 5.9 is the simulation result of average inter-particle force on particles inside the inner-piece area as a function of normal stiffness, and Fig. 5.10 is

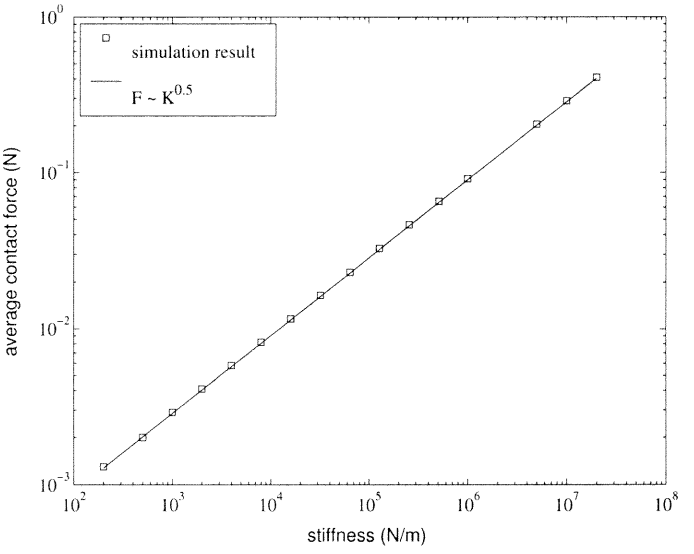

Figure 5.8 Average contact force on a particle during a binary contact as a function of stiffness

the result within rest of the areas. The relations of average forces with stiffness approximately match with the theoretical expectation. Hence it is possible to deduce force and stiffness relationship based on the numerical simulation.

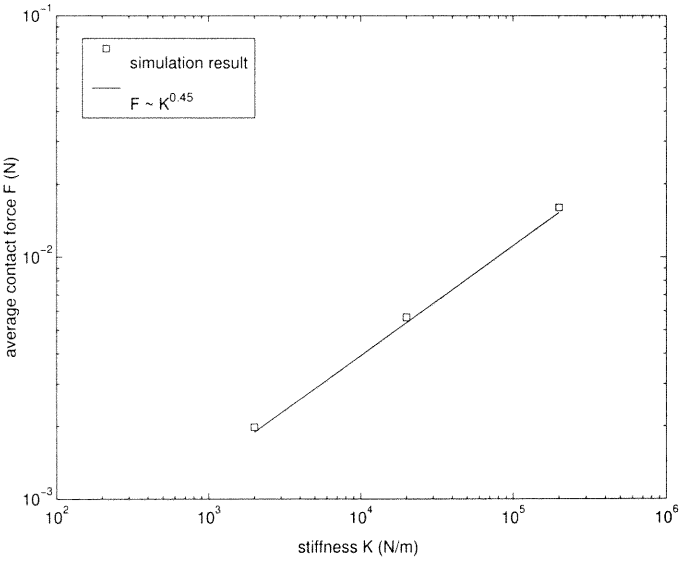

Figure 5.9 The numerical result of average force on particles inside the inner-piece area as a function of stiffness

2. Contact force as a function of rotation speed: According to the similar relationship (show in Eq. 5.11), average force on the particles inside the inner-

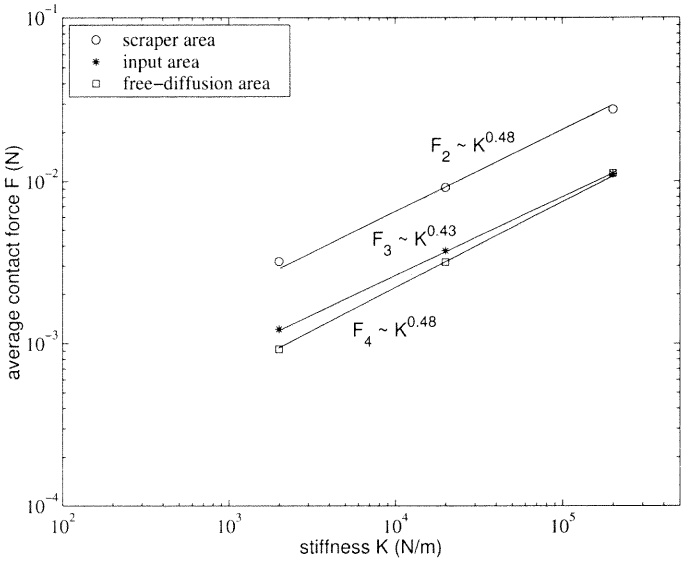

Figure 5.10 The numerical result of average force on particles inside the system as a function of stiffness

piece area should change linearly with the rotational speed of the chamber. The numerical simulation result, which is shown in Fig. 5.11, gives a similar relationship. Average inter-particle forces inside rest areas of the system are also proportional to the rotation speed, which is illustrated in Fig. 5.12.

3. Contact force as a function of gap size: The similarity relation, shown in Eq. 5.11, shows that average force on the particles inside the inner-piece area should be inversely proportional to gap. A simulation result, which is shown in Fig. 5.13, gives a similar trend but different function. Since the deduction of average force on particles as a function of gap-size is only valid for the inner-piece zone, it is difficult to find relations of force with gap-size for rest of areas of the system, which is shown in Fig. 4.34.

5.6 Conclusion

The limitation of DEM technique makes it difficult to handle simulation with the real system scale and particles. The results from a experimental study and a numerical

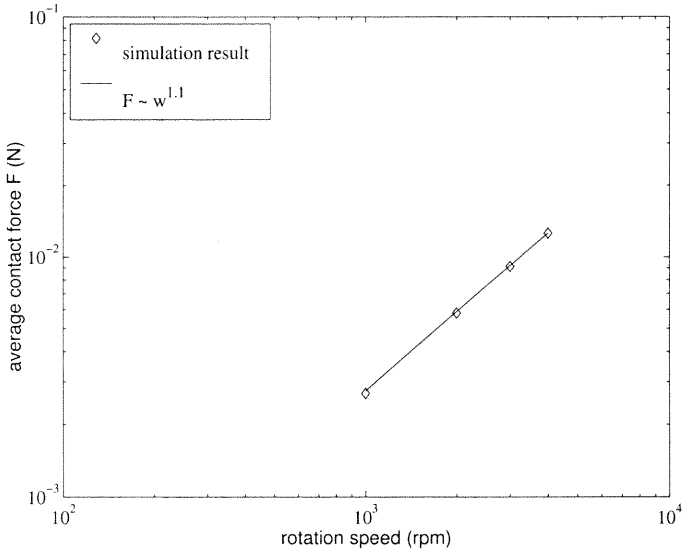

Figure 5.11 The numerical result of average force on particles inside the inner-piece area as a function of rotation speed

calculation of a Mechanofusion system show that the particulate flow inside the system can be treated as a simply collisional flow. Therefore, in this chapter, the dimensional analysis of the Mechanofusion system is carried out based on the fundamental of kinetic theory.

The derived equation for the average force on a particle inside the system establishes a correlation between a simulated system and a real system. Numerical results of forces on particles inside two geometry similar systems basically agrees with theoretical expectation. Major kinetic theory modeling based similarity results, verified by simulations and in part from available experimental data, include: (1) The calculate average force on a particle during a collision is related with the value of selected normal stiffness, and it is proportional to the square-root of the stiffness for a binary contact. The numerical result of force on the particles inside the system as a function of stiffness obtains the similar relation; (2) Inter-particle forces vary linearly with the rotation speed; (3) Force exerted on the particles within the inner-piece is inversely proportional to the gap-size, and (4) Force on the inner-piece varies linearly with the square of the rotation speed.

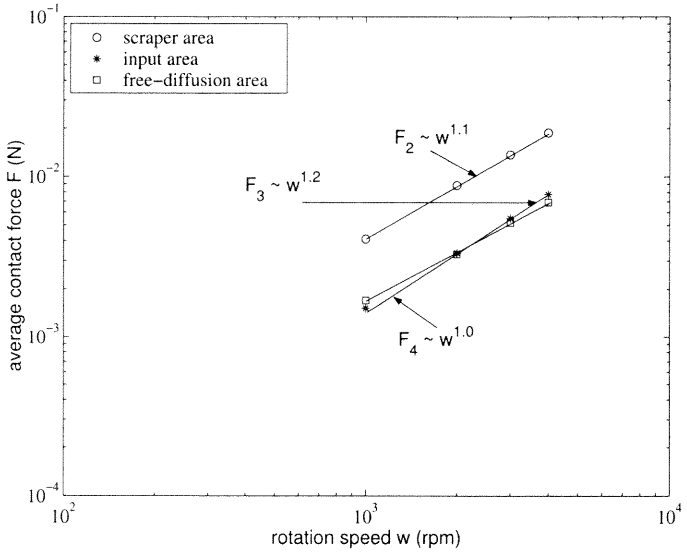

Figure 5.12 The numerical result of average force on particles inside the system as a function of rotation speed

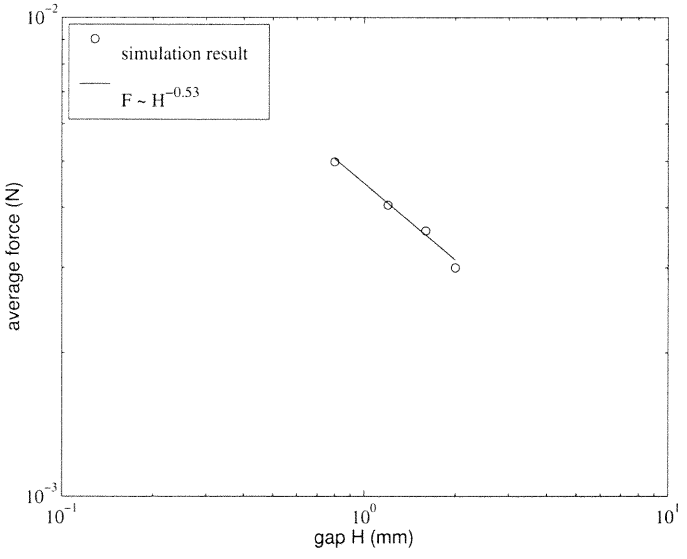

Figure 5.13 The numerical result of average force on particles inside the inner-piece area as a function of gap size

CHAPTER 6

CONTACT MODEL WITH ADHESION

6.1 Adhesion Model Review

Surface forces, which arise directly from molecular interactions, are usually classified as short-range and long-range forces. The short-range forces are often called chemical bonds and consist of metallic, covalent, ionic bonds and hydrogen bonds. Long-range attractive interactions are weak compared to short-range ones and result from van der Waals and electrostatic forces. Under normal ambient conditions, the short-range force is not important. In long-range intermolecular interaction, the dispersion component is also called the London-van der Waals dispersion force, which is an attractive force.

Adhesion is defined as the state in which two surfaces are held together by interfacial forces. Normally, it is considered to be van der Waals force that causes this interaction. The current theoretical model for the adhesive force of small particles dates back around 70 years. Bradley and Hamaker developed the theory by integrating the molecular attractive over the volumes of the neighboring spheres. The attractive potential between two spheres can be expressed as $E = -Ad/12z$, where A is Hamaker constant, d represents $\frac{d_1 d_2}{d_1+d_2}$, where d_1 and d_2 are the diameters of the two spheres, and z is the separation between the spheres. For adhering spheres, z is typically $4\mathring{A}$. Dahneke proposed a new theory that describes the interaction between two bodies as the sum of an attractive component and a repulsive component, obtained from an expression from the continuum theory of elasticity [86]. Since repulsion is included, the theory properly describes the influence of elastic flattening on the adhesion of spheres and also the minimal nature of the interaction force and energy. Based on the energy conservation principle and force balance, Tsai, et al deduced the analytical equations that describe the relationship between the elastic flattening and van der Waals adhesion force [87].

6.2 Contact Model Review

The classical solution of the contact problem of two non-adhesive spheres was given by Hertz in 1881. He studied two perfectly elastic spheres under a normal interaction (no friction). The resulted contact area and stress distribution are computed under a given compressive load. In Hertz model, there is no attraction or stickiness, elastic spheres would separate freely at zero or negative load.

Johnson, Kendall and Roberts (referred to as JKR [88]) extended the Hertz theory to include the adhesion effect. In their model, two solids would stick together when in contact, due to possessing a finite surface energy. Under a given load, the contact area computed by JKR model is larger than the value given by Hertz model. Apart from a compressive stress near the center, there is a tensile stress near the periphery of the contact region, which was not allowed in Hertz model. Therefore, a finite tensile load is required to separate the solids. In JKR model, attractive force exists only when two spheres are in contact and is of infinitely short range. So it predicts the abrupt separation of two spheres (from a finite contact area) once the separating force reaches its pull-off value. Different from JKR model, Derjaguin, Muller, and Toporov (DMT [89]) argued that attractive force between the solids must have a finite range. There should have attractive force outside the contact zone where the surfaces are a small distance apart. According to DMT predictions, the separation of two spheres only happens when the contact area has been reduce to zero. The pull-off force calculated by DMT is $\frac{4}{3}$ times greater than the JKR value.

A comprehensive comparison of JKR and DMT models was ever given by Horn, et al [90]. The arguments between JKR and DMT model in the literature has not been satisfactorily resolved. However, it is normally agreed that DMT is more suitable for hard solids of small radius and low surface energy, while the JKR theory would be more accurate for soft materials with large surface energy and radius. Muller et al has formulated a dimensionless quantity to describe the contact system

so as to decide which model is appropriate [91]. Recently, JKR model has been extended to large contact radii [92].

The consideration of the adhesion of particles arising from impact requires to consider not only the adhesion forces acting upon the bodies but also the mechanisms of energy loss occurring during the impact [93] [94]. Brenner et al considered the impact of a purely plastic particle with a rigid surface, with the recovery stage being due to elastic recovery processes [95]. Rogers and Reed presented a model to describe the adhesion of particles arising from elastic-plastic impacts with a surface, and combined theoretical analysis with experimental studies [76]. In their model, both elastic and plastic deformations are allowed for throughout the impact. Attard and Parker considered the consequences of finite-range surface force and presented the results for two basic forces, an exponential repulsion and a Lennard-Jones adhesion [96]. Brach and Dunn presented a model for the low velocity impact of microspheres with surfaces based on classical impact dynamics and Hertzian theories [97] [98]. It analytically relates the velocity change of the microspheres to the physical parameters of the microspheres and the surface as well as to the microsphere-surface adhesion forces. Johnson and Pollock made use of the JKR theory of adhesive elastic contact to examine interactions between adhesion and inelastic deformations in the impact of predominantly elastic solids [99]. Thornton et al considered impact in the presence of adhesion using the theory developed by JKR [100] $\sim$ [102]. The new theory describes the tangential behavior of two adhered elastic spheres under combined normal and tangential loading. A new sliding criterion is proposed in the new model. Experimental observation shows good agreement with the proposed sliding criterion.

In this chapter, the contact model that is implemented in Aston DEM code is discussed in detail. The model equations for frictional elastic particles and frictional auto-adhesive particles are reviewed respectively. The load-displacement behavior at

the contact of two elastic spheres with friction under normal and tangential loading is studied first. The impact in the presence of adhesion is examined thereafter.

6.3 Contact Model Without and With Adhesion (Thornton et al.)

6.3.1 Time Step

The time step in Aston DEM code is decided by the Rayleigh wave speed of force transmission on the surface of elastic bodies. For an assembly of spherical particles, the highest frequency of Rayleigh wave propagation is determined by the smallest particles, which leading to a critical time step, Δt, given by

$$\Delta t = \frac{\pi R_{\min}}{\lambda}\sqrt{\frac{\rho}{G}} \tag{6.1}$$

where $R_{\min}$ is radius of the smallest particles, ρ is density of the particles, G denotes shear modulus and is calculated by

$$G = \frac{E}{2(1+\nu)} \tag{6.2}$$

where E is Young's modules and ν is Poisson ratio. In Eq. 6.1, λ is related with Poisson ratio ν and is calculated by

$$\lambda = 0.1631\nu + 0.876605$$

It is easy to prove that critical time step that is calculated by Eq. 6.1 has the same magnitude as the time step that is adopted by Walton & Braun model, which is calculated by Eq. 4.1. From one point, this shows the consistence of two DEM models.

6.3.2 Frictional Elastic Particles

For frictional elastic particles, the theory of Hertz (See Johnson [103]) is used to model the normal force-displacement relationship and theory of Mindlin and Deresiewicz [104] for the tangential force-displacement relationship.

a. Normal interactions (Hertzian model)

The normal force-displacement relationship ($N-\alpha$) for particles 1 and 2 with elastic module E_1 and E_2, Poisson ratio ν_1 and ν_2 and radii R_1 and R_2

$$\begin{cases} N = \frac{4}{3}E^* R^{*1/2}\alpha^{3/2} & \text{for no previous normal force} \\ N = K_N \alpha & \text{for a previous normal force} \end{cases} \tag{6.3}$$

K_N is normal stiffness, $K_N = 2E^*a$, where a is the radius of the contact area and

$$a = \sqrt{\alpha R^*} \tag{6.4}$$

E^* is equivalent Young's modulus and R^* is equivalent radius, and they are defined by

$$\begin{aligned} \frac{1}{E^*} &= \frac{1-{\nu_1}^2}{E_1} + \frac{1-{\nu_2}^2}{E_2} \\ \frac{1}{R^*} &= \frac{1}{R_1} + \frac{1}{R_2} \end{aligned}$$

b. Tangential interactions (Mindlin and Deresiewicz model)

The calculation of tangential force adopts an incremental approach. The procedure is to update the normal force and contact area (Eq. 6.3, Eq. 6.4) followed by calculating the incremental tangential force ΔT using the new values of N and a. The incremental tangential force ΔT arising from an incremental tangential displacement $\Delta\delta$ depends on the loading history as well as the normal force and is given as

$$\Delta T = K_T \Delta\delta \tag{6.5}$$

K_T is tangential stiffness and is defined as

$$\begin{cases} K_T = 8G^* a\theta + \mu(1-\theta)\frac{\Delta N}{\Delta\delta} & \text{loading} \\ K_T = 8G^* a\theta - \mu(1-\theta)\frac{\Delta N}{\Delta\delta} & \text{unloading} \end{cases} \tag{6.6}$$

where

$$\frac{1}{G^*} = \frac{1-{\nu_1}^2}{G_1} + \frac{1-{\nu_2}^2}{G_2}$$

G is shear modulus and is calculated by Eq. 6.2. Parameter θ in Eq. 6.6 is decided by loading history,

$$\theta = 1 \qquad \text{if } |\Delta T| < \mu \Delta N \text{ (no-slip solution)} \tag{6.7}$$

Otherwise (partial-slip solution)

$$\theta^3 = 1 - \frac{T + \mu \Delta N}{\mu N} \qquad \text{loading} \tag{6.8}$$

$$\theta^3 = 1 - \frac{T^* - T + 2\mu \Delta N}{2\mu N} \qquad \text{unloading} \tag{6.9}$$

$$\theta^3 = 1 - \frac{T - T^{**} + 2\mu \Delta N}{2\mu N} \qquad \text{reloading} \tag{6.10}$$

and

$$\begin{cases} T^* &= T^* + \mu \Delta N \\ T^{**} &= T^{**} - \mu \Delta N \end{cases} \tag{6.11}$$

Here, μ is the coefficient of friction. The parameters T^* and T^{**} define the loading and unloading reversal points, and need to be continuously updated by the Eq. 6.11 to allow for the effect of varying normal force.

6.3.3 Frictional Auto-adhesive Particles

For auto-adhesive particles, the JKR model which extends the Hertzian model to account for surface energy is used for the normal interactions. For the tangential interactions, a model developed by Thornton which combines the theories of Savkoor and Briggs [105] and Mindlin and Deresiewicz is used.

a. Normal interactions(JKR model)

When surface energy is considered for auto-adhesive particles, the radius of the contact area a is

$$a = \left[\frac{3R^* N'}{4E^*} \right]^{1/3} \tag{6.12}$$

where N' is the effective Hertzian force which would produce the same contact area and is given by

$$N' = N + 2N_c \pm \sqrt{4NN_c + 4{N_c}^2} \tag{6.13}$$

where N is the applied force and $N_c = 1.5\pi\Gamma R^*$ is the pull-off force (Γ being the interface energy).

The relative approach of the two spheres (α) is related to the contact area a by

$$\alpha = \frac{a^2}{R^*} - \sqrt{\frac{2\pi\Gamma a}{E^*}} \tag{6.14}$$

The incremental normal force ΔN corresponding to an incremental relative approach $\Delta\alpha$ is obtained as

$$\Delta N = 2E^* a \left[\frac{3\sqrt{N'} - 3\sqrt{N_c}}{3\sqrt{N'} - \sqrt{N_c}}\right] \Delta\alpha \tag{6.15}$$

The normal stiffness is defined as

$$K_N = 2E^* a \left\{\frac{3-3\left[\frac{a_c^3}{a^3}\right]^{1/2}}{3-\left[\frac{a_c^3}{a^3}\right]^{1/2}}\right\}$$

$$= 2E^* a \left[\frac{3\sqrt{N'}-3\sqrt{N_c}}{3\sqrt{N'}-\sqrt{N_c}}\right] \tag{6.16}$$

where a_c is the contact radius when $N = -N_c$, and

$$a_c^3 = \frac{3N_c R^*}{4E^*} \tag{6.17}$$

b. Tangential interactions (JKR model)

On initial application of a tangential force, a peeling mechanism results in a reduction of the contact area and tangential interactions are modeled using the no-slip solution of Mindlin [104].

$$T = 8G^* a\delta \tag{6.18}$$

with the incremental tangential force ΔT and the contact area a given by

$$\Delta T = 8G^* a\Delta\delta \tag{6.19}$$

$$a^3 = \frac{3R^*}{4E^*}\left[N + 2N_c \pm \sqrt{4NN_c + 4{N_c}^2 - \frac{T^2E^*}{4G^*}}\right] \tag{6.20}$$

Equation 6.20 indicates a reduction in the contact radius under increasing tangential force. Savkoor and Briggs suggested that this corresponds to a 'peeling' mechanism which continues in a stable manner until a critical value T is reached [105], given by the equation,

$$T_c = 4\sqrt{\frac{G^*}{E^*}(NN_c + {N_c}^2)} \tag{6.21}$$

When the process is complete and the contact area is reduced to

$$a_p^3 = \frac{3R^*}{4E^*}(N + 2N_c) \tag{6.22}$$

Thornton [102] argues that peeling must occur before sliding, followed by a smooth transition to sliding. If at the end of peeling the critical tangential force T_c is less than the sliding force, a subsequent slip annulus is assumed to spread radially inwards and the partial-slip solution of Mindlin and Deresiewicz [66] is applied until sliding occurs. The equations used in this case are Eq. 6.5 $\sim$ Eq. 6.10 with N replaced by $N + 2N_c$. If the tangential force at the end of peeling is greater than the sliding force, the tangential force immediately falls to the sliding force. Two sliding criteria are used for modeling the post-peeling behavior. For negative normal loads when $N < -0.3N_c$,

$$T = \mu N'\left[1 - \frac{N' - N}{3N'}\right]^{3/2} \tag{6.23}$$

is used, where,

$$N' = N + 2N_c + 2(NN_c + {N_c}^2)^{1/2} \tag{6.24}$$

Otherwise,

$$T = \mu(N + 2N_c) \tag{6.25}$$

is employed

6.4 Oblique Impact of Elastic Spheres With and Without Adhesion

The oblique impact of two elastic spheres with friction is implemented first. Figure 6.1 shows the initial configuration of the system. Two identical spheres are created with the following properties: $R = 100$ μm, $\rho = 2.65$ Mg/m^3, $E = 70$ GPa, $\nu = 0.3$ and $\mu = 0.35$. Each sphere was specified velocity 0.05 m/s in the vertical direction. A series simulations were performed for different values of impact angle θ.

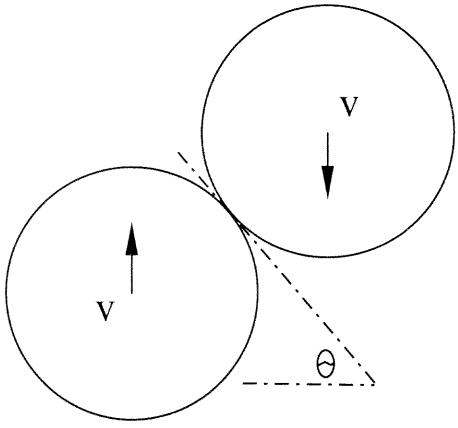

Figure 6.1 Impact configuration

Five typical loading paths corresponding to five impact angle are shown in Fig. 6.2. The related evolution of the tangential force-displacement behavior is shown in Fig. 6.3. The angle of inter-particle friction for impact spheres is 19^o. For small impact angles, e.g., 15^o (less than the angle of inter-particle friction), the limiting condition $|T| = \mu N$, associated with rigid body sliding, only occurs during the final stages of the impact, as shown in Fig. 6.2. However, energy is dissipated as a result of microslip prior to rigid body sliding as shown in the corresponding force-displacement curves, Fig. 6.3. If the impact angle is greater than the angle of internal friction, e.g., 30^o or greater, rigid body sliding occurs from the start of the impact and continues until the decelerating relative tangential motion of the spheres . Subsequently, as the resultant force rotates, the tangential force reduces, reverses in direction and finally

towards the end of the impact rigid body sliding recurs. For a larger impact angles, e.g., 75^o, rigid body sliding continues throughout the impact with no reversal of the tangential force direction.

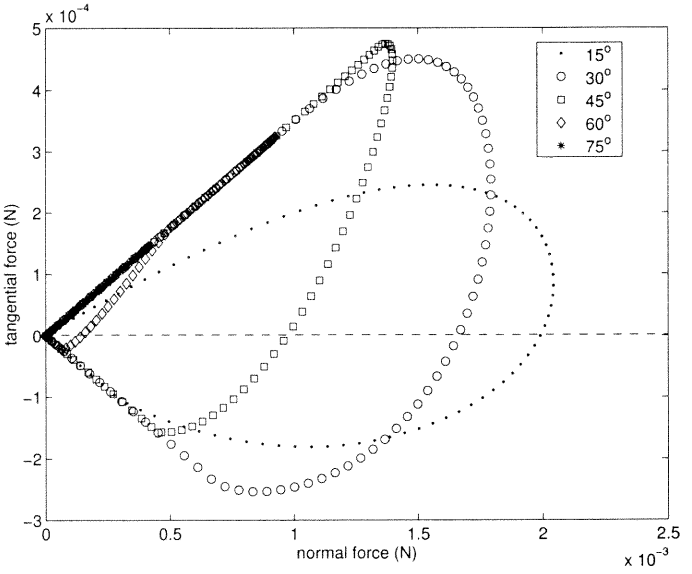

Figure 6.2 Effect of impact angle on loading path (without adhesion)

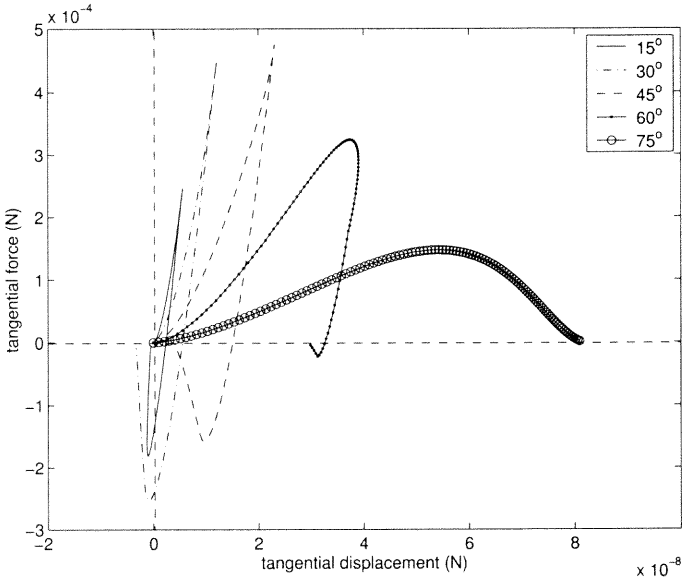

Figure 6.3 Effect of impact angle on tangential force displacement behavior (without adhesion)

Figure 6.4 to Fig. 6.10 are the results of computer simulated oblique impact experiments with identical particle properties and initial velocities as the previous tests but with an effective surface energy $\gamma = 0.2$ J/m^2. Figure 6.4 to Fig. 6.8 provide a comparison between the loading paths followed for impacts with and without adhesion. Figure 6.9 shows effect of impact angle on the loading path under the case of adhesion. For all cases with adhesion, at the start of the impact, the ratio $\Delta T/\Delta N$ is almost constant and slightly greater than $tan\ \theta$, where θ is the impact angle, due to the difference between the tangential and normal contact stiffnesses.

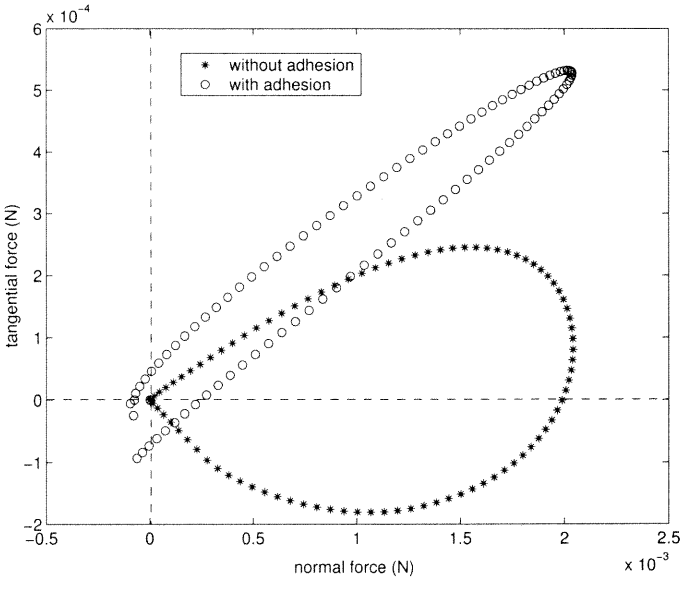

Figure 6.4 Loading paths (with and without adhesion) at $\theta = 15^o$

Except for small impact angles, e.g., 15^o, which is less than the angle of internal friction, the contact peels and then slides as the normal force increases. Subsequent behavior is similar to that for no adhesion with rigid body sliding recommencing towards the end of the impact. Moreover, as can be seen from Fig. 6.4 to Fig. 6.7, adhesion permits much higher tangential forces to be generated and, provided that the impact velocity is small enough to prevent a peeling failure when the normal force is increasing. Figure 6.10 shows the relationship of tangential force with tangential

displacement. More energy is dissipated as a consequence of the larger contact area due to adhesion. However, once peeling has occurred, the behavior is essentially similar to the case with no adhesion. The detailed description of the contact model of two adhered elastic spheres under combined normal and tangential loading is presented in [106].

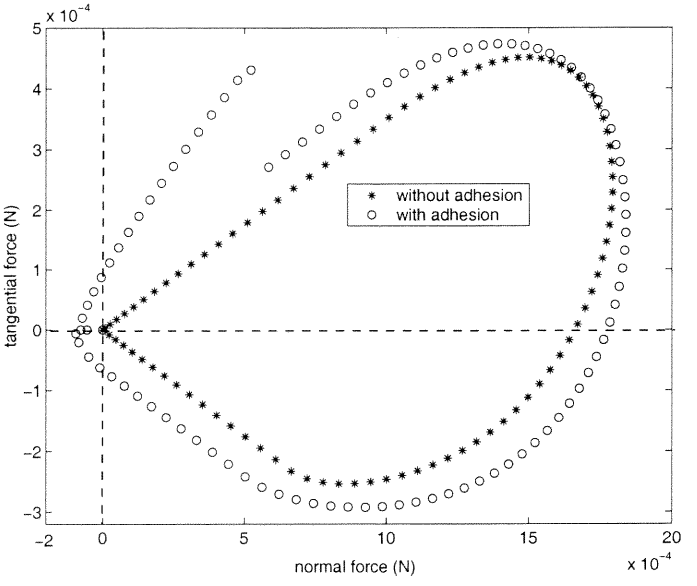

Figure 6.5 Loading paths (with and without adhesion) at $\theta = 30^o$

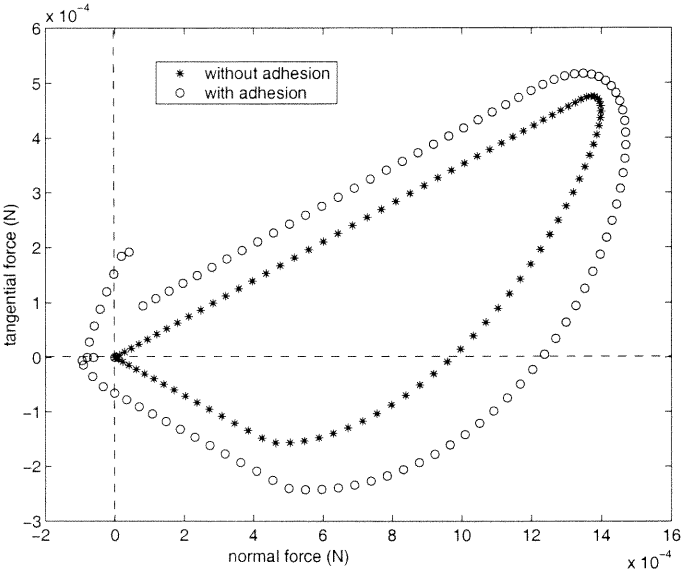

Figure 6.6 Loading paths (with and without adhesion) at $\theta = 45^o$

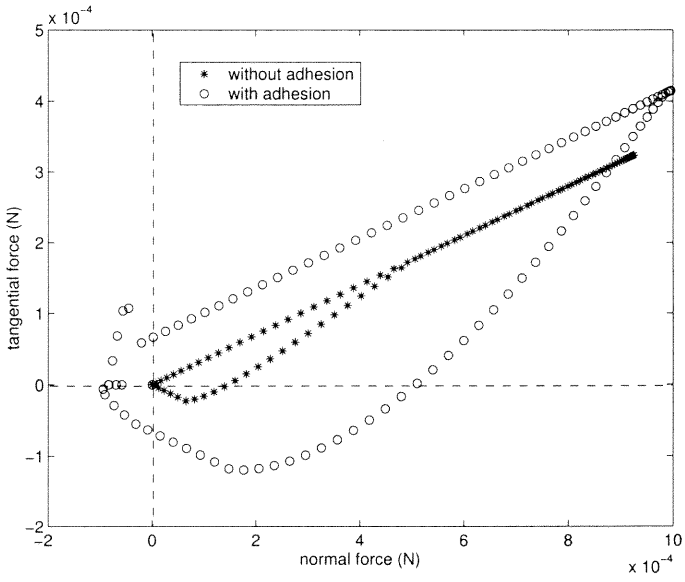

Figure 6.7 Loading paths (with and without adhesion) at $\theta = 60^o$

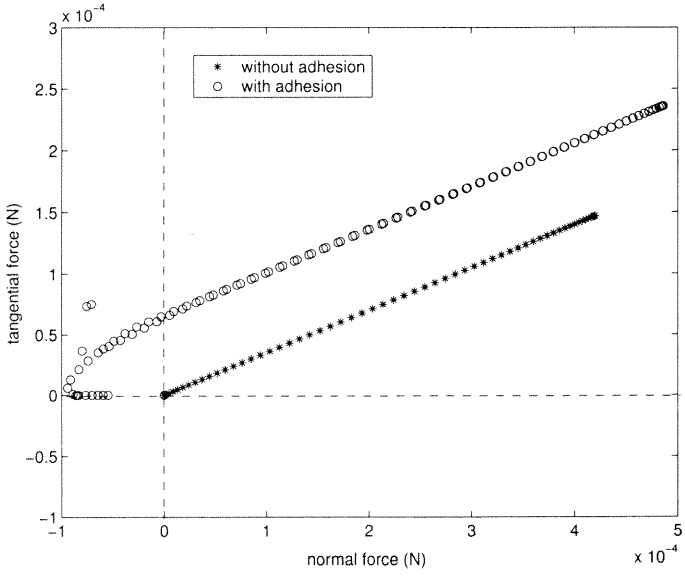

Figure 6.8 Loading paths (with and without adhesion) at $\theta = 75^o$

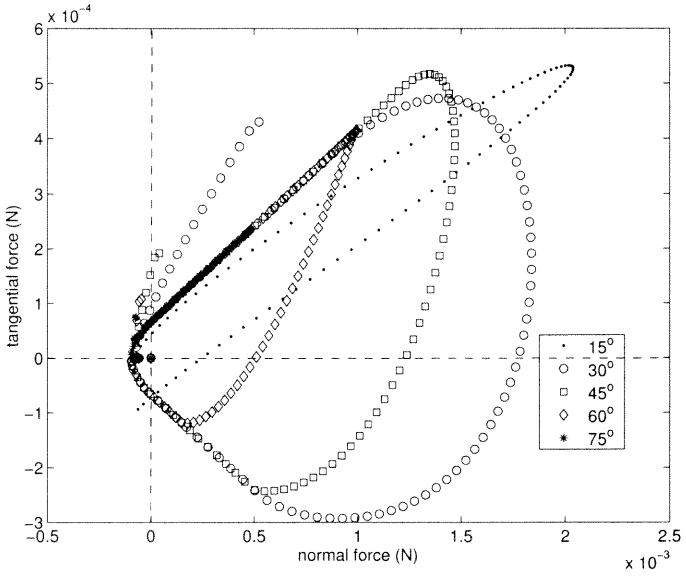

Figure 6.9 Effect of impact angle on loading paths with adhesion

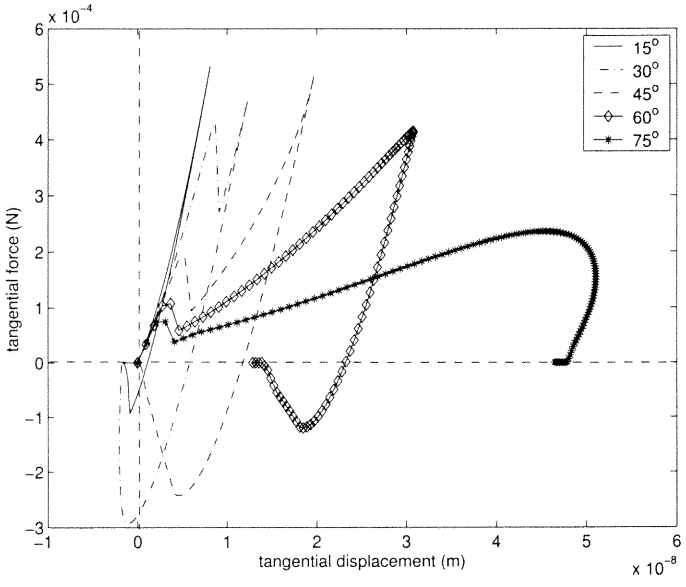

Figure 6.10 Impact angle on tangential force displacement behavior with adhesion

CHAPTER 7

EVOLUTION OF AGGLOMERATE DAMAGE/FRACTURE PROCESS IN MECHANOFUSION SYSTEM

7.1 Introduction

The numerical simulation of Mechanofusion system for dry particle coating does not take into consideration of the function of guest particles. There are couple of reasons for the current mono-dispersed system simulation:

- The large size difference of host particle with that of guest particle. If the guest particle is considered in the system simulation, the time step, which is depended on the size of small particles here, will be even smaller.

- If the system simulation includes guests particles, it would be very hard for the hardware to deal with the huge number of guest particles.

- The numerical results from the system simulation can still be used to estimate the coating degree and required coating time assumed that guest particles are already evenly dispersed on the surface of host particles before processing.

It is known that, the guest particles are normally in the form of agglomerates. The question unsolved here is how the guest agglomerates deagglomerate during the processing before dry particle coating happens. Over the years studies, it was found that degradation of agglomerates resulted from attrition and fragmentation as they collide with each other and with the process equipment. In Mechanofusion system, agglomerates are broken down by shearing, compression or impact with each other, with host particles and with the equipment. The real interactions inside the system are very complicated. Therefore, it is impossible to create a simply model that can cover all the related interactions. This study will examine the fracture of single agglomerate under normal interactions with a host particle and with boundary walls based on the information obtained from the system simulation.

In practical, agglomerates may have different sizes, irregular shapes and different packing properties. The agglomerate used in the test is assumed to have same size and spherical shape with random packing property. The fracture of the agglomerate during normal interactions with a host particle, a boundary wall, or two boundary walls (for the diametrical compression tests) under different impact velocities is examined by Aston DEM code, which takes use of the "soft sphere" approach and enables the simulation of auto-adhesive particles. The simulations are performed in two-dimensional mode.

7.2 Results From System Simulation

Since the fragmentation study of the agglomerate is based on the binary impact, it is necessary to obtain useful information of the system such as relative interactions inside the system to guide the numerical study. The numerical result from the system simulation illustrates contact force distribution inside the system, which is figured in Fig. 7.1 $\sim$ Fig. 7.4 in terms of areas. If the interactions are normalized to normal interaction and from the relationship of:

$$F_{max} = 0.02\Delta v$$

where F_{max} is the maximum contact force and Δv is the relative impact velocity. The relative impact velocity distribution inside areas is obtained and expressed in Fig. 7.5 $\sim$ Fig. 7.8.

The results show that the relative impact velocities have a very wide distribution inside the system. Inside the input area and free-diffusion area, almost half of the relative impact velocity is less than 0.1 m/s. From another point of view, the interactions inside these two areas are weak, which is expected from the inter-force calculation by the system simulation. On the contrary, the interactions inside the inner-piece area and the scraper area is much stronger. More than 50 % relative

impact velocity is larger than 0.2 m/s. Moreover, inside the scraper area, more than 10 % relative impact velocity is larger than 1.0 m/s. The larger interactions inside the inner-piece and the scraper area are also shown from the inter-force analysis by the system simulation.

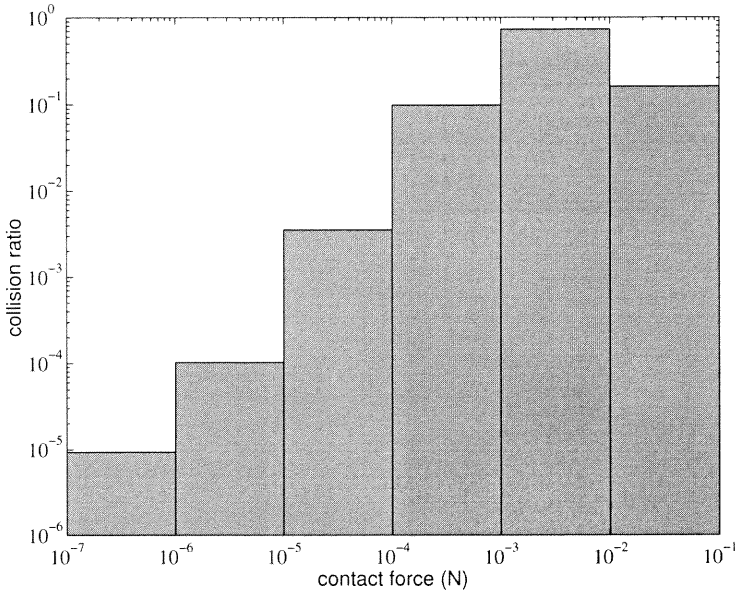

Figure 7.1 Contact force distribution inside the inner-piece area

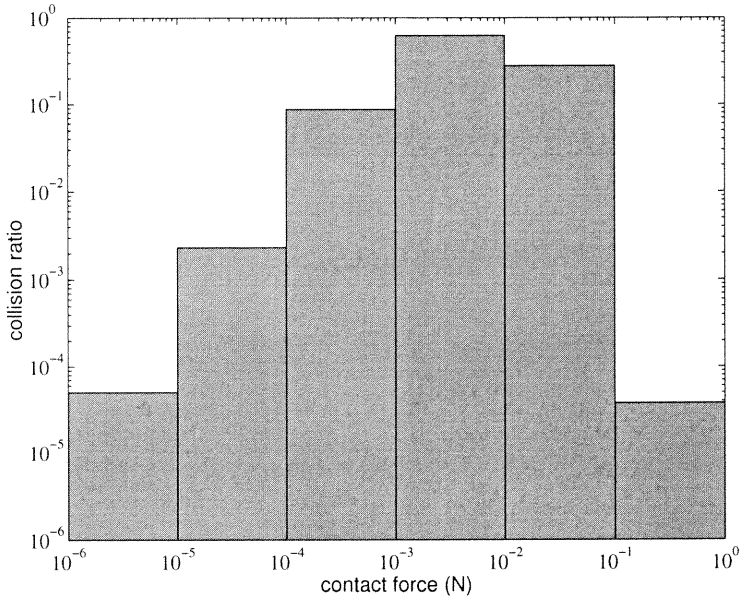

Figure 7.2 Contact force distribution inside the scraper area

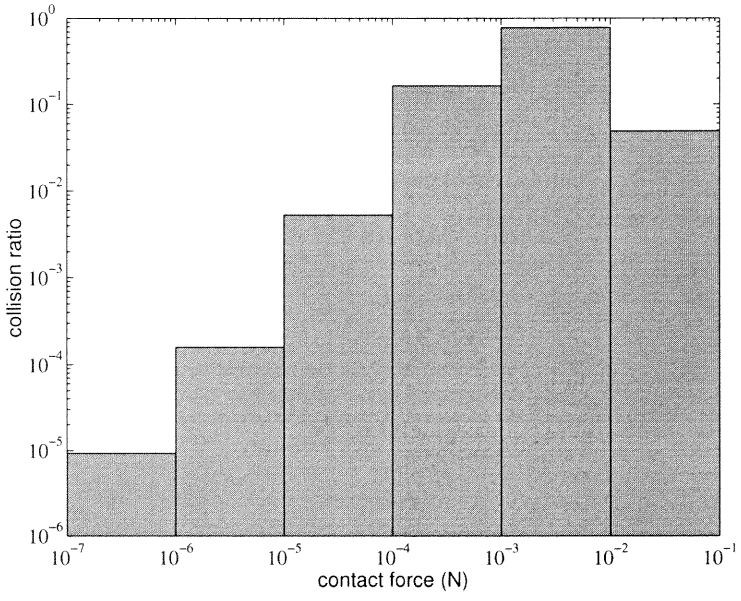

Figure 7.3 Contact force distribution inside the input area

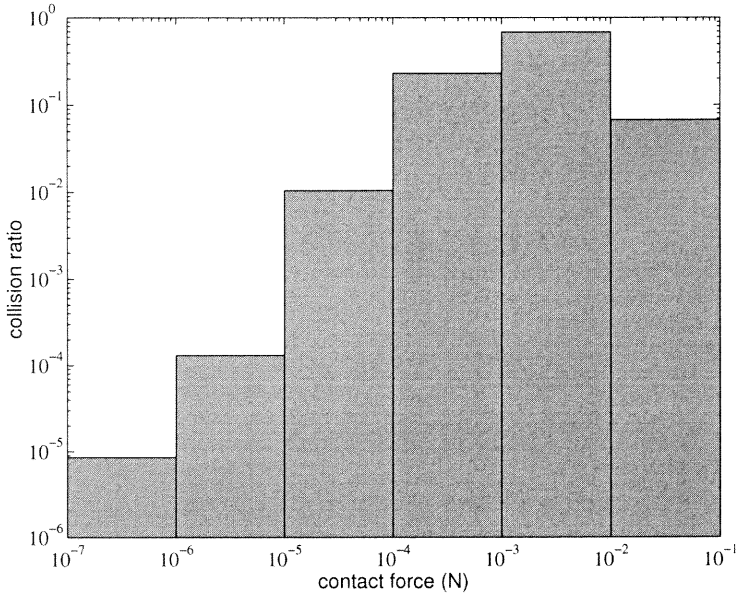

Figure 7.4 Contact force distribution inside the free-diffusion area

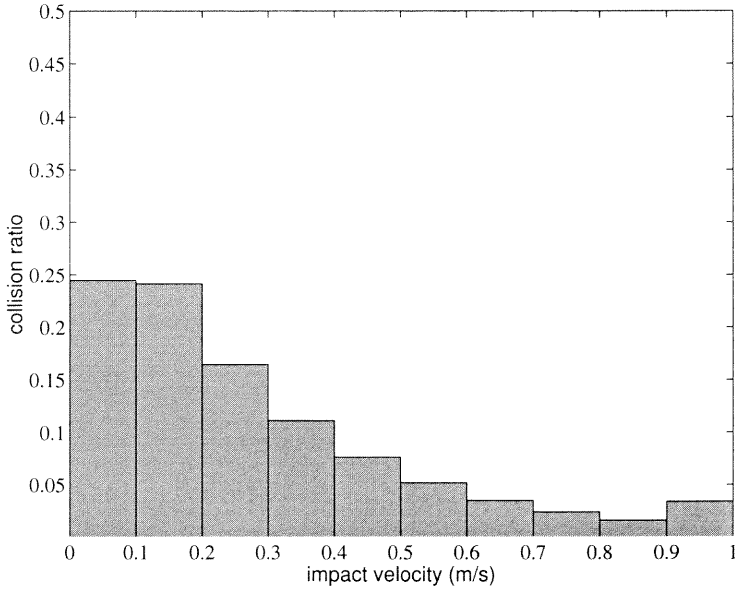

Figure 7.5 Impact velocity distribution inside the inner-piece area

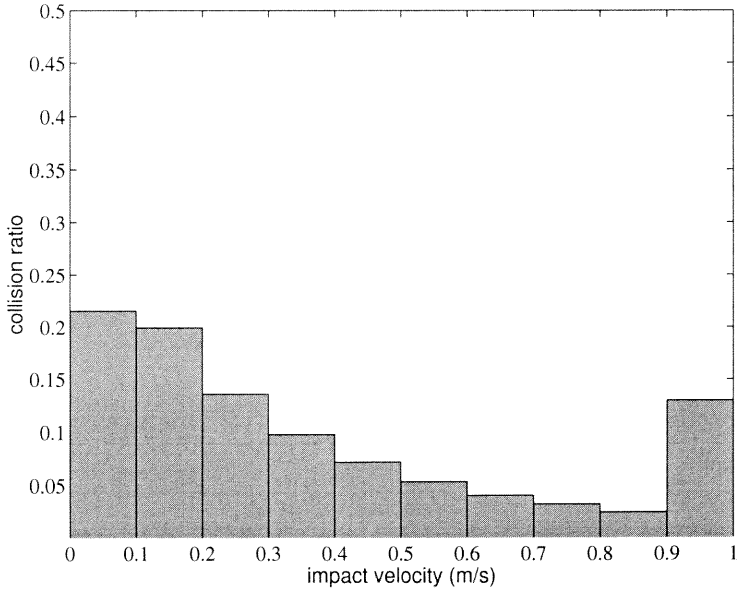

Figure 7.6 Impact velocity distribution inside the scraper area

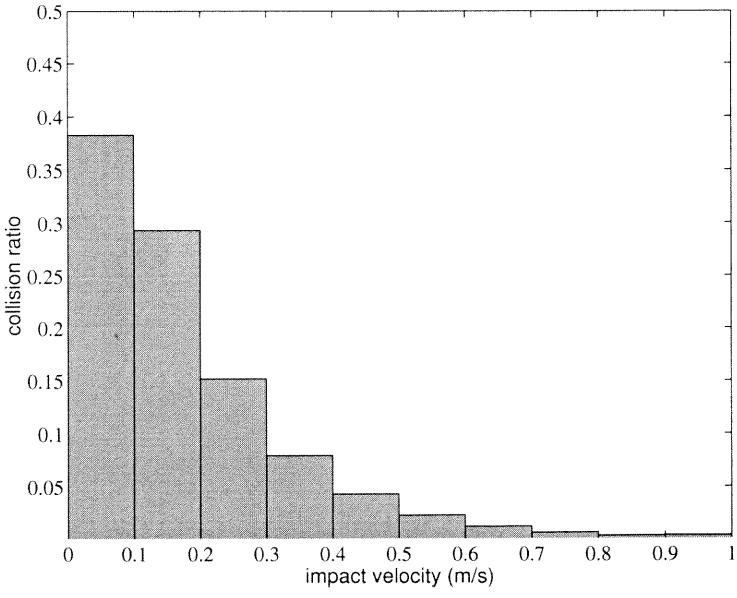

Figure 7.7 Impact velocity distribution inside the input area

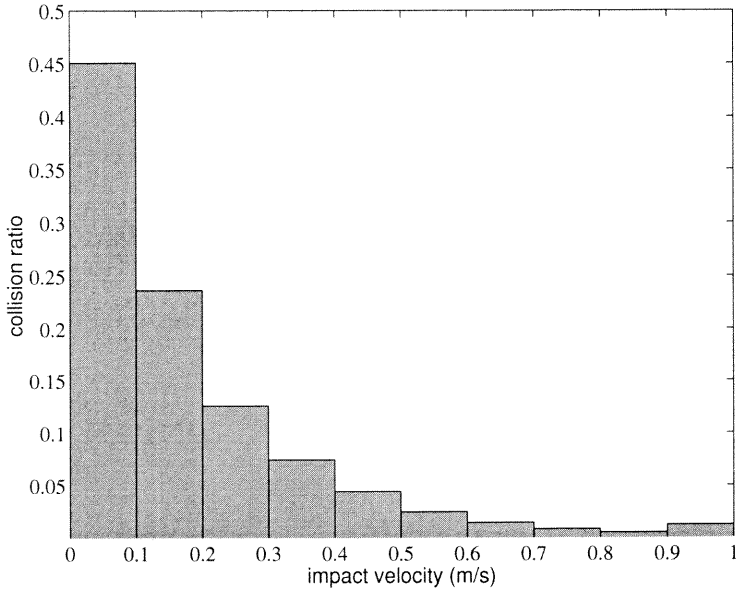

Figure 7.8 Impact velocity distribution inside the free-diffusion area

7.3 Preparation of the Agglomerate

The agglomerate used in the simulation study consists of primary particles with the following mechanical properties: density, $\rho = \mathbf{3970\ Kg/m^3}$; Young's modulus, $\mathbf{E = 345\ GPa}$; Poisson's ratio, $\nu = \mathbf{0.26}$ and the coefficient of interface friction, $\mu = \mathbf{0.25}$. With these properties, particles may be considered to be composed of Al_2O_3. The agglomerate preparation stage begins with the generation of spherical particles in a specified spherical region. There are two ways to create primary particles: one is regular packing and another is random packing. In this study, the agglomerate with random packing will be examined.

Systems of equal-sized spheres have a natural tendency to form clusters of regular packed zones. Therefore, in order to avoid this, it was decided to use seven slightly different particle sizes in the range 5 μm $\pm$ 5%. The particle size distribution chosen for the agglomerate created is shown in Fig. 7.9. To prepare the random agglomerate, the primary particles are initially created at random locations within a designated spherical volume and then brought together in contact by applying a centripetal gravity field. To obtain a dense agglomerate, it is necessary to apply the centripetal gravity field to the system using zero inter-particle friction and to introduce the desired values of inter-particle friction and interface energy as late as possible in the preparation stage [107].

After obtaining the agglomerate with the desired friction and interface energy, it is important to remove the centripetal gravity field gradually and carefully in order to preserve the agglomerates equilibrium state. Therefore, at the end of the preparation stage, the particle velocities and contact forces are very low - with the number of compressive contact forces approximately equal to the number of tensile contact forces. An image of 217 particles, which are included in a circle with a diameter of 100 μm (in two-dimensional), with an average size of 5 μm just after their creation is presented in Fig. 7.10. Figure 7.12 shows the random packing agglomerate at

the end of the preparation stage with 216 inter-particle bonds. The diameter of the agglomerate is 87 μm. Two values of interface energy 1.0 and 2.0 J/m^2 were used for the test.

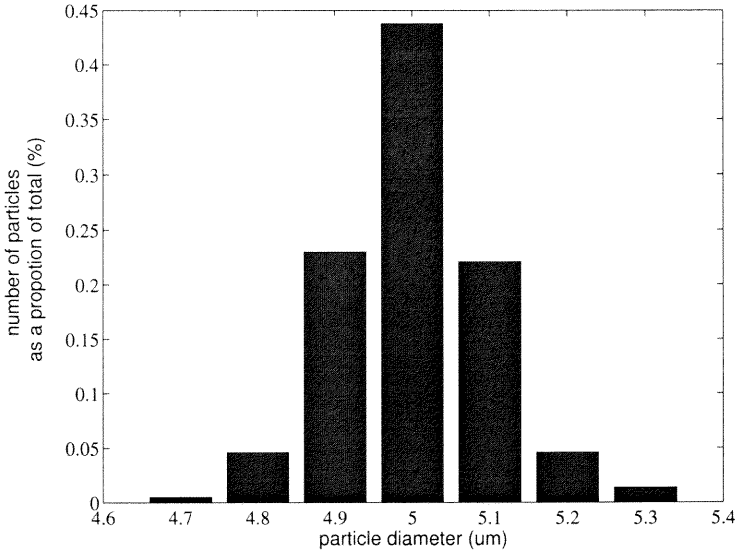

Figure 7.9 The particle size distribution for the random packing agglomerate

7.4 Numerical Methodology and Simulation Procedures

The Aston DEM code is capable of modeling elastic, frictional, adhesive or non-adhesive spherical primary particles with or without plastic yield at the inter-particle contacts. In this study, the adhesive option with no plastic deformation at the contact is used. The detail description of the interaction laws have been reported by Thornton, et al. and is reviewed in detail in the previous chapter.

After the creation of the agglomerate, a host particle or a wall (or two walls under diametrical compression test) is created at very small distance from the agglomerate with an assigned velocity. The damage of the agglomerate is evaluated by debris ratio and damage ratio. The *damage ratio* is defined as the ratio of the number of contacts that have been broken to the initial number of contacts prior to the test. The *debris ratio* is the ratio of the mass of debris (fragments of under 2.5 % mass of the initial agglomerate mass) produced to the mass of the agglomerate at

the start of the test. Here, *fragment* is an assemblage of particles produced by the fracture or fragmentation of the agglomerate. A fragment behaves as an individual entity (e.g. all particles in a fragment move together). There are several terms used to describe the fragment according to its size [107]:

- Large fragment: a fragment having over 10 % of the mass of the original agglomerate.

- Medium-sized fragment: a fragment having between 2.5 % and 10 % of the mass of the original agglomerate.

- Small fragment or Debris: a fragment having under 2.5 % of the mass of the original agglomerate.

- Fines or finest debris (smaller fragments): clusters consisting of under 0.2 % of the mass of the original agglomerate.

7.5 Evolution of the Agglomerate Damage During Normal Impact With a Host Particle

Figure 7.11 is the interaction diagram. Here, the agglomerate experiences normal impact with a host particle. The host particle has the following parameters: density, $\rho = \mathbf{1190\ Kg/m^3}$; diameter, $\mathbf{d = 400\ \mu m}$; Young's modulus, $\mathbf{E = 3300\ MPa}$; Poisson's ratio, $\nu = \mathbf{0.5}$ and the coefficient of interface friction, $\mu = \mathbf{0.30}$. To simplify the impact situation, it is assumed that two elements have the same incoming velocity. At the beginning of the impact, the desired impact velocity was attributed to all the constituent primary particles. Cyclic calculations were continued until the impact system got a steady state which was indicated by a zero rate of bond breakage and a constant kinetic energy of the system. This test was performed under the different impact velocities and surface energy.

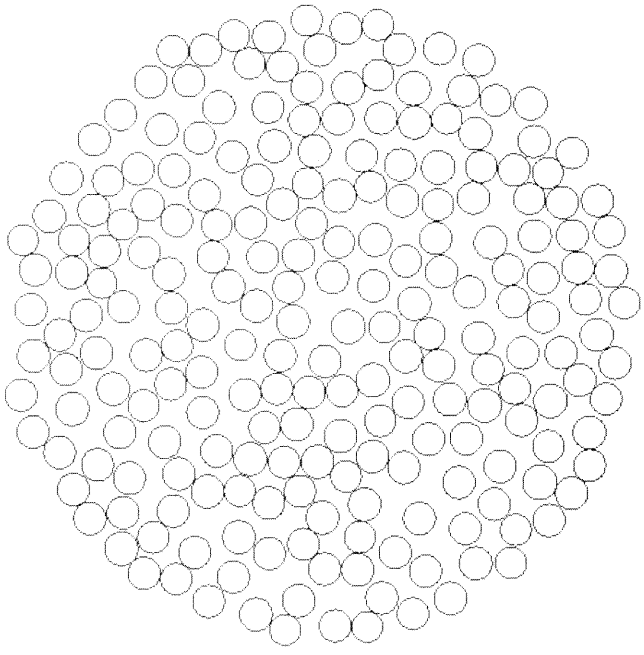

Figure 7.10 Start of preparation stage: for the random packing agglomerate

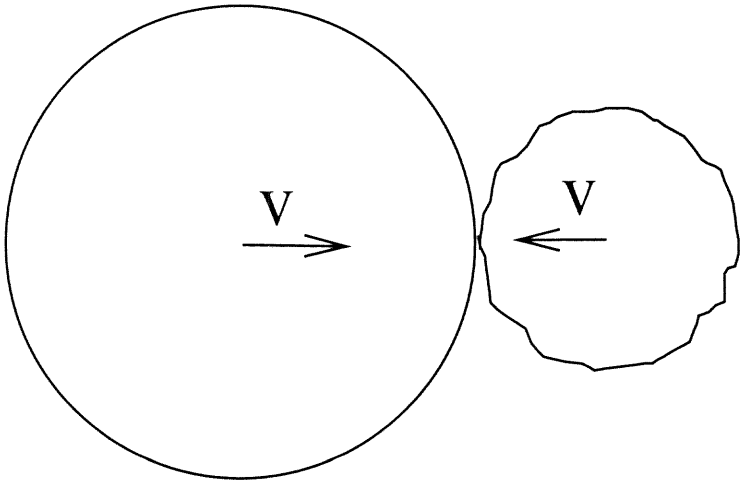

Figure 7.11 Breakage of the agglomerate under binary impact with a host particle

7.5.1 Effect of Impact Velocity

Effect of impact velocity to the degradation of single agglomerate during normal interaction with a host particle is studied next using the surface energy, $\Gamma = 1.0$ J/m^2. Except that under very small impact velocity (v < 0.1 m/s), the agglomerate rebounded without damage. However, the agglomerate seemed to store lots of energy during the impact. The stored energy dissipated after the impact and caused fracture of the agglomerate during the restoration period.

7.5.1.1 Impact Causing Fracture/Fragmentation. For an impact velocity of 0.1 m/s, the agglomerate rebounded while fracture formed inside the agglomerate. Figure 7.13 illustrates the imagine at the end of impact. During the impact, only a small percentage of the initial bonds were broken, and resulted in a small amount of debris at the end of impact. Figure 7.14 shows the clust at the end of impact, where the primary particle which constituted the broken cluster are colored grey. Figure 7.15 presents the evolution of the debris ratio and damage ratio during the test. The damage ratio increased slightly throughout the loading and unloading stages, while the debris appeared only at the end of the impact with a very small amount. However, both damage ratio and debris ratio jumped up at the initial stage of rebounding and gradually leveled off, and at the end of the test there was only two large fragments left and lots of debris created.

7.5.1.2 Impact Causing Further Fracture/Fragmentation and Initial Shattering. When impacted at a velocity of 0.4 m/s, the agglomerate fractured into two large and some small fragments at the end of impact. The imagine in Fig. 7.16 presents aspects observed at the end of test. In Fig. 7.17 the primary particle which constituted the surviving cluster are colored black. Figure 7.18 presents the evolution of the debris ratio and damage ratio during

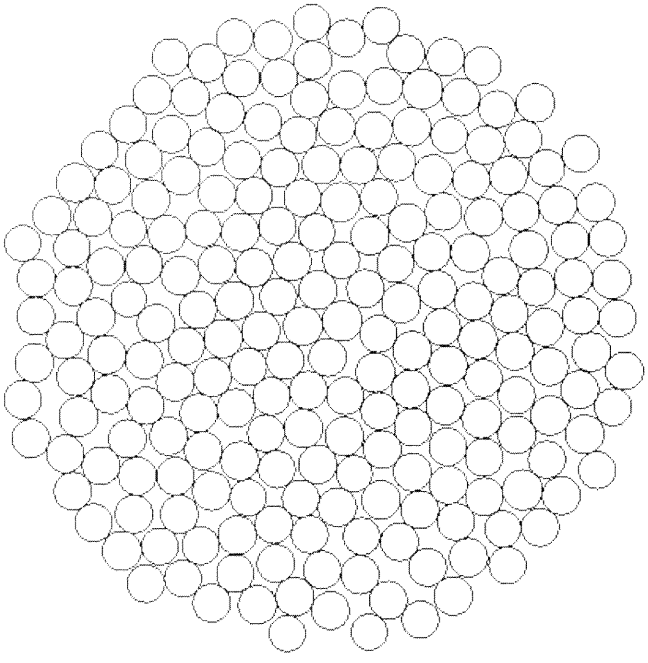

Figure 7.12 A random packing agglomerate at the end of preparation stage

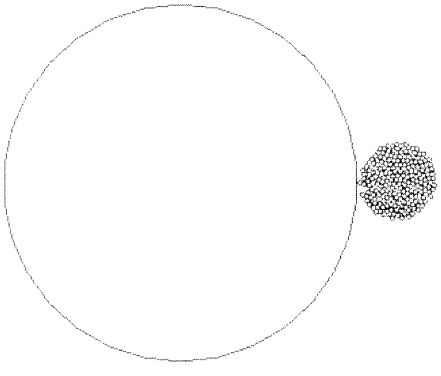

Figure 7.13 Imagine at the end of impact test at v = 0.1 m/s

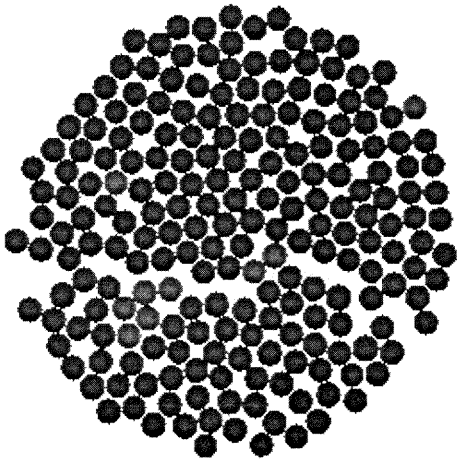

Figure 7.14 Cluster at the end of impact test at v = 0.1 m/s

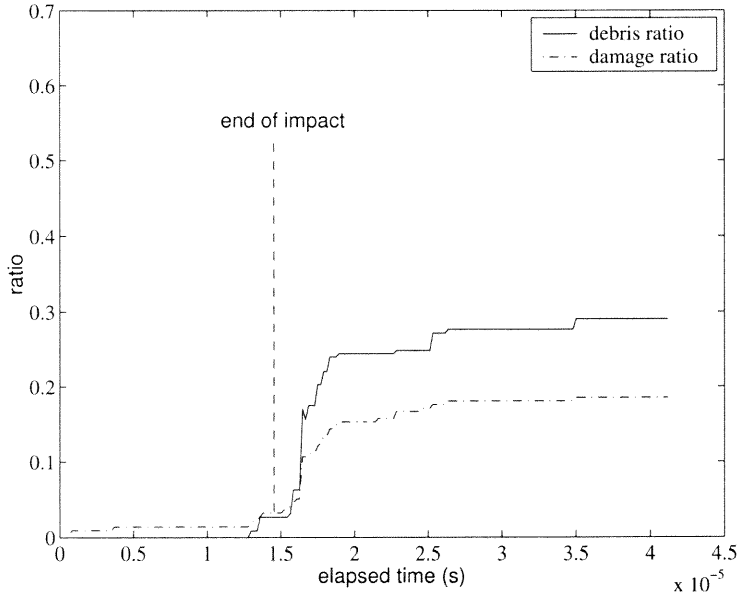

Figure 7.15 Evolution of damage ratio and debris ratio at v = 0.1 m/s

the test. The debris ratio and damage ratio increased gradually throughout the loading and unloading stages. The fragmentation still gradually developed during rebounding period and at the end of test there was some debris around impact area.

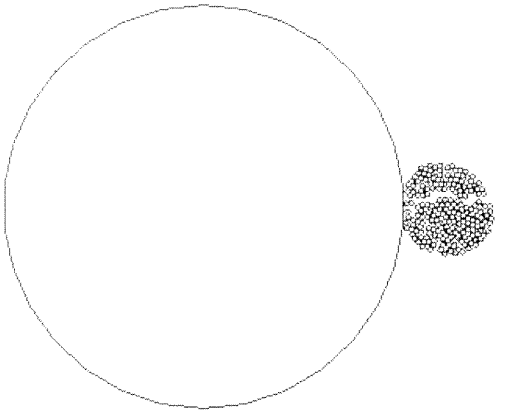

Figure 7.16 Imagine at the end of impact test at v = 0.4 m/s

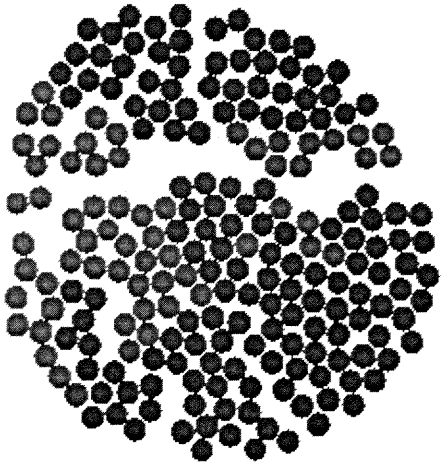

Figure 7.17 Cluster at the end of impact test at v = 0.4 m/s

7.5.1.3 Impact Causing Shattering.

The agglomerate shattered when impact velocity goes to 1.0 m/s. The high impact velocity broke the agglomerate into many small fragments and debris. There is no large fragment survived at the end of the impact. The imagine in Fig. 7.19 presents aspects observed at the end of test. In Fig. 7.20 the primary particle which constituted the surviving cluster are colored black. Figure 7.21 presents the evolution of the debris ratio and damage ratio during the test. The debris ratio and damage ratio increased dramatically during impact period, and reached a maximum value as the agglomerate rebounding off the host surface. Both the damage ratio and the debris ratio had less change once rebound occurred. Another phenomenon that can be observed from this study is the higher impact velocity induces less impact time. The impact time reduced from 15 μs when the impact velocity is 0.1 m/s to 2.5 μs when the velocity increased to 1.0 m/s, which is shown in Fig. 7.15 and Fig. 7.21, respectively.

7.5.2 Effect of Surface Energy

While the agglomerate has larger surface energy, the contact bonds between particles become stronger. Figure 7.22 is the evolution of damage ratio and damage ratio at v = 1.0 m/s with surface energy of $\Gamma = 2.0$ J/m^2. During initial loading, there is no damage of bonds, and debris appeared only after the agglomerate had certain kind of damage. Figure 7.23 is the evolution of debris ratio as a function of surface energy under same impact velocity (here v = 1.0 m/s). The maximum debris ratio at the end of impact for the agglomerate with larger surface energy is 10 % less than the agglomerate with smaller surface energy .

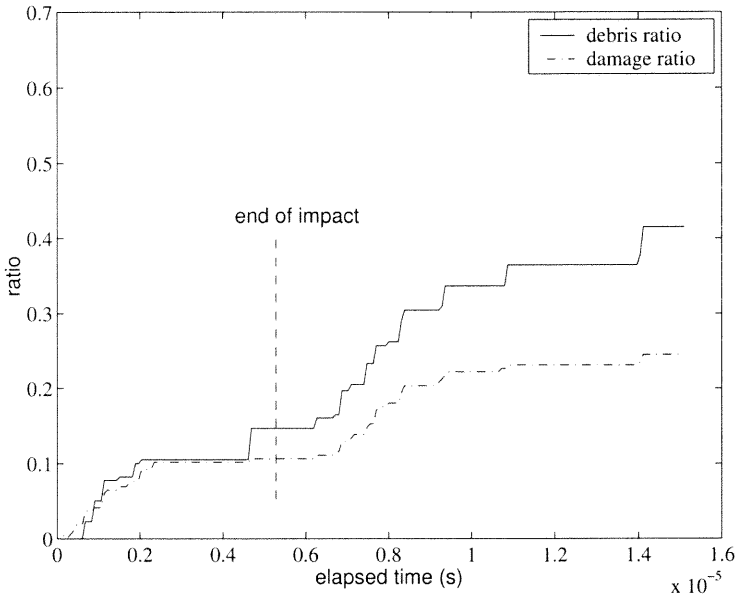

Figure 7.18 Evolution of damage ratio and debris ratio at v = 0.4 m/s

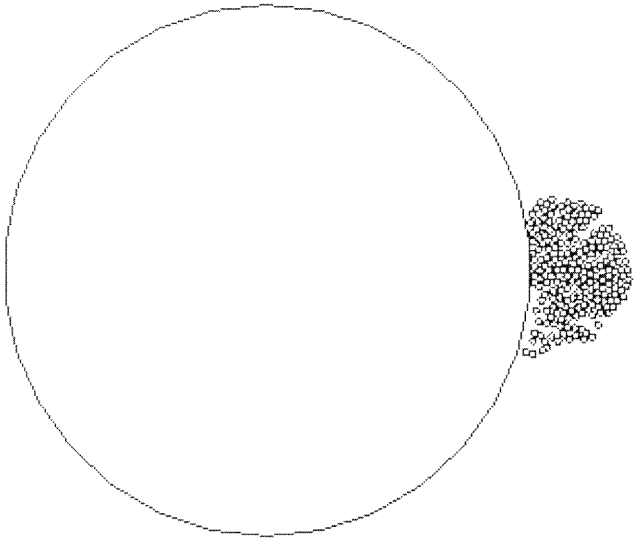

Figure 7.19 Imagine at the end of impact test at v = 1.0 m/s

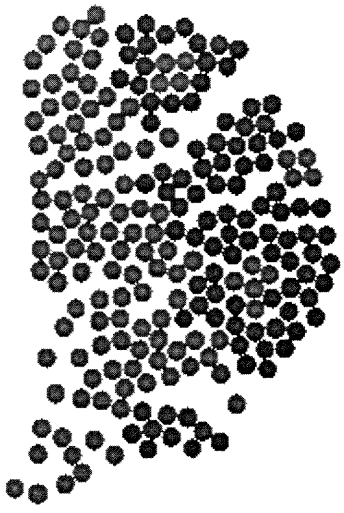

Figure 7.20 Cluster at the end of impact test at v = 1.0 m/s

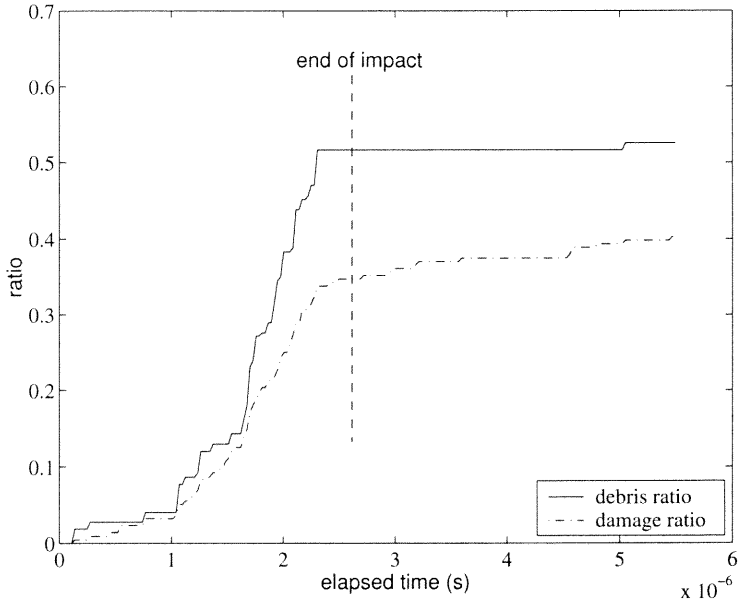

Figure 7.21 Evolution of damage ratio and debris ratio at v = 1.0 m/s

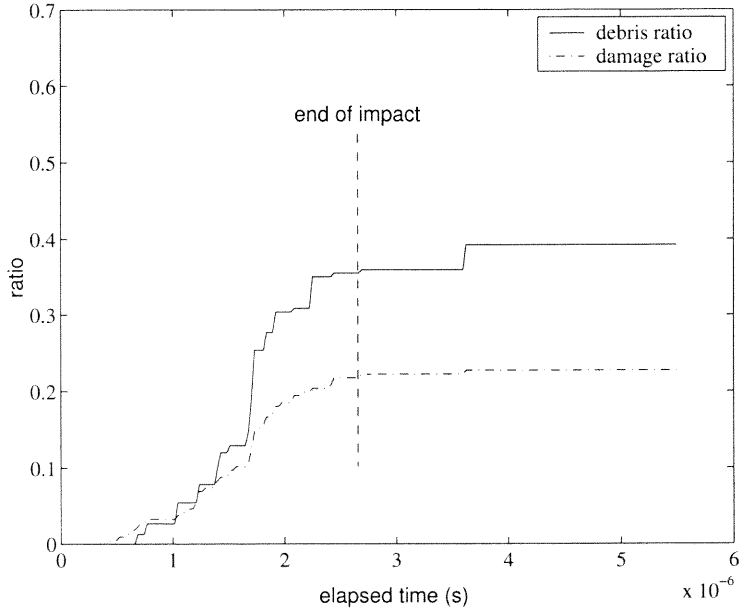

Figure 7.22 Evolution of damage at v = 1.0 m/s , $\Gamma = 2.0$ J/m^2

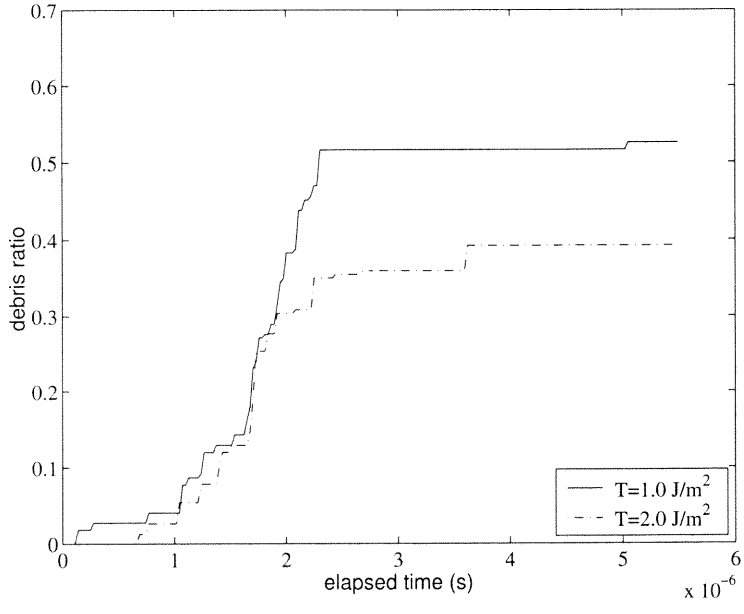

Figure 7.23 Evolution of debris at $\Gamma = 1.0$ J/m^2 and 2.0 J/m^2 and v = 1.0 m/s

7.6 Evolution of the Agglomerate Damage During Normal Impact With a Wall

The degradation of the agglomerate during normal impact with a wall is studied in the following section. Figure 7.24 is the interaction diagram. Here, the wall is a stationary wall with the following properties: density, $\rho = \mathbf{6000\ Kg/m^3}$; Young's modulus, $\mathbf{E = 1000\ GPa}$; Poisson's ratio, $\nu = \mathbf{0.45}$ and the coefficient of interface friction, $\mu = \mathbf{0.5}$. The tests were carried out under different impact velocities of the agglomerate to the wall. The surface energy for the agglomerate is $\Gamma = 1.0\ \mathrm{J/m^2}$ For each test, the simulation was continued till there was no force on the wall and system reached a steady state.

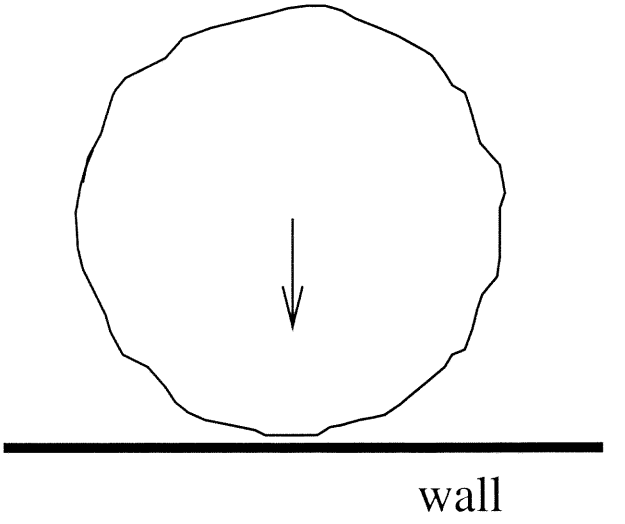

Figure 7.24 Normal impact of an agglomerate with a wall

When the impact velocity was under v = 0.1 m/s, the agglomerate deformed elastically. The fractures were created during the impact, and the agglomerate was broken into three big fragments and two medium-sized fragments, but there was no debris. Figure 7.25 shows the cluster after the impact. When the impact velocity went to v = 0.2 m/s, the agglomerate was broken into two large fragments and some medium-sized fragments as well as a small amount of debris. The debris focused inside the impact area and is shown in grey color in Fig. 7.26. When the

increased to v = 0.5 m/s, the agglomerate fractured during the impact. There was only two large fragments survived after the impact. A lot of small fragments and fines created at the end of the test, which is shown in Fig. 7.27. The debris concentrated inside the impact area. The shattering happened when velocity went to v = 1.0 m/s. The created medium and small sized fragments as well as fines and singles at the end of impact is shown in Fig. 7.28. There was no big agglomerate survived after the impact and the agglomerate shattered to the surface of the impacting wall. Fracture pattern of the agglomerate under this test is in good agreement with related work done in three-dimensional simulation [108] [109]. Figure 7.29 is the development of debris ratio as a function of the impact velocity, and, Figure 7.30 is the development of damage ratio as a function of the impact velocity. There was no debris when the impact velocity was less than 0.2 m/s. When the impact velocity was greater than 0.2 m/s, the debris ratio and damage ratio increased with the impact velocity. The broken bonds and debris appeared early under the higher impact velocity. Debris increased greatly when the velocity went to 0.5 m/s, and the corresponding change is also illustrated in the figure of the damage ratio. When shattering happened (v = 1.0 m/s), the debris ratio went to 60 % at the end of the test. However, the damage ratio was just 40 %. It can be seen that debris was in the state of fines where single primary particle still had some connecting bonds with others.

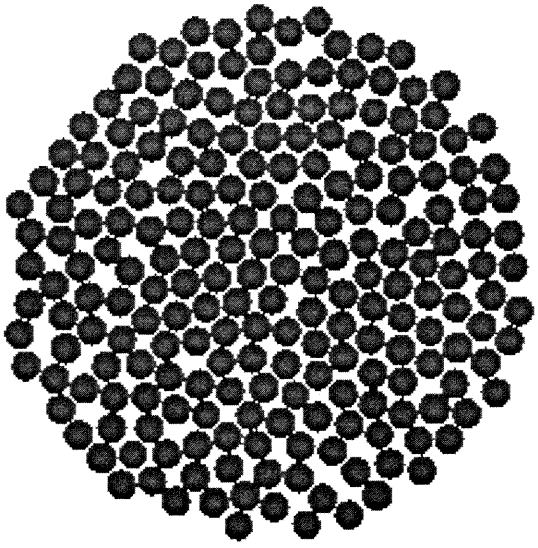

Figure 7.25 Cluster at the end of impact test at v = 0.1 m/s

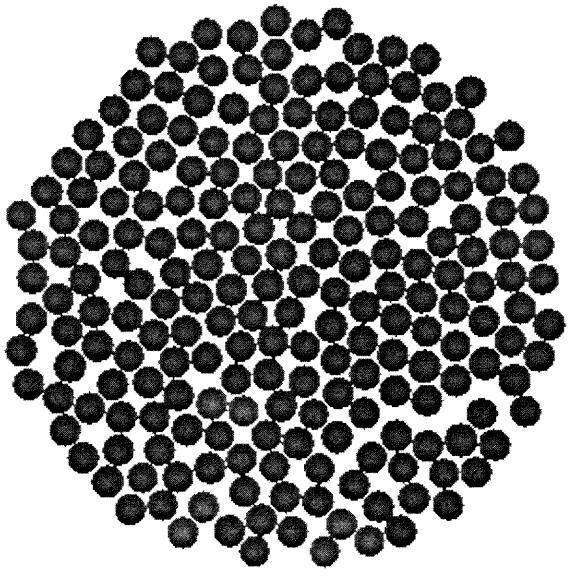

Figure 7.26 Cluster at the end of impact test at v = 0.2 m/s

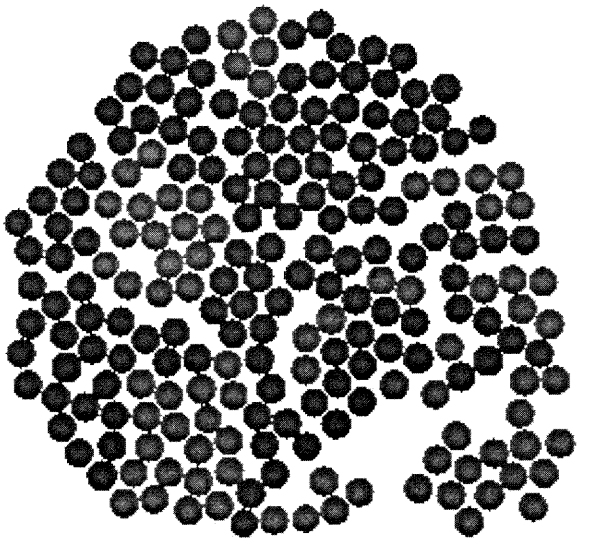

Figure 7.27 Cluster at the end of impact test at v = 0.5 m/s

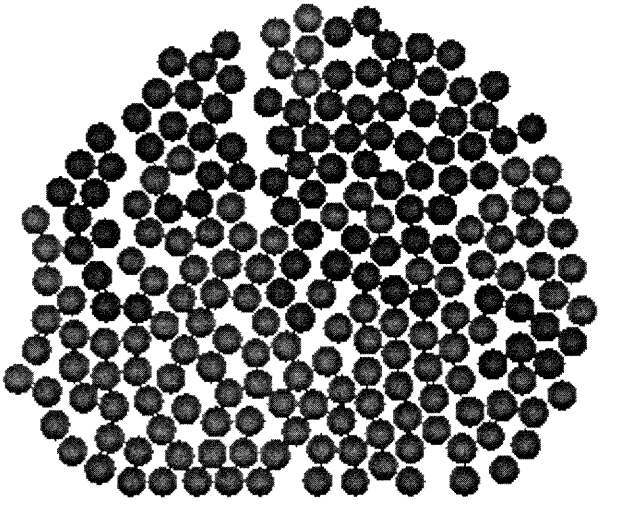

Figure 7.28 Cluster at the end of impact test at v = 1.0 m/s

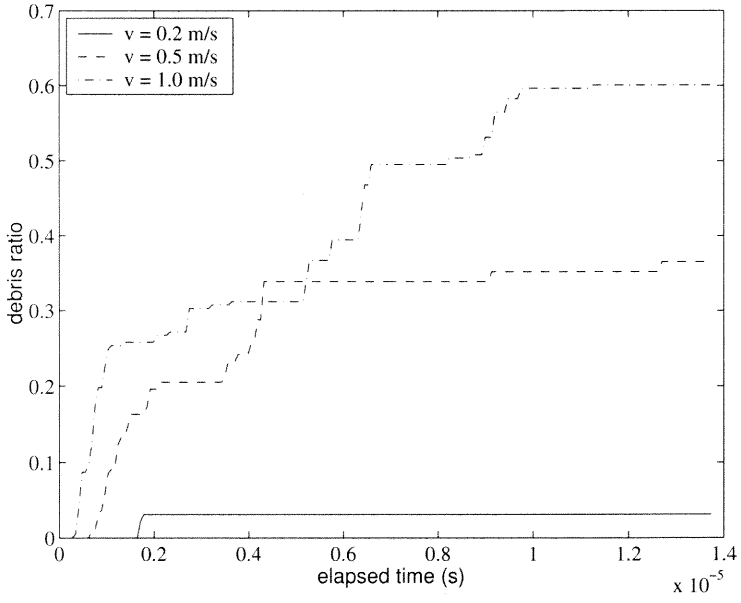

Figure 7.29 Evolution of debris ratio as a function of impact velocity

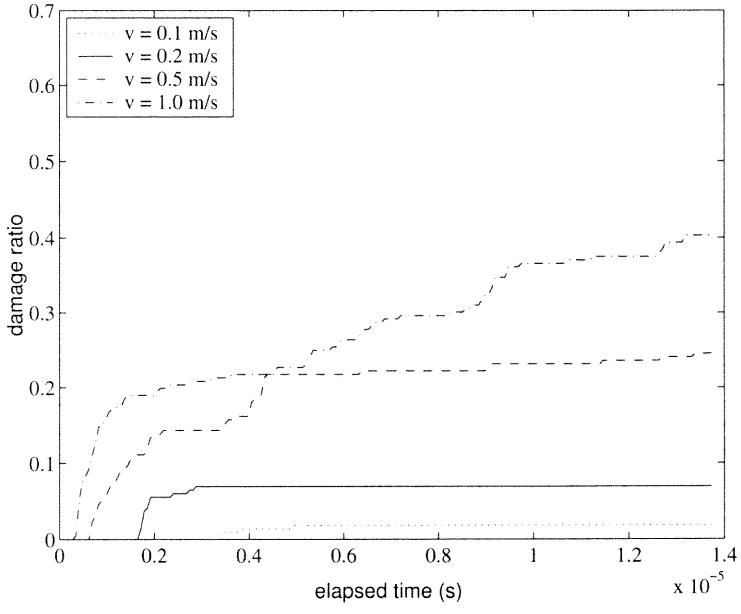

Figure 7.30 Evolution of damage ratio as a function of impact velocity

7.7 Diametrical Compression Test

In the Mechanofusion system, when single agglomerate pass through the inner-piece area, it will fracture under shear and compression interactions in this area. This interaction can be simplified as the degradation of the agglomerate under diametrical compression by two walls. The interaction is illustrated in Fig. 7.31. Here, the agglomerate is compressed by two walls which moving together in y-direction under velocity v. In this study, the bottom wall is a stationary wall and the top wall is a moving wall. The simulation will continue till the strain rate of the system is 10 %.

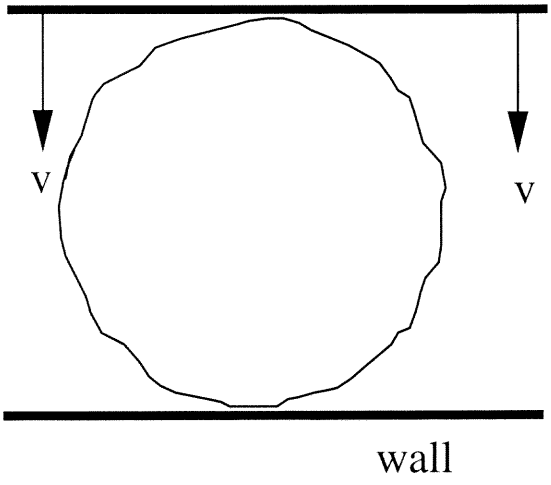

Figure 7.31 Diametrical compression under two walls

The agglomerate was easy to break under this interaction. The larger fractures happened under the lower compression velocity (v = 0.1 m/s). When the compression velocity increased to v = 0.6 m/s, the agglomerate shattered to the wall surface and most debris and fines concentrate inside the impact area. Figure 7.32 $\sim$ Fig. 7.34 is the imagine of cluster at the end of test under velocity v = 0.1, 0.2, 0.6 m/s, respectively, where debris is shown in grey color. Figure 7.35 and Fig. 7.36 are development of debris ratio and damage ratio as a function of compression velocity, respectively. The value of the debris ratio and damage ratio at the end of test increased with the compression velocity. Moreover, the initial growing

rate of debris ratio and damage ratio increased with the velocity. However, as shown in Fig. 7.35 and Fig. 7.36, the increasing rate leveled off during the middle of compression period, which shows the elastic resistance of the agglomerate during the compression. The elastic performance of the agglomerate during the diametrical test is also shown in the Fig. 7.36, when the agglomerate shattered (under v = 0.6 m/s), the maximum damage ratio at the end of test was smaller compared with the values for the binary tests, which is also reported in the research work by Ciomocos [107].

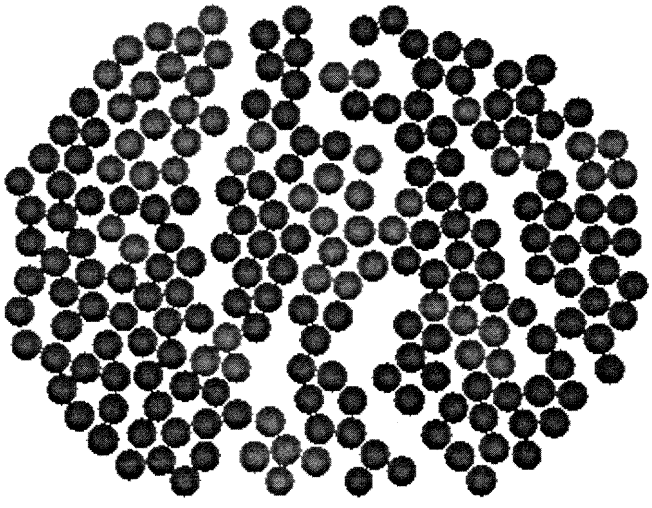

Figure 7.32 Cluster at the end of compression test at v = 0.1 m/s

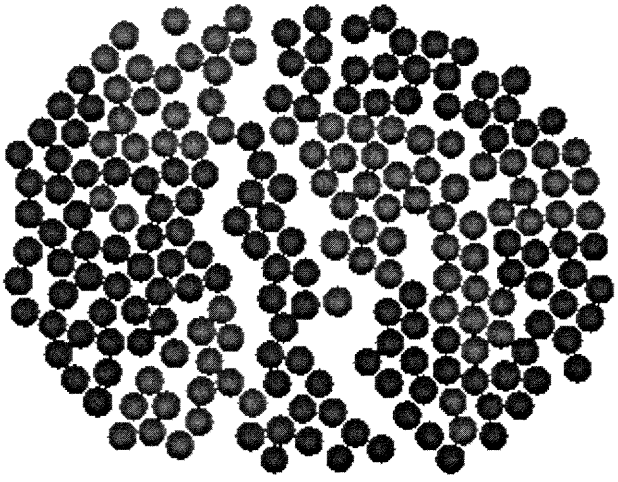

Figure 7.33 Cluster at the end of compression test at v = 0.2 m/s

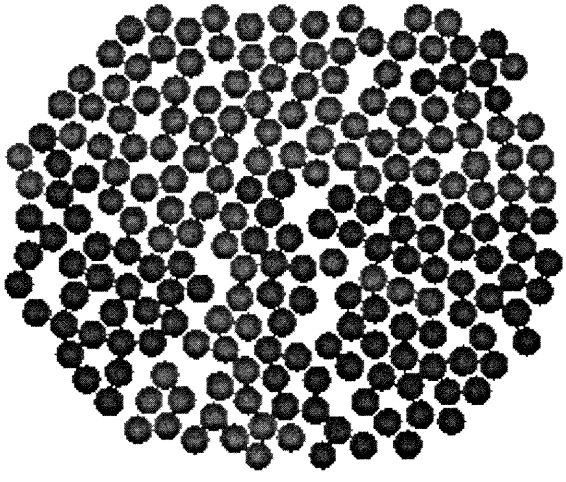

Figure 7.34 Cluster at the end of compression test at v = 0.6 m/s

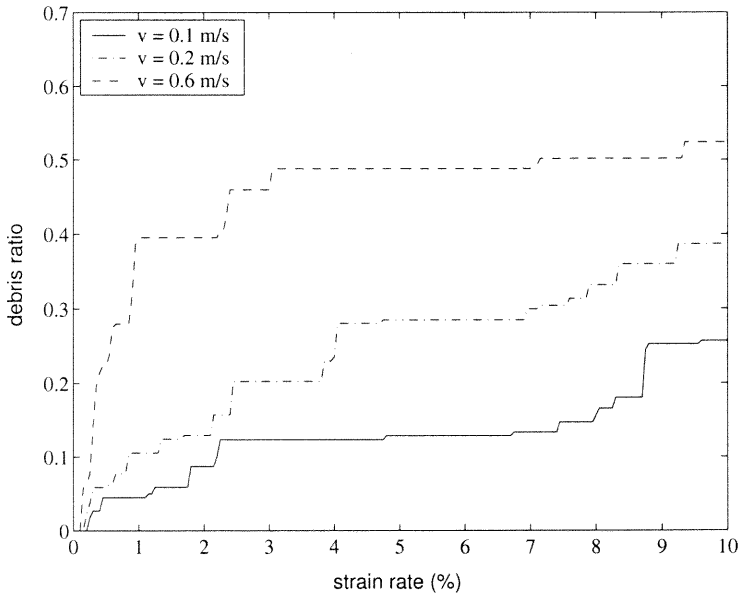

Figure 7.35 Evolution of debris ratio as a function of compression velocity

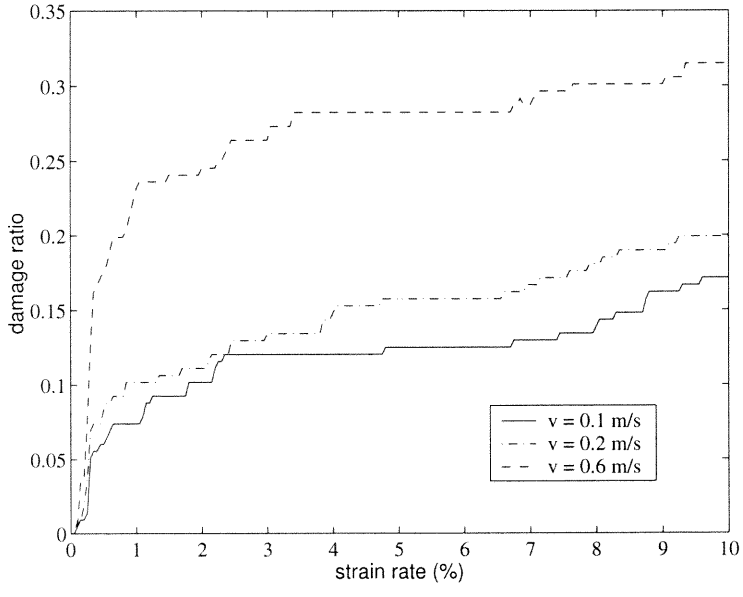

Figure 7.36 Evolution of damage ratio as a function of compression velocity

7.8 Conclusion

Before dry particle coating process, guest agglomerates are degraded into small fragments during interactions with each other, host particles as well as equipment boundary. The fracture/fragmentation of single agglomerate under normal interactions with a host particle and system walls is examined in detail in the chapter. Although the test is limited in the normal interactions, it can represent the general interactions inside the system. The study shows that the single agglomerate may fracture or even shatter during normal impact with the host particle or the walls.

Based on the results from the system simulation, the impact test is performed under various velocities. Generally, higher impact velocities lead to higher local damage and debris. Under extreme conditions, the high impact velocity induces shattering of the agglomerate. The fracture pattern of the agglomerate under normal interaction with a wall agrees with the reported work in three-dimensional simulation [108] [109]. Increasing surface energy has the inverse function. Contact bonds inside the agglomerate becomes stronger with larger surface energy. During a normal impact with a host particle, under the same impact condition (i.e., impact velocity), an agglomerate with the stronger contact bonds had around 10 % less debris ratio and damage ratio after the impact than the agglomerate with smaller surface energy.

CHAPTER 8

CONCLUSIONS

Dry particle coating is a new and promising technique. The dissertation work is very helpful for the in-depth understanding of Mechanofusion system in the application of dry particle coating. The numerical study is performed on two scales: system scale and micro scale. The system scale simulation uncovers the dynamics of the system which is driving-force for dry particle coating, while the micro scale simulation examines the fracture of guest agglomerates prior to dry coating. DEM technique is successfully applied in both simulations.

The system-scale simulation is based on a mono-dispersed system. In numerical model, an existing, widely used, non-adhesion contact model (Walton-Braun) has been employed for two-dimensional discrete element simulation studies. Visualization of the particulate patterns inside the system and the diagnostic analysis derived from the numerical simulations uncover the dynamics of the system. The numerical simulation are proved to be capable of capturing the features of particle behavior in the system. The calculation result of forces on the inner piece is qualitively comparable with that of experiment result. Simulations are performed to obtain some useful quantities such as impact forces on the particles due to interactions with other particles and vessel parts, and collision frequencies. The results show that a particle may experience larger force inside the inner piece area and the scraper area, and the particle has highest interaction frequency inside the inner piece area. Coating level of a simplified coating system is estimated by impact theory based on particle-particle interactions. Results show that coating level is correlated to hardness of host particle and size of guest particle, which agree with experimental observation. Coating time which is the minimum time needed to cover the whole coating surface is acquired by the system simulation. Examination of key parameters on coating

effect illustrates that increasing rotational speed of chamber yields even coating with less coating time, meanwhile, decreasing gap size may cause longer coating time.

Numerical results for a simulated system are correlated to a real system on the basis of kinetic theory since particle flow inside the system could be simplified as a collisional flow. Kinetic theory is applied to the dimensional analysis of the system. An equation of average forces acting on particles inside system is established to evaluate the performance of the real system based on the simulated system. Similarity results based on kinetic theory modeling and verified by simulations show that Inter-particle (host-host) forces vary linearly with the rotation speed, force exerted on the particles within the inner-piece zone is inversely proportional to the gap-size, and force on the inner-piece varies linearly with the square of the rotation speed, which is in agreement with reported experimental data. Moreover, kinetic modeling agrees with numerical simulations on that two geometry similar systems may create resembling coating outcome under same operation conditions.

The fracture/fragmentation of an agglomerate under normal interactions with host particle and system walls is examined in detail by the micro-scale simulation. The numerical study is implemented in two-dimensional mode, which includes auto-adhesive interactions between particles. The micro-scale simulation takes use of some information from the system-scale simulation. The study shows that single agglomerate may fracture or even shatter during normal interactions with host particles and system equipment. The fracture pattern of the agglomerate is in agreement with reported work done by three-dimensional simulation. Generally, higher impact velocity leads to higher local damage and debris. Under extreme conditions, the high impact velocity induces shattering of the agglomerate. The increased surface energy has the opposite function. The agglomerate becomes much stronger with larger surface energy. After the same impact velocity, the agglomerate with higher surface energy had less debris ratio and damage ratio.

It is said "The more we discover, the more we realize how much more still remains to be discovered". The dissertation studies the mechanism of Mechanofusion device for dry particle coating process by DEM technique. Results show that numerical simulation can capture the dynamics of the system and estimate the resulted coating outcome as well as examine the fragmentation of single agglomerate prior to dry particle process. It is known that dry particle coating process is a time continuous procedure. More understanding of the interactions of guest particles with host particles and distribution of the guest particles on surface of the host particles with time is required, which could lead to a better view of the process. Besides, an obvious extension to the research reported in the dissertation is to carry out three-dimensional simulations.

APPENDIX A

DIAGNOSTIC QUANTITIES FOR A THREE-DIMENSIONAL SYSTEM

The performance of a three-dimensional system is examined to compare the dynamics of the system with the corresponding two-dimensional system. The simulation is carried out on a small cylindrical cell, height 1.6 mm (equal to four particles size) and diameter 25 mm (same dimension for two-dimensional studies). During the simulation, the system is assumed to have periodic boundaries in z-direction and solid boundary along the cylindrical surface. The periodic boundaries allow particles to leave and re-enter the ends of cylinder with the same velocity at its image. The operation parameters is list in Table 4.1, except that load of the system is 6000 particles to keep the system have the same solid ratio as that of the two-dimensional system. The simulation time is 1 second.

Figure A.1, Fig. A.3 and Fig. A.5 show distribution of rotational kinetic energy, deviatoric kinetic energy and pressure inside the chamber for the system, respectively, and Fig. A.2, Fig. A.4, and Fig. A.6 illustrate the comparison of diagnostic quantities within the chamber with the corresponding two-dimensional system. Each point in Fig. A.2, Fig. A.4, and Fig. A.6 represents an average value for the system during a long period (here it is equal to 0.2 second). The distribution patterns of diagnostic quantities for the three-dimensional system are in agreement with that for the two-dimensional system (Fig. 4.8, Fig 4.10 and Fig. 4.12). However, there is some difference in average values within two systems (as shown in Fig. A.2, Fig. A.4, and Fig. A.6). Comparatively, it is not significant, which means two systems have the similar dynamics.

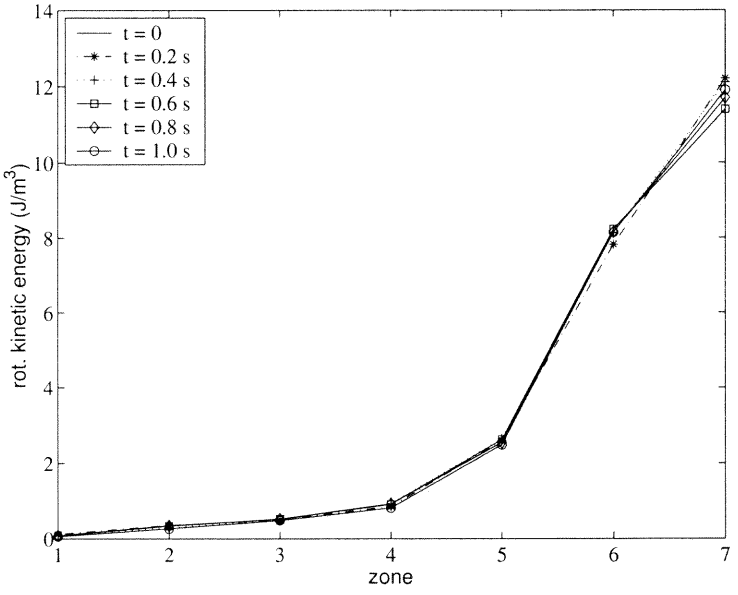

Figure A.1 Rotational kinetic energy distribution inside the chamber for the three-dimensional system

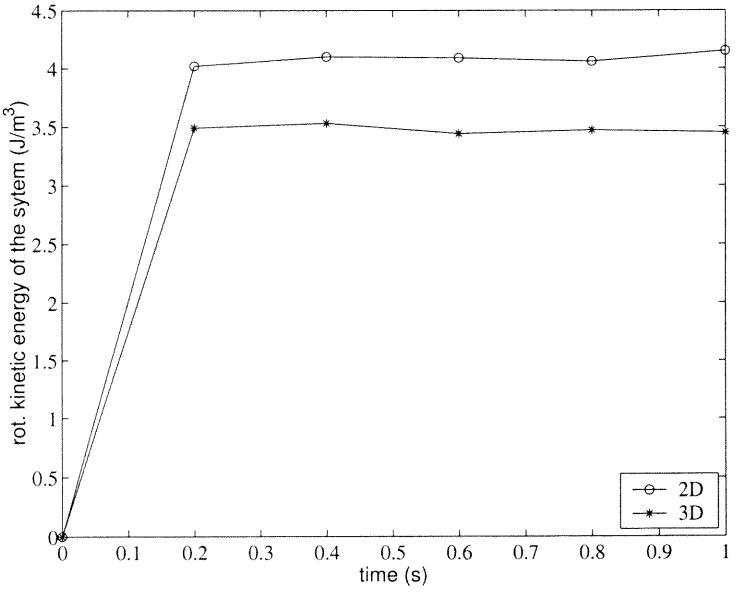

Figure A.2 Comparison of average rotational kinetic energy within the chamber for two systems

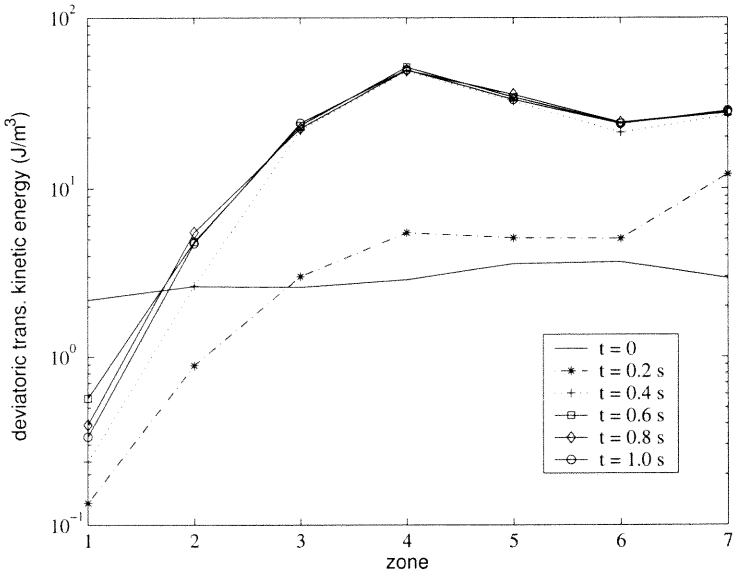

Figure A.3 Deviatoric kinetic energy distribution inside the chamber for the three-dimensional system

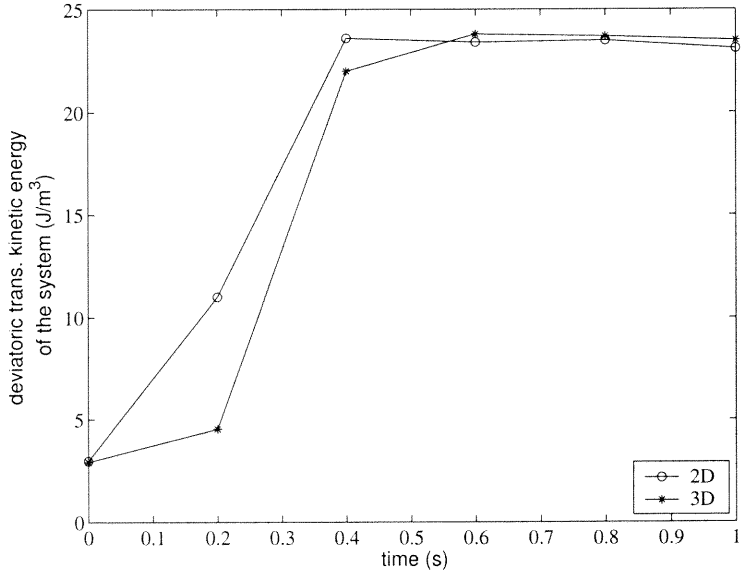

Figure A.4 Comparison of average deviatoric kinetic energy within the chamber for two systems

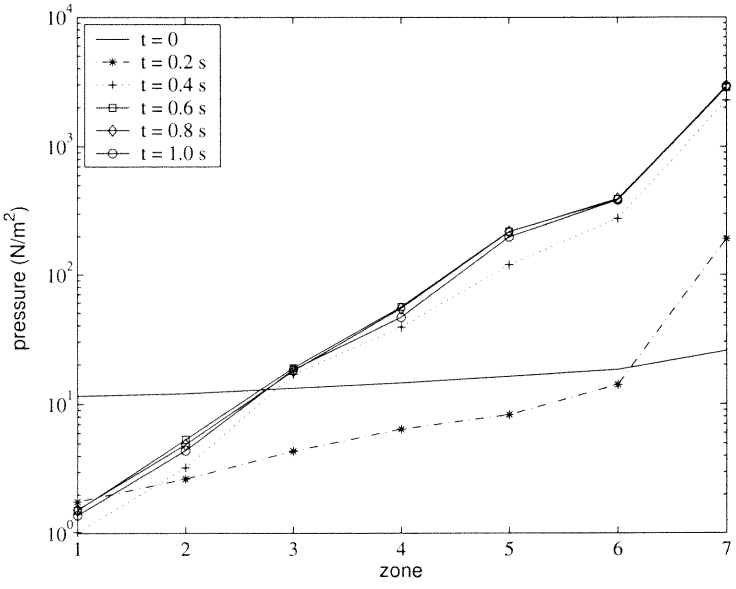

Figure A.5 Pressure distribution inside the chamber for the three-dimensional system

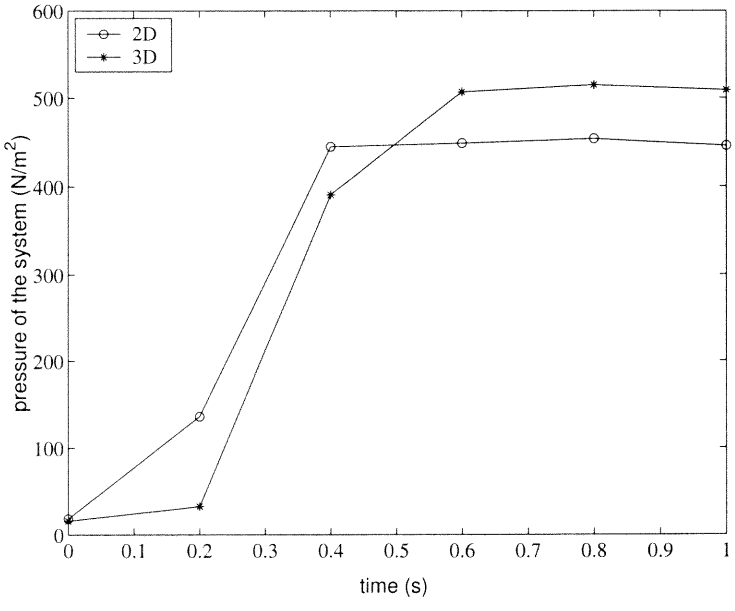

Figure A.6 Comparison of average pressure within the chamber for two systems

APPENDIX B

DEFORMATION CALCULATION

The calculation of deformation of guest particle to host surface resulted from host-host interaction is described in detail here. For PMMA particles, the limiting elastic velocity, φ, given by [110]

$$\varphi = \left(\frac{2\pi}{3K}\right)^2 \left(\frac{2}{5\rho}\right)^{1/2} Y^{5/2} \tag{B.1}$$

is as small as 0.0081 m/s. It can be assumed that interactions inside the system are beyond elastic yield limit, where Hertz equations may not be applied.

The impact calculation is therefore implemented by Rogers and Reed impact model [76], which describes the adhesion of a particle to a surface following an elastic-plastic impact. The model is based upon consideration of the energy balance during the interaction of two bodies. It is readily extended to the case of impact between two spherical bodies. Assume two spheres approaching each other at velocity v, the maximum contact area radius a_m can be calculated by equation:

$$a_m = \left(\frac{2Q_{pe}}{\pi Y R}\right)^{1/2} \left(\frac{3K}{2\pi Y}\right) \tag{B.2}$$

where Y is the yield stress of the impacting particle and

$$K = \frac{4}{3\pi(k_1 + k_2)} \tag{B.3}$$

with $k_i = (1 - \nu_i^2)/\pi E_i$ and ν_i and E_i are Poisson's ratio and Young's modulus for particles, and i is the index for particles ($i = 1, 2$), and for same materials, $K = \frac{2}{3}\frac{E}{1-\nu^2}$. R is the radius of contact system, which is calculated by equation:

$$R = \frac{r_1 r_2}{r_1 + r_2}$$

where r_1, r_2 is the radius of the contact particle 1, 2, respectively. For the particles with same size, $R = r/2$; m is particle mass, and $m = \frac{4}{3}\pi r^3 \rho$, and ρ is particle density.

The energy stored as elastic deformations in the area of plastic deformation during impact, Q_{pe}, can be calculated by equation:

$$Q_{pe} = \left(\frac{15m\varphi^2}{8}\right)^{1/2} \left(\frac{(2mv^2 - \frac{1}{8}m\varphi^2)^{1/2} - (\frac{15}{8}m\varphi^2)^{1/2}}{2}\right) \tag{B.4}$$

where φ is the limiting elastic velocity.

The total force, P, can be approximately calculated by

$$P = \pi a_m^2 Y \tag{B.5}$$

Assuming guest particles evenly dispersed on the host surface, therefore, the force on singlet guest particle due to host-host interaction can be obtained from:

$$F = \frac{P}{n_g \pi a_m^2} \tag{B.6}$$

where n_g is number of guest particles per m^2 on host surface, and $n_g = \frac{1}{\pi r^2}\rho$, ρ is packing ratio and approximately equal to 0.79 under density packing condition. The resultant contact area radius of this host-guest system can be calculated by Hertizian model equation:

$$a_h = (R'F/K')^{1/3} \tag{B.7}$$

where R' is the radius for host-guest contact system, and K' is the elastic constants of the contact system and can be calculated by Eq. B.3 based on material of contacting spheres. Considering adhesion effect arose from surface energy of a guest particle with that of the host particle, the new contact area can be deduced by JKR model equation as:

$$a_j = \left[\frac{R'}{K'}\left\{F + 3\gamma\pi R' + \left[6\gamma\pi R'F + (3\gamma\pi R')^2\right]^{\frac{1}{2}}\right\}\right]^{1/3} \tag{B.8}$$

where γ is surface energy between two elastic bodies, and can be estimated by equation [76]:

$$\gamma = 2\sqrt{\varpi_{d1}\varpi_{d2}} + 2\sqrt{\varpi_{p1}\varpi_{p2}} \tag{B.9}$$

where ϖ_d, ϖ_p refer to dispersive surface energy and polar surface energy respectively.

Then, the corresponding central displacement of a guest particle on a host surface can be calculated by:

$$\delta_j = \frac{a_j^2}{R'} - \left(\frac{8\pi\gamma a_j}{3K'}\right)^{1/2} \tag{B.10}$$

REFERENCES

1. Y. Fukumori, Y. Yamaoka and H. Khikawa, "Coating of pharmaceutical powders by fluidized bed process. IV.," *Chemical & pharmaceutical bulletin*, **36**, 12, pp. 4927-4941, 1988.

2. N. Liberto, "Powder coating equipment part 1: application," *Metal Finishing*, **88**, 8, pp. 23-49, 1990.

3. W. J. Lackey, "Liquid fluidized bed coating process," *Carbon*, **34**, 10, pp. 1299-1315, 1996.

4. J. Visser, "An invited review: Van der Waals and other cohesive forces affecting powder fluidization," *Powder Tech.*, **58**, pp. 1-10, 1989.

5. H. Kage, K. Nishihara, H. Ishimatsu, H. Ogura and Y. Matsuno, "Effect of drying on powder coating efficiency and agglomeration in vibro-fluidized bed," *Dry Tech.*, **19**, 2, pp. 359-374, 2001.

6. H. Kage, M. Dohzaki and Y. Matsuno, "Powder coating efficiency of small particles and their agglomeration in circulating fluidized bed," *The Kerean J. of the Mical-Engineering*, **16**, 5, pp. 630-643, 1999.

7. K. Sudsakom and R. Turton, "Nonuniformity of particle coating on a size distribution of particles in a fluidized bed coater," *Powder Tech.*, **110**, pp. 37-51, 2000.

8. M. Naito, M. Yoshikawa, T. Tanaka and H. Kondo, "Analysis of the powder composite process by a mechanical method," *J. Soc. Powder Technol.*, Japan, **29**, pp. 434-441, 1992.

9. H. Honda, M. Kimura, F. Honda, T. Matsuno and M. Koishi, "Preparation of monolayer particle coated powder by the dry impact blending process utilizing mechanochemical treatment," *Colloids and Surfaces A: Physicochemical and Engineering Aspects*, **82**, pp. 117-128, 1994.

10. H. Honda, M. Kimura, T. Matsuno and M. Koishi, "Preparation of composite and encapsulated powder particles by dry impact blending," *CHIMICA OGGI - June*, pp. 21-26, 1991.

11. T. Yokoyama and K. Urayama, "The Angmill Mechanofusion System and its Applications," *KONA*, **5**, pp. 59-68, 1987.

12. H. Honda, K. Ono, etc., "The effect of powder properties on the dry impact blending preparation method," *Journal of the Society of Power Technology*, Japan, **24** (9), pp. 593, 1987.

13. R. K. Singh, A. Ata, and J. Fitz-Gerald, etc, "Dry coating method using magnetically assisted impaction in a randomly turbulent fluidized bed," *KONA*, **15**, pp. 121-130, 1997.

14. Y. Fukumori, H. Ichikawa and M. Ueda, "Preparation of controlled release microcapsules by a high-speed elliptical-rotor type powder mixer," *Proc. World Congress on Particle Technology 3*, Brighton, UK, pp. 1217, 1998.

15. K. Tanno, "Current status of the Mechanofusion process for producing composite particles," *KONA*, **8**, pp. 74-82, 1990.

16. H. Herman, J. Chen, C. Huang, and R. Cohen, "Mechanofused powders for thermal spray," *J. of thermal Spray Technology*, **1**(2), pp. 129-135, 1992.

17. H. Kaga, Y. Taya, I. Shimono and H. Katayama, "Preparation of Al_2O_3/Cu composite particles by vacuum Mechanfusion process," *Process. J. Soc. Powder-Powder Metall.*, Japan, **39**, pp. 546-553, 1992.

18. K. Tanno, T. Onagi and M. Naito, "Preparation of stainless stell/zirconia composite particles with a multi-phase coating layer," *Advanced Powder Technol.*, **5**, 4, pp. 393-405, 1994.

19. J. Chen and H. Herman, "A preliminary model For Mechanofusion powder processing," *KONA*, **15**, pp. 113-120, 1997.

20. M. Alonso, M. Satoh and K. Miyanami, "Kinetics of fines transfer among carriers in powder coating," *Powder Technology*, **59**, pp. 217-224, 1989.

21. M. Alonso, M. Satoh and K. Miyanami, "The effect of random positioning on the packing of particles adhering to the surface of a central particle," *Powder Technology*, **62**, pp. 35-40, 1990.

22. P. Bannister and N. Harnby, "A colorimetric technique for assessing the mixture quality of fine particle mixtures," *Powder Technology*, **36**, pp. 275-279, 1983.

23. P. K. Haff, "Grain flow as a fluid mechanical phenomena," *J. Fluid Mech.*, **134**, pp. 401-430, 1983.

24. P. K. Haff, "A physical picture of kinetic granular fluids," *J. Rheol.*, **30**, pp. 931-948, 1986.

25. K. Hui and P. K. Haff, "Kinetic grain flow in a vertical channel," *Int. J. Multiphase Flow*, **12**, pp. 289-298, 1986.

26. P. C. Johnson and R. Jackson, "Frictional-collisional constitutive relations for granular materials, with application to plane shearing," *J. Fluid Mech.*, **176**, pp. 67-93, 1987.

27. P. C. Johnson, P. Nott and R. Jackson, "Frictional-collisional constitutive equations of motion for particulate flows and their application to chutes," *J. Fluid Mech.*, **210**, pp. 501-535, 1990.

28. K. Hui, P. K. Haff, J. E. Ungar and R. Jackson, "Boundary conditions for high-shear grain flows," *J. Fluid Mech.*, **145**, pp. 223-233, 1984.

29. P. A. Cundall, "Ball - a program to model granular media using the distinct element method," *Technical Note*, Advanced Technology Group, Dames and Moore, London, 1978.

30. P. A. Cundall and O. D. L. Strack, "A Discrete Numerical Model for Granular Assemblies," *Geotechnique*, **29**, pp. 47-65, 1979.

31. P. A. Cundall and O. D. L. Strack, "The Distinct Element Method as a Tool for Research in Granular Media," Part II, Dept. Civ. Min. Engrg. Univ. Minnesota, 1979.

32. P. A. Cundall and O. D. L. Strack, "Modelling of Microscopic Mechanisms in Granular Material," *Mechanics of Granular Materials: New Models and Constitutive Relations*, J. T. Jenkins and M. Satake ed., Elsevier Science Publisher, Amsterdam, 1983.

33. R. Smith, K. Beardmore and A. Gras-Mati, "Molecular dynamics simulation of particle-surface interactions," *Vacuum*, **46**, 8-10, pp. 1195-1199, 1995.

34. D. J. Quesnel, D. S. Rimai and L. P. Demejo, "Molecular dynamic modeling of interfacial energy," *J. Adhesion Sci. Technol.*, **9**, 8, pp. 1015-1030, 1995.

35. C.-C. Chen, D. Y. Paithankar, J. Talbot and R. P. Andres, "Molecular dynamic simulation of gold cluster collisions," *Atoms, Molecules and Cluster*, Spring-Verlag, pp. 165-167, 1993.

36. J. Lian and S. Shima, "Powder assembly simulation by particle dynamics method," *International J. Numerical Methods in Engineering*, **37**, pp. 763-775, 1994.

37. M. P. Allen and D. J. Tildesley, *Computer Simulation of Liquids*, Clarendon Press, Oxford, 1987.

38. D. S. Cahn and D. W. Fuerstenau, "Simulation of diffusional mixing of particulate solids by Monte Carlo techniques," *Powder Tech.*, **1**, pp. 174-182, 1967.

39. M. A. Hopkins and M. Y. Louge, "Inelastic microstructure in rapid granular flows of smooth disks," *Phys. Fluids A*, **3**, pp. 47-57, 1991.

40. M. A. Hopkins and H. Shen, "A Monte Carlo solution for rapidly shearing granular flows based on the kinetic theory of dense gases," *J. Fluid Mech.*, **244**, pp. 477-491, 1992.

41. P. A. Cundall, "A computer model for simulating progressive, large scale movements in blocky rock system," *Proceedings of the Symposium of International Society of Rock Mechanics*, Nancy, Article 8, 1971.

42. P. K. Haff, "Discrete Mechanics," Granular Matter - An Interdisciplinary Approach, Springer - Verlag, pp. 141-160, 1993.

43. C. S. Campbell, "Computer simulation of Powder Flows," K. Gotoh, et. al ed., Marcel Dekker, Inc., New York · Basel · Hong Kong, 1997.

44. C. S. Campbell and A. Gong, "The stress-tensor in a two-dimensional granular flow," *J. Fluid Mech.*, **164**, pp. 107-125, 1986.

45. C. S. Campbell, "Rapid granular flows," *Annu. Rev. Fluid Mech.*, **22**, pp. 57-92, 1990.

46. O. R. Walton, "Numerical Simulation of Inelastic, Frictional Particle-Particle Interactions," in *Particle Two-Phase Flow*, M. C. Roco, ed., Butterworth - Heinemann, Boston, 1993.

47. C. S. Campbell and C. E. Brennen, "Computer Simulation of Granular Shear Flows," *J. Fluid Mech.*, **151**, pp. 167-188, 1985.

48. D. M. Hanes and D. L. Inman, "Observations of rapidly flowing granular-fluid materials," *J. Fluid Mech.*, **150**, pp. 357-380, 1985.

49. K. K. Yin, "Numerical modelling of agglomerate degradation," *PhD Thesis*, Aston University, 1992.

50. G. Lian, C. Thornton and M. J. Adams, "Discrete Particle Simulation of Agglomerate Impact Coalescence," *Chemical Eng. Sci.*, **53**, No. 19, pp. 3381-3391, 1998.

51. O. R. Walton, "Numerical simulation of inclined chute flows of monodisperse, inelastic, frictional spheres," *Advances in Micromechanics of Granular Materials*, H. H. Shen et al. (eds.), Elsevier Science Publishers B. V., pp. 453-460, 1992.

52. R. Mei, H. Shang, O. R. Walton and J. F. Klausner, "Concentration non-uniformity in simple shear flow of cohesive powders," *Powder Tech.*, **112**, pp. 102-110, 2000.

53. Y. Tsuji, "Activities in discrete particle simulation in Japan," *Powder Tech.*, **113**, pp. 278-286, 2000.

54. Y. Tsuji, T. Tanaka and T. Ishida, "Lagrangian numerical simulation of plug flow of cohesionless particles in a horizontal pipe," *Powder Tech.*, **71**, pp. 239-250, 1992.

55. Y. Tsuji, T. Kawaguichi and T. Tanaka, "Discrete particle simulation of two-dimensional fluidized bed," *Powder Tech.*, **77**, pp. 79-87, 1993.

56. O. R. Walton, *Energy and Technologh Review*, Lawrence Livermore Lab., pp. 24, 1984.

57. M. A. Hopkins and H. Shen, "Constitutive relations for a planar, simple shear flow of rough disks," *Int. J. Eng. Sci.*, **24**, pp. 1717-1730, 1986.

58. J. Ghaboussi and R. Barbosa, *Int. J. Num. Anal. Meth. Geomech.*, **14**, pp. 451, 1990.

59. Y. Lan and A. D. Rosato, "Macroscopic behavior of vibrating beds of smooth inelastic spheres," *Phys. Fluids*, **7**(8), pp. 1818-1831, 1995.

60. Y. Muguruma, T. Tanaka, S. kawatake, Y. Tsuji, "Discrete Particle Simulation of a Rotary Vessel Mixer with Baffles," *Powder Tech.*, **93**, pp. 261-266, 1997.

61. J. Szepvolgyi Jr., S. Endoh, J. Gyenis and G. I. Tardos, "Dynamic simulation of particle motion in a high shear mixer," *AIChE Annual Meeting: Numerical Methods in Powder Technology*, Dallas, TX, Oct. 31-Nov. 5, 1999.

62. J. J. McCarthy and J. M. Ottino, "Particle Dynamics Simulation: A Hybrid Technique Applied to Granular Mixing," *Powder Tech.*, **97**, pp. 91-99, 1998.

63. Y. F. Cheng, S. J. Guo and H. Y. Lai, "Dynamic simulation of random packing of spherical particles," *Powder Tech.*, **107**, pp. 123-130, 2000.

64. K. Iwashita and M. Oda, "Micro-deformation mechanism of shear banding process based on modified distinct element mechod," *Powder Tech.*, **109**, pp. 192-205, 2000.

65. K.L. Johnson, "One hundred years of Hertz contact," *Proceeding of Insitute of Mechanical Engineers*, **196**, pp. 363-377, 1982.

66. R. D. Mindlin and H. Deresiewicz, "Elastic spheres in contact under varying oblique forces," *J. Appl. Mech. Trans. ASME*, **20**, pp. 327-344, 1953.

67. O. R. Walton and R. L. Braun, "Viscosity and Temperature Calculations for Assemblies of Inelastic Frictional Disks," *J. Rheology*, **30**(5), pp. 949-980, 1986.

68. O. R. Walton, H. Kim, and A. D. Rosato, "Microstructure and Stress Differences in Shearing Flows," *Mechanics Computing in 1990's and Beyond*, H. Adeli and R. L.Sierakowski, eds., ASCE, NY, **2**, pp. 1249-1253, 1991.

69. O. R. Walton and R. L. Braun, "Stress Calculations for Assemblies of Inelastic Spheres in Uniform Shear," *Acta Mechanica*, **63**, pp. 73-86, 1986.

70. O. R. Walton, "Numerical Simulation of Inclined Chute Flows of Monodisperse, Inelastic, Frictional Spheres," *Mech. of Materials*, **16**, pp. 239-246, 1993.

71. W. Chen, R. N. Dave and R. Pfeffer, "Numerical simulation of Mechanofusion system for dry particle coating," *AIChE Annual Meething*: Particle Technology Forum, Reno Hilton, Reno, NV, November 2001.

72. W. Chen, R. N. Dave and R. Pfeffer, "Computer simulation and modeling of Mechanofusion system for dry particle coating," *IFPRI Annual Meeting*, Gainesville, Florida, June 2001.

73. W. Chen, R. N. Dave and R. Pfeffer, "Computer simulation of Mechanofusion process for dry particle coating," *AIChE Annual Meething*: Fourth International Particle Technology Forum, Los Angeles, CA, November 2000.

74. A. J. Matchett, T. Yanagida and S. Kobayashi, "Vibrating powder beds: a comparison of experimental and Distinct Element Method simulated data," *Powder Tech.*, **107**, n1/2, 13, 2000.

75. A. Ladd, "Molecular Dynamics," *Lectures to be given at the Nato Advanced Summer Institute in Bath*, England, pp. 4-17, September 1988.

76. L. N. Rogers and J. Reed, "The adhesion of particles undergoing an elastic-plastic impact with a surface," *J. Phys. D: Appl. Phys.*, **17**, pp. 677-689, 1984.

77. S. B. Savage and D. J. Jeffrey, "The stress tensor in a granular flow," *J. Fluid Mech.*, **110**, pp. 255-272, 1981.

78. S. B. Savage, "The mechanics of rapid granular flows," *Adv. Appl. Mech.*, **24**, pp. 289-366, 1984.

79. M. W. Richman and C. S. Chou, "Boundary effects on granular shear flows of smooth disks," *J. Appl. Phys. Math.*, **39**, pp. 885-901, 1988.

80. C. K. K. Lun, S. B. Savage, D. J. Jeffrey and N. Chepurniy, "Kinetic theories for granular flow: inelastic particles in Couette flow and slightly inelastic particles in a general flow field," *J. Fluid Mech.*, **140**, pp. 223-256, 1984.

81. J. T. Jenkins and S. B. Savage, "A theory for the rapid flow of identical, smooth, nearly elastic, spherical particles," *J. Fluid Mech.*, **130**, pp. 187-202, 1983.

82. S. Chapman and T. G. Cowling, *The Mathematical Theory of Nonuniform Gases*, Cambridge University Press: Cambridge, 1970.

83. R. A. Bagnold, "Experiments on a gravity-free dispersion of large solid sphere in a Newtonian fluid under shear," *Proc. R. Soc. Lond.*, **A 225**, pp. 49-63, 1954.

84. S. B. Savage and M. Sayed, "Experiments on dry cohesionless materials in an annular shear cell at high strain rates," *Proc. EUROMECH 133, Statics and Dynamics and Granular Materials*, Oxford University Press, 1980.

85. J. T. Jenkins and M. W. Richman, "Grad's 13-Moment System for a Dense Gas of Inelastic Spheres," *Arch. Rat. Mech. Anal.*, **87**, pp. 355-377, 1984.

86. B. Dahneke, "The influence of flattening on the adhesion of particles," *J. Colloid and Interface Sci.*, **40**, 1, pp. 1-13, 1972.

87. C-J. Tsai, D. Y. H. Pui and B. Y. H. Liu, "Elastic flattening and particle adhesion," *Aerosol Science and Technology*, **15**, pp. 239-255, 1991.

88. K. L. Johnson, K. Kendall and A. D. Roberts, "Surface energy and contact of elastic solids," *Proc. Roy. Soc. Lond. A.*, **324**, pp. 301-313, 1971.

89. B. V. Deryaguin, V. M. Muller and Y. P. Toporov, "Effect of contact deformations on the adhesion of particles," *J. Colloid and Interface Sci.*, **53**, pp. 314-379, 1975.

90. R. G. Horn, J. N. Israelachvili and F. Pribac, "Measurement of the deformation and adhesion of solids in contact," *J. Colloid and Interface Sci.*, **115**, 2, pp. 481-491, 1987.

91. V. M. Muller, V. S. Yushenko and B. V. Derjaguin, "On the influence of molecular forces on the deformation of an elastic sphere and its sticking to a rigid plane," *J. Colloid and Interface Sci.*, **77**, pp. 91-101, 1980.

92. D. Maugis, "Extension of the Johnson-Kendall-Roberts theory of the elastic contact of spheres to large contact radii," *Langmuir*, **11**, pp. 679-682, 1995.

93. S. Wall, W. John and H.-C. Wang, "Measurements of kinetic energy loss for particles impacting surface," *Aerosal Science and Technology*, **12**, pp. 926-946, 1990.

94. R. P. Andres, "Inelastic energy transfer in particle/surface collisions," *Aerosal Science and Technology*, **23**, pp. 40-50, 1995.

95. S. S. Brenner, H. A. Wreidt and R. I. Oriani, *Wear*, **68**, pp. 169-190, 1981.

96. P. Attard and J. L. Parker, "Deformation and adhesion of elastic bodies in contact," *Physical Review A*, **46**, 12, pp. 7959-7971, 1992.

97. R. M. Brach and P. F. Dunn, "A machematical model of the impact and adhesion of microspheres," *Aerosol Science and Technology*, **16**, pp. 51-64, 1992.

98. R. M. Brach and P. F. Dunn, "Macrodynamics of microparticles," *Aerosol Science and Technology*, **23**, pp. 51-71, 1995.

99. K. Johnson and H. M. Pollock, "The role of adhesion in the impact of elastic spheres," *J. Adhesion Sci. Technol.*, **8**, 11, pp. 1323-1332, 1994.

100. C. Thornton and W. Randall, "Applications of theoretical contact mechanics to solid particle system simulation," in M. Satake and J. T. Jenkins (ed.), *Micromechanics of Granular Materials*, pp. 133-142, 1988.

101. C. Thornton and Z. Ning, "A theoretical model for the stick/bounce behaviour of adhesive, elastic-plastic spheres," *Powder Tech.*, **99**, pp. 155-162, 1998.

102. C. Thornton, "Interparticle sliding in the presence of adhesion," *J. Phy. D: Appl. Phys.*, **24**, pp. 1942-1946, 1991.

103. K. L. Johnson, *Contact Mechanics*, Cambridge University Press, Cambridge, 1985.

104. R. D. Mindlin, "Compliance of elastic bodies in contact," *J. Appl. Mech., Trans. ASME*, **16**, pp. 259-268, 1949.

105. A. R. Savkoor and G. A. D. Briggs, "The effect of tangential force on the contact of elastic solids," *Proc. Roy. Soc. Lond. A.*, **356**, pp. 103-114, 1977.

106. C. Thornton and K. K. Yin, "Impact of Elastic Spheres with and without Adhesion," *Powder Tech.*, **65**, pp. 153-166, 1991.

107. M. T. Ciomocos, "Micromechanics of agglomerate damage processes," *PhD thesis*, Aston University, 1996.

108. K. D. Kafui and C. Thornton, "Computer simulated impact of agglomerates," in *Powder & Grains'93.*, Thornton(ed.), pp. 401-406, Balkema, Rotterdam, 1993.

109. K. D. Kafui and C. Thornton, "Numerical simulation of impact breakage of a spherical crystalline agglomerate," *Powder Tech.*, **109**, Nov. 1-3, pp. 113-132, 2000.

110. S. Timoshenko and J. N. Goodier, *Theory of Elasticity*, McGraw-Hill, New York, 1951.